THE UNIVERSITY OF QUEENSLAND

AUSTRALIA

The Development of Rotating Radiofrequency Techniques for Ultra-High Field Magnetic Resonance Imaging

Mingyan Li

Bachelor of Engineering – Electrical

Master of Engineering – Electrical

A thesis submitted for the degree of Doctor of Philosophy at

The University of Queensland in 2015

School of Information Technology and Electrical Engineering

Abstract

Ultra-high field (≥7 T) magnetic resonance imaging (MRI) offers improved image quality to facilitate clinical diagnosis. However, the wavelength of radiofrequency (RF) electromagnetic (EM) waves becomes a fraction of the size of the human body at ultra-high fields; therefore, constructive and destructive interference of RF magnetic field (B_1 field) forms in the human body, causing bright and dark regions in the output images. These artefacts seriously affect the accuracy and diagnostic value of the images. The RF power deposited in the human body is dramatically increased at ultra-high fields and the resultant overheating could potentially damage tissues. The long scan duration is also an issue which is reported as the most unpleasant factor during an MRI scan at 7 T. It can cause patient discomfort, both psychologically and physically; consequently, inevitable motion of the patient could induce motion artefacts in the images that seriously degrade image quality for clinical use.

In terms of hardware, phased array coils are considered to be the best choice to implement parallel transmission and parallel imaging for solving ultra-high field issues. Parallel transmission and parallel imaging use multiple coils to transmit and receive signals. Theoretically, increasing the number of coils in an array can improve the performance of parallel transmission and parallel imaging. However, this raises RF coil related issues, such as reduced B_1 penetration and increased mutual coupling, which undermine the efficiency of parallel transmission/imaging. Alternatively, a physical rotating RF coil is capable of emulating a large number of coils without these RF coil related issues, so it could be employed as a solution. However, with only one coil element, the rotating RF coil (RRFC) is limited in its ability to reduce the scan duration.

The specific aim of this project is to develop RF techniques that strategically combine the array structure with the rotating concept, to provide better solutions for ultra-high field issues. By introducing the rotation, the coil has the capability of acquiring a large number of transmit/receive sensitivity profiles, and thus fewer coils are needed for parallel transmission and parallel imaging. This offers the opportunity of constructing a coil array with lower coupling and bigger coils that have higher efficiency and B_1 penetration. Compared to a stationary coil array, the rotating array will also introduce an extra degree of freedom in the spatial domain to facilitate B_1 field homogenising (B_1 shimming) and Specific Absorption Rate (SAR) control.

The geometry of a 4-element rotating RF coil array (RRFCA) was optimised to achieve natural decoupling and reasonable B_1 penetration, and then the RRFCA prototype was built for imaging a head-size homogenous phantom at 7 T. In order to achieve an image reconstruction without significant B_1 inhomogeneity, a time interleaved, spatial varying B_1 inhomogeneity mitigation strategy for the RRFAC was developed. A dedicated rotating-SENSE algorithm was also developed to accelerate the image acquisition up to four-fold with an optimal chosen stepping angle of the rotation. The feasibility of using the RRFCA at 7 T is also tested with human subjects. At 7 T, the coil-tissue interaction becomes complex and unpredictable. In order to use the rotating-SENSE for fast imaging, a novel *in vivo* rotation-dependent sensitivity estimation algorithm based on a library and registration techniques was developed and validated with human subjects. With the assistance of this algorithm and the rotating-SENSE algorithm, the RRFCA was proved capable of reconstructing artefact-free images at a high reduction factor of scan time. However, mapping the sensitivity required extra scans that potentially extend the scan time, although the overall time was reduced by using dedicated algorithms. In addition, those methods cannot reconstruct images using built-in algorithms on the host computer of MRI system, which prevent their use for applications that require immediate image outputs. Instead of using Cartesian sampling, the feasibility of using radial trajectory to reconstruct artefact-free images with system built-in algorithm was investigated at 9.4 T. This imaging scheme was found to be more practical and can facilitate the rotating technique for *in vivo* applications.

The results suggested that by introducing rotation and with the assistance of an *in vivo* sensitivity estimation algorithm, a low channel-count, large coil-size rotating array is capable of reconstructing images without significant inhomogeneity within only a quarter of the scan duration. By employing the radial sampling, the imaging scheme was more practical and could benefit those *in vivo* applications that require immediate on-line image reconstruction.

Declaration by author

This thesis is composed of my original work, and contains no material previously published or written by another person except where due reference has been made in the text. I have clearly stated the contribution by others to jointly-authored works that I have included in my thesis.

I have clearly stated the contribution of others to my thesis as a whole, including statistical assistance, survey design, data analysis, significant technical procedures, professional editorial advice, and any other original research work used or reported in my thesis. The content of my thesis is the result of work I have carried out since the commencement of my research higher degree candidature and does not include a substantial part of work that has been submitted to qualify for the award of any other degree or diploma in any university or other tertiary institution. I have clearly stated which parts of my thesis, if any, have been submitted to qualify for another award.

I acknowledge that an electronic copy of my thesis must be lodged with the University Library and, subject to the policy and procedures of The University of Queensland, the thesis be made available for research and study in accordance with the Copyright Act 1968 unless a period of embargo has been approved by the Dean of the Graduate School.

I acknowledge that copyright of all material contained in my thesis resides with the copyright holder(s) of that material. Where appropriate I have obtained copyright permission from the copyright holder to reproduce material in this thesis.

Publications during candidature

Peer-reviewed journal papers

Mingyan Li, Zhentao Zuo, Jin Jin, Rong Xue, Adnan Trakic, Ewald Weber, Feng Liu and Stuart Crozier, Highly Accelerated Acquisition and Homogeneous Image Reconstruction with Rotating RF Coil Array at 7 T — A Phantom Based Study, *Journal of Magnetic Resonance*, vol. 240, pp.102-112, 2014.

Mingyan Li, Jin Jin, Zhentao Zuo, Feng Liu, Adnan Trakic, Ewald Weber; Yan Zhuo, Rong Xue, Stuart Crozier, *In vivo* Sensitivity Estimation and Imaging Acceleration with Rotating RF Coil Arrays at 7 Tesla, *Journal of Magnetic Resonance*, vol. 252, pp. 29-40, 2015

Mingyan Li, Thimo Hugger, Ewald Weber, Jin Jin, Feng Liu, Peter Ullmann, Simon Stark, Yasvir Tesiram, Yang Yang, Sven Junge, and Stuart Crozier, A rapid and practical imaging scheme for a rotating coil using radial trajectory at 9.4 T, *Magnetic Resonance in Medicine*, (under preparation).

Jin. Jin, Feng Liu, Zhentao Zuo, Rong Xue, **Mingyan Li**, Yu Li, Ewald Weber, Stuart Crozier, Inverse field-based approach for simultaneous B1 mapping at high fields - A phantom based study, *Journal of Magnetic Resonance*, vol. 217, pp. 27-35, 2012

Adnan Trakic, Jin Jin, **Mingyan Li**, Darryl McClymont, Ewald Weber, Feng Liu, Stuart Crozier, A comparative numerical study of rotating and stationary RF coils in terms of flip angle and specific absorption rate for 7 Tesla MRI, *Journal of Magnetic Resonance*, vol. 236, pp. 70-82, 2013

Peer-reviewed conference proceedings

Mingyan Li, Jin Jin, Adnan Trakic, Feng Liu, Ewald Weber, Yu Li, High Acceleration with Rotating Radiofrequency Coil Array (RRFCA) in Parallel Magnetic Resonance Imaging (MRI), *34th Annual International Conference of the IEEE Engineering in Medicine and Biology Society (EMBC'12)*, San Diego, USA, 2012, *oral presentation*.

Mingyan Li, Jin Jin, Feng Liu, Ewald Weber, Adnan Trakic and Stuart Crozier, Highly accelerated parallel MRI using rotating radiofrequency coil array at 7T, International Society for Magnetic

Resonance in Medicine, 21th scientific meeting and exhibition, Salt Lake City, USA, May 2013, *oral presentation*

Mingyan Li, Jin Jin, Feng Liu, Ewald Weber, Adnan Trakic and Stuart Crozier, Efficient Hybrid imaging reconstruction of sensitivity encoding parallel imaging performed on rotating radiofrequency coil array, *International Society for Magnetic Resonance in Medicine, 21th scientific meeting and exhibition*, Salt Lake City, USA, May 2013, *magna cum laude award*

Mingyan Li, Jin Jin, Feng Liu, Adnan Trakic, Ewald Weber, Stuart Crozier, High Imaging Acceleration with a Rotating Radiofrequency Coil Array at 7T, *5th Asia-Pacific NMR Symposium in conjunction with ANZMAG 2013*, Brisbane, Australia, 2013, *Student poster winner*

Mingyan Li, Thimo Hugger, Ewald Weber, Jin Jin, Feng Liu, Peter Ullmann, Simon Stark, Yasvir Tesiram, Yang Yang, Sven Junge, and Stuart Crozier, A Fast and Practical Imaging Scheme for a Rotating RF Coil at 9.4T by Using Ultra-short TE Sequence in Radial Trajectory, *International Society for Magnetic Resonance in Medicine, 24th scientific meeting and exhibition*, Toronto, Canada, 2015, *oral presentation*

Aurelien Destruel, Jin Jin, Feng Liu, Ewald Weber, **Mingyan Li** and Stuart Crozier, Improving B_1^+ uniformity using segmented dielectric pads, *International Society for Magnetic Resonance in Medicine, 24th scientific meeting and exhibition*, Toronto, Canada, 2015.

Ewald Weber, Adnan Trakic, **Mingyan Li**, Jin Jin, Feng Liu, Stuart Crozier, Rotating Radiofrequency Coil Probe for 11.7T Small animal MRI, 5th Asia-Pacific NMR Symposium in conjunction with ANZMAG 2013, Brisbane, Australia, 2013

Adnan Trakic, Ewald Weber, Jin Jin, **Mingyan Li**, Feng Liu and Stuart Crozier, B1 gradient encoding with the rotating RF coil, International Society for Magnetic Resonance in Medicine, 21th scientific meeting and exhibition, Salt Lake City. 2013, *summa Cum Laude award*

Feng Liu, Jin Jin, **Mingyan Li**, Ewald Weber, Adnan Trakic and Stuart Crozier, On the Reduction of Transmit B1 Non-uniformity and SAR using a Single-loop Rotating RF coil. 34th Annual Meeting of the Bioelectromagnetics Society, Brisbane, Australia, 17-22 June, 2012.

Yu Li, Feng Liu, Ewald Weber, **Mingyan Li**, Wenlong Xu and Stuart Crozier, A Theoretical Study for the Inverse Design of an Ellipsoidal Phased-array Breast Coil, 33rd Annual International Conference of the IEEE Engineering in Medicine and Biology Society (EMBC'11), Boston, USA, 2011.

Publications included in this thesis

Chapter 4: **Mingyan Li**, Zhentao Zuo, Jin Jin, Rong Xue, Adnan Trakic, Ewald Weber, Feng Liu, Stuart Crozier, "Highly accelerated acquisition and homogeneous image reconstruction with rotating RF coil array at 7T-A phantom based study", *Journal of Magnetic Resonance,*Vol. 240, 102-112, 2014

Author contributions

Mingyan Li	Numerical modelling (80%), code implementation (80%), analysis and interpretation (40%), manuscript preparation (100%), experiment implementation (10%)
Zhentao Zuo	Hardware design and manufacture (70%), experiment implementation (70%)
Jin Jin	Numerical modelling (20%), code implementation (20%), analysis and interpretation (20%), manuscript reviews (30%)
Rong Xue	Hardware design and manufacture (20%), experiment implementation (20%)
Adnan Trakic	Analysis and interpretation (10%), manuscript reviews (10%)
Ewald Weber	Hardware design and manufacture (10%), manuscript reviews (10%)
Feng Liu	Analysis and interpretation (20%), manuscript reviews (20%)
Stuart Crozier	Analysis and interpretation (10%), manuscript reviews (30%)

Chapter 5: **Mingyan Li**, Jin Jin, Zhentao Zuo, Feng Liu, Adnan Trakic, Ewald Weber; Yan Zhuo, Rong Xue, Stuart Crozier, *In vivo* Sensitivity Estimation and Imaging Acceleration with Rotating RF Coil Arrays at 7 Tesla, *Journal of Magnetic Resonance,* vol. 252, pp. 29-40, 2015

Author contributions

Mingyan Li	Numerical modelling (80%), code implementation (80%), analysis and interpretation (40%), manuscript preparation (100%).
Jin Jin	Numerical modelling (20%), code implementation (20%), analysis and interpretation (15%), manuscript reviews (20%)
Zhentao Zuo	Hardware design and manufacture (70%), experiment implementation (60%)
Feng Liu	Analysis and interpretation (15%), manuscript reviews (30%)
Adnan Trakic	Analysis and interpretation (10%), manuscript reviews (10%)
Ewald Weber	Hardware design and manufacture (10%), manuscript reviews (10%)
Yan Zhuo	Experiment implementation (20%), manuscript reviews (10%)
Rong Xue	Hardware design and manufacture (20%), experiment implementation (20%)
Stuart Crozier	Analysis and interpretation (20%), manuscript reviews (20%)

Contributions by others to the thesis

Prof. Stuart Crozier (principle supervisor), Associate Prof. Feng Liu (associate supervisor) and Dr Jin Jin (associate supervisor), Mr Ewald Weber (colleague), Dr Yu Li (colleague), Dr Adnan Trakic (colleague), Dr Zhentao Zuo (collaborator), Prof. Rong Xue (collaborator), Prof. Yan Zhuo (collaborator), Dr Thimo Hugger (collaborator), Dr Yasvir Tesiram (collaborator), Dr Peter Ullmann (collaborator), Dr Sven Junge (collaborator), Mr Simon Stark (collaborator), have made contributions towards generating research ideas, experimental design, numerical modelling, data collection and the interpretation of the results. Their individual contributions are detailed in the previous section and are listed at the beginning of Chapters 4–6. All work presented in the remainder of this thesis (Chapters 1, 2, 3 and 6, 7) was drafted entirely by the author. Prior to submission, the thesis was reviewed by all PhD supervisors with corrections being made by the author. This thesis has been edited by Wendy Smith (Chapter 3 to Chapter 7) and Vivienne Chavez (Chapter 1 and 2).

Statement of parts of the thesis submitted to qualify for the award of another degree

None

Acknowledgements

First and foremost, I would like to express my sincere gratitude to my PhD supervisors Prof. Stuart Crozier, A/Prof. Feng Liu and Dr Jin Jin. I am extremely grateful to them for providing me this great opportunity to work in such an excellent research environment. Their valuable advice and generous support accompanied me throughout the course of my PhD. My thanks go to Stuart Crozier for organising regular meetings to discuss interesting research ideas and point out the right research direction with his insightful knowledge. My thanks go to Feng Liu and Jin Jin for always finding the time to discuss my preliminary ideas, in discussions which would sometimes last for hours. The patience, enthusiasm and immense knowledge of my supervisors were priceless treasures throughout my PhD study.

My thanks also go to Mr Ewald Weber and Dr Adnan Trakic for numerous discussions on various aspects of the MRI radiofrequency system. Thanks to them for offering me the opportunity to work with our industry partners, Bruker Biospin (Rheinstetten, Germany). Their creative minds and diligent work have laid a solid foundation for the rotating concept and rotating coil prototype.

Thanks go to Prof. Rong Xue, Dr Zentao Zuo and Prof. Yan Zhan from the Institute of Biophysics of the Chinese Academy of Sciences, for their active collaboration and generous support in building the prototype of the rotating RF coil array and validating it with their state-of-the-art 7 T MRI scanner.

Thanks go to Dr Yu Li for his tuition on electromagnetic simulations and for many discussions on MRI radiofrequency system optimisation. Thanks also go to Kimberley Nunes for her patient and careful tutoring in academic writing. Thanks go to Dr Yeyang Yu, Mr Yang Yang and Dr Limei Liu for many insightful discussions on compressed sensing and gradient coils.

The research in this thesis was funded by a UQ international scholarship. I am also appreciative of financial support in the form of travel grants from the University of Queensland and the International Society for Magnetic Resonance in Medicine.

I would like to say thanks to my Dad and Mum, who have been supportive throughout my life in every way possible. They are my role models. Finally, I thank my wife Zheng Chen for her continuous support, love and understanding. I am lucky to have you in my life.

Keywords

ultra-high field magnetic resonance imaging, 7 Tesla, 9.4 Tesla, rotating radiofrequency coil array, numerical modelling, method of moments, sensitivity estimation, acquisition acceleration, radial trajectory.

Australian and New Zealand Standard Research Classifications (ANZSRC)

ANZSRC code 090304: Medical Devices 50%
ANZSRC code 090399: Biomedical Engineering not elsewhere classified 50%

Fields of Research (FoR) Classification

FoR Code 0903: Biomedical Engineering 60%
FoR Code 0906: Electrical and Electronic Engineering 40%

Table of contents

List of Figures

List of Tables

List of Abbreviations

B_0	Main magnetic field
B_1	Radiofrequency magnetic field
B_1^+	Radiofrequency receive magnetic field
B_1^-	Radiofrequency transmit magnetic field
BOLD	Blood-Oxygenation-Level- Dependent
CP	Circular polarisation
CNR	Contrast-to-noise ratio
CT	Computed tomography
EM	Electromagnetic
EPI	Echo planar imaging
FDTD	Finite-difference time-domain
FEM	Finite element method
FOV	Field of view
GRAPPA	Generalized auto calibrating partially parallel acquisitions
GRE	Gradient echo
IEC	International Electrotechnical Commission
IFFT	inverse fast Fourier transform
MRI	Magnetic resonance imaging
PACs	Phased array coils
PPI	Partially parallel imaging
rpm	revolution per minute
RF	Radiofrequency

ROIs	Region of interests
RRFC	Rotating RF coil
RRFCA	Rotating RF coil array
SAR	Specific absorption rate
SENSE	Sensitivity encoding
SNR	Signal-to-noise ratio
T_1	Longitudinal or spin-lattice relaxation time
T_2	Transverse or spin-spin relaxation time
TE	Echo time
TR	Repetition time
UTE	Ultra-short TE

Chapter 1. Introduction

In this introduction, the radiofrequency (RF) coil related issues of ultra-high field (≥ 7 T) magnetic resonance imaging (MRI) are briefly introduced, and the importance of solving these issues is also outlined. The aim of this project is to develop RF techniques, both new acquisition and reconstruction methods, to mitigate ultra-high field related issues. The outline of this thesis is also summarised from research scope to methodology.

1.1. Problems and motivations

Great efforts have been made to increase the strength of the main magnetic field (B_0) for MRI because of the potential advantages, such as higher signal-to-noise ratio (SNR), increased Blood-Oxygen-Level-Dependent (BOLD) effect and wider applications of X-nuclei (sodium/phosphorus) imaging. Preliminary clinical results have confirmed the advantages of imaging at ultra-high fields [1-7].

However, there are a number of RF field (B_1 field) related issues that come with higher fields. MRI relies on RF coils to transmit and receive MR signals in the form of electromagnetic (EM) waves. However, at ultra-high fields, the wavelength of RF EM waves is shorter than the geometrical size of human body, which forms constructive and destructive interference that in turn manifest as image distortions. This can seriously affect the diagnostic quality of images. The RF energy deposited into the human body is dramatically increased at ultra-high fields, which is proportional to the square of field strength [8]. The overheating may cause tissue damage and thus hinder the clinical use of ultra-high field MRI. Since *in vivo* temperature increases are very difficult to measure, the specific absorption rate (SAR) is used to indicate the RF power dissipation. In addition, long scan duration is a concern for both high and low field MRI. At 7 T, the long scan duration is considered to be the most unpleasant factor [9]. Patients find it hard to remain absolutely still for long periods which leads to motion artefacts that can seriously degrade image quality. A number of studies have been carried out to develop various methods for solving these issues [10-37]. However, there is no accepted standard solution to solve these issues. In order to achieve the promised benefits from ultra-high field MRI, these RF-field related issues need to be addressed.

1.2. Objective and scope

The broad aim of this project is to develop novel RF techniques to solve ultra-high field problems. To date, in terms of hardware, phased array coils are considered to be the best option to implement parallel transmission [23, 24, 31, 36] and parallel imaging [10-13], which are efficient at

mitigating B_1 inhomogeneity while controlling SAR and reducing scan duration. In parallel transmission, the B_1 inhomogeneity and excessive SAR are mitigated by adjusting the magnitude and phase of each transmit channel in conjunction with an RF pulsing design in the spatial and time domains. In parallel imaging, the Generalized Autocalibrating Partially Parallel Acquisition (GRAPPA) algorithm [10] finds coefficients from coils to reconstruct undersampled *k*-space. The SENSitivity Encoding (SENSE) algorithm [11, 12] employs spatial sensitivity information of coils to reconstruct images with partially acquired *k*-space. In order to further improve performance of parallel transmission and parallel imaging, one method is to increase the number of coils. Specifically, with more coils and therefore transmit and receive channels, the parallel transmission has higher degrees of freedom to better homogenise B_1 field and control SAR.

However, the efficiency of this method reduces with an increased number of elements, due to the decreased performance of RF coils, such as stronger coupling and reduced B_1 penetration. On a confined surface, the coil size is necessarily smaller and mutual couplings are increased with a larger number of coils; the smaller coil size also leads to a shallower B_1 penetration. These could reduce the efficiency of parallel transmission and parallel imaging, because coils are less efficient in modulating inhomogeneous B_1 field and receiving signals at some (particularly deep) regions. Some studies have demonstrated the limitation of using phased array coils for improving the performance of parallel transmission [23, 24, 36] and parallel imaging [38, 39]. Alternatively, a recently developed single element rotating RF coil (RRFC) [40, 41] has proved to be capable of reducing scan time for *in vivo* imaging at low fields. With only one coil element, the coil size is big and there is no coupling, which improves the coil performance. However, with only one coil, the imaging acceleration strategy of the RRFC requires an increase of rotation speed and analogue-to-digital (ADC) sampling rate, which could be limiting factors especially for large volume coils. Phased array coils and the RRFC have complementary advantages, thus combining two techniques could synergize each other's strengths and offset their disadvantages.

The specific aim of this thesis is to develop rotating techniques that strategically combine the physically rotated coil concept and general array structures to better solve ultra-high field issues. Specifically, benefitting from rotation, each coil is capable of acquiring a large number of transmit and receive profiles for parallel transmission and parallel imaging, which allows the use of fewer but larger coils. Coils in such a rotating RF coil array (RRFCA) have lower coupling and deeper B_1 penetration which improves the performance of B_1 shimming and acquisition acceleration. In addition, with the extra degrees of freedom introduced from rotating, the B_1 shimming and SAR control could be achieved with relatively simple methods without complex pulsing design. With multiple rotating elements, imaging acceleration is achieved without modulating the rotation speed.

New algorithms based on SENSE that employ abundant rotation-dependent sensitivity maps can be developed to better accelerate acquisitions and reconstruct images.

An important aspect of any new acquisition method is to ensure rapid image reconstruction that is achievable on the host computer of the MRI system. This ensures clinical workflow. A further aim of this thesis is to investigate the use of efficient reconstruction algorithms that are appropriate for the data generated by the rotating array system. One promising avenue is the use of radial *k*-space acquisition trajectories, in combination with a novel artefact suppression and on-line reconstruction algorithm. A new rapid imaging scheme based on the use of radial trajectory acquisitions and related reconstruction methods in combination with rotating techniques will also be investigated.

1.3. Thesis overview

In **Chapter 2**, the theoretical improvement of the MRI signal at ultra-high fields is analysed and various clinical applications are investigated. These mathematical derivations and clinical validations are strong evidence of the ultra-high field MRI outperforming lower fields. The clinical benefits emphasise the importance of solving technical issues to benefit from ultra-high field MRI.

In **Chapter 3**, the technical issues and the existing solutions are reviewed. Demonstrated with simulation results and clinical images, these RF-field related issues are shown to be a serious obstacle for successfully implementing clinical ultra-high field MRI. This strengthens the aim of this project to develop novel RF techniques for solving ultra-high field issues and facilitating clinical applications.

In **Chapters 4** and **5**, the RRFCA and corresponding algorithms are developed with numerical models and then validated with a homogenous phantom. Afterwards, the feasibility of using the RRFCA will be tested on human subjects. In **Chapter 4**, assisted by the numerical modelling, the structure of the RRFCA is first optimised, and then the B_1 shimming strategy is investigated when the extra degrees of freedom is introduced by rotation. The acquisition acceleration and reconstruction algorithms are also developed in this chapter. In **Chapter 5**, in order to use the RRFCA for human brain imaging, the rotation-dependent sensitivities need to be accurately estimated. Therefore, a registration technique based *in vivo* sensitivity estimation algorithm is developed and validated with human subjects.

In order to extend the applications and improve practicability of the RRFCA, a new imaging scheme is developed in **Chapter 6** by employing radial trajectories. By characterising artefacts caused by coil rotation, this method can reconstruct images with a customised algorithm without

mapping any transmit/receive sensitivity, therefore saving time on sensitivity calibrations and extending the rotating technique to applications that requires immediate image output.

In **Chapter 7**, this thesis will be concluded with a summary of the advantages of the rotating technique over conventional techniques, in terms of solving ultra-high field issues. In addition, the future work of using the RRFCA for wider applications will be discussed.

Chapter 2. Benefits of ultra-high field MRI

As one of the most important imaging modalities with various clinical applications, MRI has become widespread with over 25,000 scanners in use worldwide [42]. When looking back at the history of MRI, there is a clear trend of pushing the main magnetic field (B_0) to higher strengths. The first clinical MRI scanner started with 0.35 T in 1983, which then rose to 1.0 T and 1.5 T in the late 1980s. High field MRI systems were tested in 1990s and 3 T became the highest permitted field strength for clinical use in 2002. Ultra-high field (≥7 T) MRI systems became available in the late 90s.

The promised SNR improvement is one of the primary drives to increase the strength of the main magnetic field (B_0). Besides the SNR increase, the signal sensitivity of functional MRI (*f*MRI) and X-nuclei are also considered higher at ultra-high fields. In this chapter, the mathematical derivations and clinical applications will be used to demonstrate the benefits of ultra-high field MRI.

2.1. Theoretical analysis of SNR dependency on B_0

In order to reveal the relationship of the MRI signal and field strength, it is necessary to analyse the MR signal at an elementary level. The nuclear magnetic resonance (NMR) phenomenon is an ensemble effect of elementary particles in a volume of substance. Generally, the MRI signal is generated with three essential conditions, namely, spin, external magnetic field and RF EM waves. In the first part of this chapter, these factors and their relationships to the MR signal are mathematically analysed.

2.1.1. The magnetisation and its dependency on B_0

The spin and the strong external magnetic field generate the magnetisation, M_0, which is considered to be the maximum amount of MRI signal that can be received. Spin is an intrinsic property of elementary particles, composite particles and atomic nuclei [43, 44]. As shown in Figure 2-1 (a), a spinning proton can possess a magnetic dipole moment. Atomic nuclei with an odd number of protons have a non-zero net magnetic moment. The magnetic moment μ of the proton is related to the quantised angular momentum [45]:

$$\mu = \gamma \hbar I \tag{2.1}$$

where $\hbar$ is the Planck constant divided by 2π (1.055×10^{-34} *Joules*); and γ is the gyromagnetic ratio; for the proton, the value of γ is $2.68\times10^{8} rad\cdot s^{-1}\cdot Tesla^{-1}$. I is the angular momentum quantum number, which is in multiples of 1/2 and can be + or -. I= ½ for proton. With the presence

of the external magnetic field, the proton only has two possible states with a quantum number of $-1/2$ and $1/2$.

The human body is made up of over 60% of water; therefore hydrogen protons are abundant in various soft tissues, such as muscles and brain. Under normal circumstances (i.e. no external magnetic field), the spin orientations of hydrogen protons in a sample are randomised as shown in Figure 2-1(b); consequently, the net magnetic moment in a sample is close to zero. However, under a strong external magnetic field, the hydrogen protons will experience forces and align with the magnetic field in two orientations as shown in Figure 2-1(c): parallel or anti-parallel.

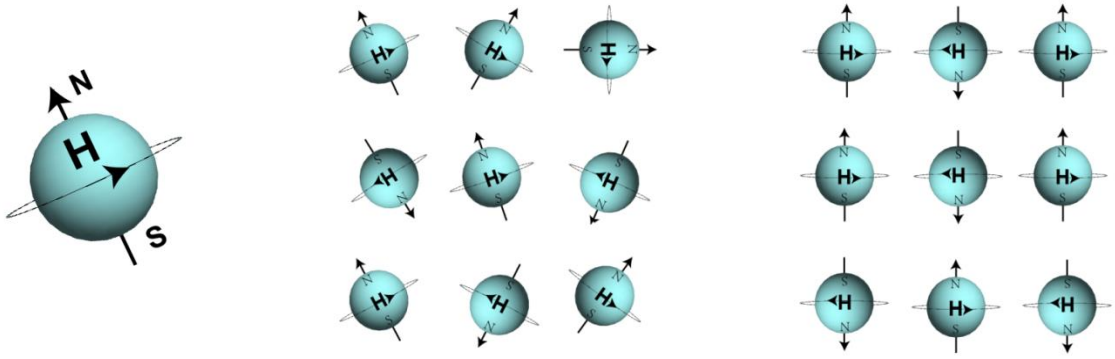

(a) (b) (c)

Figure 2-1. (a) Illustration of magnetic dipole induced by spin of the hydrogen proton; (b) hydrogen protons without external magnetic field, and (c) hydrogen protons align with the external magnetic field in parallel or anti-parallel direction.

The alignment direction is determined by the energy levels of a proton. The protons with higher energy level align to the magnetic field in an anti-parallel direction while low energy protons align in a parallel direction. Their energies are calculated in Eq. 2.2(a) and Eq. 2.2(b). More protons orient parallel than anti-parallel; therefore the difference of ensemble magnetic moments generates a net magnetisation along the B_0 direction, namely the magnetisation M_0.

The Zeeman energies *E* of the hydrogen protons spinning in two directions are calculated as Eq. 2.2 a and 2.2 b [46], the difference of these two energy state ΔE is calculated as Eq. 2.2 c.

$$E_{parallel} = \mu B_0 = -\frac{1}{2}\hbar\gamma B_0 \tag{2.2a}$$

$$E_{anti-parallel} = \mu B_0 = \frac{1}{2}\hbar\gamma B_0 \tag{2.2b}$$

$$\triangle E = E_{anti-parallel} - E_{parallel} = \hbar\gamma B_0 \tag{2.2c}$$

In order to calculate the magnetisation M_0, it is necessary to know the number of excessive protons. According to the Boltzmann distribution and Eq. 2.2(c), the number of spins aligned with B_0 ($N_{parallel}$) versus against B_0 ($N_{anti-parallel}$) is calculated as:

$$\frac{N_{anti-parallel}}{N_{parallel}} = e^{\frac{-\Delta E}{kT}} = e^{\frac{-\hbar\gamma B_0}{kT}} \tag{2.3}$$

where *k* is the Boltzmann constant (1.38×10^{-23} $Joules/\mathrm{K}$) and *T* is the absolute temperature. At body temperature, since the $\hbar\gamma B_0 \ll KT$, the number of protons that can generate the MR signal (N_{excess}) is derived as [47]:

$$N_{excess} = N_{parallel} - N_{anti-parallel} \approx \frac{N_{total}}{2} \cdot \frac{\hbar\gamma B_0}{KT} \tag{2.4}$$

where N_{total} is the total number of the protons in the excited volume. With a known proton density of unit volume ρ, the magnetisation M_0 can be calculated as [48]:

$$M_0 = \frac{\hbar\gamma}{2}\frac{\rho\hbar\gamma B_0}{2KT} = \frac{\rho\hbar^2\gamma^2 B_0}{4KT} \tag{2.5}$$

Eq. 2.5 indicates that in the same sample, the strength of magnetisation M_0 is proportional to the strength of the applied external magnetic field. The MR signal source is proportional to the number of excessive low energy protons (parallel) over the high energy protons (anti-parallel), which is only 3 protons per million per Tesla, at body temperature [49]. The straightforward method to improve the SNR is to increase the number of MR signal sources; namely, increase the main magnetic field strength B_0 . However, the MR signal strength is also closely related to the conditions during transmission and reception.

2.1.2. MR signal excitation and reception

When placing certain nuclei in a magnetic field, the nuclei absorb and emit RF energy while the RF power is on and off [50]. Working independently, Block et al. [51] and Purcell et al. [52] detected this proton magnetic resonance phenomenon in liquid water and solid paraffin, respectively. The frequency of the RF wave matches the external magnetic field according to the Larmor equation:

$$\omega_0 = \frac{\triangle E}{\hbar} = \gamma B_0 \tag{2.6}$$

where the ω_0 is normally referred to as the Larmor precessional frequency. The gyromagnetic ratio and resonant frequency of several commonly imaged isotopes are listed in Table 1.1.

Table 1-1 Gyromagnetic ratio and resonant frequency of several commonly measured isotopes [47]

	Gyromagnetic ratio (MHz)	Resonant frequency at 1.5 T	Resonant frequency at 3 T	Resonant frequency at 7 T
^{1}H	42.58	63.87 MHz	127.74 MHz	298.06 MHz
^{31}P	17.24	25.86 MHz	51.72 MHz	120.68 MHz
^{23}Na	11.26	16.89 MHz	33.78 MHz	78.82 MHz
^{19}F	40.05	60.01 MHz	120.02 MHz	280.35 MHz

During excitation, the low energy protons (parallel) absorb the RF energy and jump to the high energy level (anti-parallel); consequently, the collective net magnetisation is a spiral movement as shown in Figure 2-2 (a). Only the magnetisation in the XY plane is an effective MR signal that can be received. In Figure 2-2 (b), M^+ is the projection of flipped magnetisation M_0 in the XY plane and θ is the flip angle.

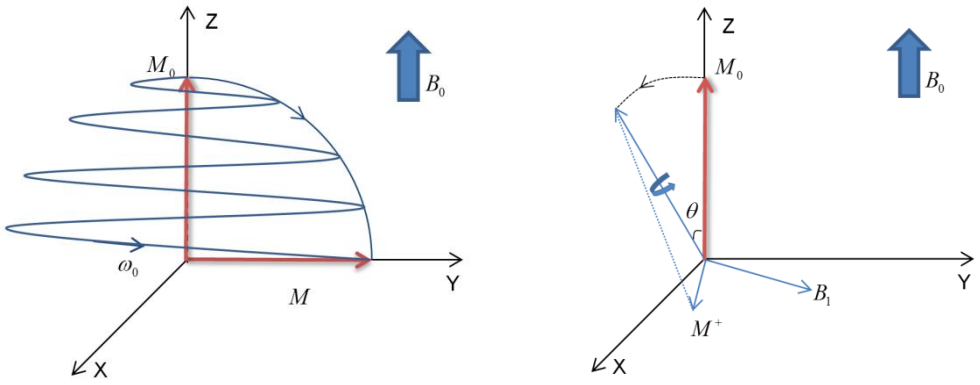

(a) (b)

Figure 2-2. (a) Net magnetisation $\boldsymbol{M_0}$ is flipped by RF waves. (b) Illustration of flip angle in the rotating frame of reference.

The flip angle θ is directly related to the RF pulse as [53]:

$$\theta = \gamma |B_1| \tau \tag{2.7}$$

where the τ is the RF pulse duration and $|B_1|$ is the magnitude of the spatial distribution of the RF magnetic field. The MRI signal generated from the transverse component (M^+) of the flipped magnetisation M_0 is therefore calculated as:

$$M^+ = M_0 \sin(\theta) = M_0 \sin(\gamma |B_1| \tau) \tag{2.8}$$

When the RF pulse is removed, protons will experience forces to return to their original states, and the flipped magnetisation will return to equilibrium M_0. According to Faraday's Law, if a receiver is placed orthogonal to the XY plane, a current will be generated in the loop. The measured voltage signal is called free induction decay (FID) and is shown in Figure 2-3.

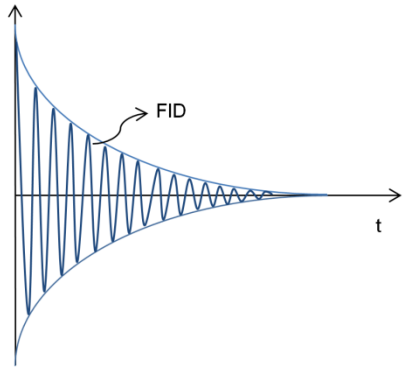

Figure 2-3. The FID signal before sending to a mixer.

In Eq. 2.8, the flipped magnetisation M^+ is the maximum amount of signal that a coil can receive, despite of the efficiency of reception. It is clear that besides M_0, the received MR signal is also proportional to the RF magnetic field distribution B_1 and RF pulse duration τ. Due to the complex coil-subject interaction, the B_1 distribution becomes subject-dependent at ultra-high field. The receive ability of the RF coil and the noises also affect the SNR of the final image. In the next section, all these factors will be considered in order to derive the SNR dependency on B_0.

2.1.3. SNR dependency on B_0

2.1.3.1. Intrinsic signal dependency on B_0

When the RF power is removed, the flipped magnetisation returns to its original state. The magnetic flux passing through a closed loop l (RF coil) will induce an electromagnetic field (ξ). The electromagnetic voltage received by the RF coil is calculated according to Faraday's Law [54]:

$$\xi = \oint_l \vec{E} \cdot dl = -\frac{d\Phi}{dt} \tag{2.9}$$

The total magnetic flux Φ is determined by the concept of reciprocity [55]:

$$\Phi(\mathrm{t}) = \int_{sample} \overrightarrow{B_1}(\mathrm{t}) \cdot \overrightarrow{M^+}(\mathrm{t})\, dV \tag{2.10}$$

where $\overrightarrow{B_1}$ denotes the magnetic field produced by the RF coil to generate the time-dependent flipped magnetisation $\overrightarrow{M^+}(\mathrm{t})$ and V denotes the volume. Combining the Eqs. 2.9 and 2.10, the voltage signal received by the coil is:

$$\xi = -\frac{d}{dt} \int_{sample} \overrightarrow{B_1}(\mathrm{t}) \cdot \overrightarrow{M^+}(\mathrm{t})\, dV \tag{2.11}$$

The RF coil is placed parallel to the z-axis, in which it generates a B_1 field that is perpendicular to B_0 during transmission. Therefore, during decay, the RF coil will only receive signals in the transverse plane from the X-axis and Y-axis component of the M^+, namely, the M_x^+ and M_y^+. The partial solutions of the Bloch Equation in the transverse plane are [51]:

$$M_x^+(\mathrm{t}) = e^{-t/T_2}\left(M_x^+(0)\cos\omega_0\,\mathrm{t} + M_y^+(0)\sin\omega_0\,\mathrm{t}\right) \tag{2.12a}$$

$$M_y^+(\mathrm{t}) = e^{-t/T_2}\left(M_y^+(0)\cos\omega_0\,\mathrm{t} - M_x^+(0)\sin\omega_0\,\mathrm{t}\right) \tag{2.12b}$$

where ω_0 is the Larmor frequency; T_1 and T_2 are the longitude and transverse relaxation time. Substituting Eq. 2.12 into Eq. 2.11, the signal acquired by the receiver is illustrated as below:

$$\begin{aligned} signal &\propto -\frac{d}{dt}\int [B_{1\mathrm{x}} M_x^+ + B_{1y} M_y^+]\, dV \\ &\propto \omega_0 \int \mathrm{e}^{-t/T_2}\mathrm{M_{xy}}[B_{1\mathrm{x}}\sin(\omega_0 t - \phi_0) + B_{1y}\cos(\omega_0 t - \phi_0)]\, dV \end{aligned} \tag{2.13}$$

where $B_{1\mathrm{x}}$ and B_{1y} are the components in the X- and Y-axis and calculated as:

$$\begin{aligned} B_{1\mathrm{x}} &= B_1 \cos\theta_B \\ B_{1y} &= B_1 \sin\theta_B \end{aligned} \tag{2.14}$$

Substituting Eq. 2.14 into Eq. 2.13 and with the trigonometric relation:

$$sin(a+b)=sin(a)cos(b)+cos(a)sin(b) \tag{2.15}$$

The intrinsic signal is obtained as Eq. 2.16:

$$signal \propto \omega_0 \int e^{-t/T_2} \cdot M_{xy} \cdot B_1 \cdot \sin(\omega_0 t + \theta_B - \phi_0) \cdot dV \tag{2.16}$$

where M_{xy} is the projection of the net magnetisation on the transverse plane:

$$M_{xy} = M^+ = M_0 \sin(\theta) \tag{2.17}$$

Substituting Eq. 2.17 with Eq. 2.16, the intrinsic signal in the sample is obtained as:

$$\begin{aligned} signal &\propto \omega_0 \int e^{-t/T_2} \cdot \frac{\rho \hbar^2 \gamma^2 B_0}{4KT} \cdot \sin(\theta) \cdot B_1 \cdot \sin(\omega_0 t + \theta_B - \phi_0) \cdot dV \\ &\propto B_0^2 \end{aligned} \tag{2.18}$$

Eq. 2.18 indicates an increase of the MR signal with a higher main field B_0. However, in order to characterise the SNR, it is also important to analyse the dependency of noise behaviour on B_0.

2.1.3.2. Noise dependency on B0

The noise in MRI is generated by the thermal motion of the charges and dipoles inside the sample and coil [8]. It is characterised by the Nyquist's equation [56]:

$$V_{noise} = \omega \sqrt{4kT \triangle \omega R} \tag{2.19}$$

where T is the absolute temperature in Kelvin; $\triangle \omega$ equates the bandwidth of the receiver. R is the effective resistance in the sample (R_{sample}) and the coil (R_{coil}) which is hard to calculate accurately. However, the dissipated power P can be calculated as $P=I^2R$, and calculating the power loss of the RF coil port (P_{coil}) can indicate the noise level. Therefore, Eq 2.19 can be written as:

$$V_{noise} = \sqrt{4KT_{coil} \triangle \omega P_{coil} + 4kT_{sample} \triangle \omega P_{sample}} \tag{2.20}$$

For a good conductor, the penetration depth δ is calculated as:

$$\delta = \sqrt{\frac{2}{2\pi w_0 \mu_c \sigma_c}} \tag{2.21}$$

where μ_c and σ_c are the magnetic permeability and electrical conductivity of the conductor, respectively. The resistance of the coil is [8]:

$$R \approx Length / \sigma_c 2\pi\rho\delta \tag{2.22}$$

Knowing that the power calculation is dependent on the electrical current and resistance, combining Eqs. 2.21 and 2.22, resulting in the following [8]:

$$P_{coil} = I^2 R \approx I^2 \cdot Length / \sigma_c 2\pi\rho\delta \propto \sqrt{B_0} \tag{2.23}$$

The power dissipated into the sample is calculated as $P_{sample} = \sigma_c E^2$ and according to Faraday's law in time-harmonic form:

$$\oint_l \vec{E} \cdot d\vec{l} = -2\pi j v \int_s \vec{B} \cdot d\vec{s} \tag{2.24}$$

From Eq. 2.24, it is seen that $E \propto v$, and thereby

$$P_{sample} \propto E^2 \propto B_0^2 \tag{2.25}$$

2.1.3.3. SNR in low, mid and high fields

SNR in low field

At low field (≤1T), the B_1 distribution is independent to the B_0 due to the much longer wavelength than the dimension of the subject. Therefore, combining the Eq. 2.17 – Eq. 2.25, the *SNR* at low field can be written as:

$$\frac{V_{signal}}{V_{noise}} \propto \frac{B_0^2}{\sqrt{aB_0^{1/2} + bB_0^2}} \tag{2.26}$$

where *a* and *b* scale the noise contribution from coil and sample, respectively. As the $B_0 \rightarrow 0$, the noise contribution from the coil will dominate, that is $aB_0^{1/2} \gg bB_0^2$ [8]. Thus the SNR at low fields can be approximated as [55]:

$$\frac{V_{signal}}{V_{noise}} \propto \frac{B_0^2}{\sqrt{aB_0^{1/2}}} \propto B_0^{7/4} \tag{2.27}$$

SNR in mid-field

At mid-field (1 T − 3 T), the B_1 distribution is still independent of B_0; however, as the field strength is stronger than 1.5 T, the sample noise starts to dominate according to Eq. 2.25, and the SNR is approximately [57]:

$$\frac{V_{signal}}{V_{noise}} \propto \frac{B_0^2}{\sqrt{bB_0^2}} \propto B_0 \tag{2.28}$$

SNR in high field

The RF wavelength inside the human body becomes a fraction of the size of the subject at high field (>3 T), and the *SNR* is closely related to the B_1 distribution in a volume [58]:

$$\frac{V_{signal}}{V_{noise}} \propto \frac{\int_{VOI} WB_0^2 \sin(\tau V \gamma \left|B_1^+\right|)\left|B_1^-\right| dv}{\sqrt{P_{sample}}} \tag{2.29}$$

where W is a weighting factor related to tissue and sequence. B_1^+ is the excitation profile proportional to the flip angle and B_1^- is the coil reception profile, illustrating the coil's receive ability. B_1^+ and B_1^- are calculated as [53]:

$$B_1^+ = \frac{B_x + iB_x}{2} \tag{2.30a}$$

$$B_1^- = (\frac{B_x - iB_y}{2})^* \tag{2.30b}$$

where B_x and B_y denote the position dependent complex magnetic field quantities; i is the imaginary unit and the asterisk indicates the complex conjugation.

According to Eq. 2.25, the Eq. 2.29 can be modified as:

$$SNR \propto B_0 \sin(\tau V \gamma \left|B_1^+\right|)\left|B_1^-\right| \tag{2.30}$$

Eq. 2.30 indicates that at high field, the SNR increases with B_0; however, the transmit and receive profiles need to be homogenous to make this increase meaningful. The B_1 inhomogeneity and mitigation strategy will be illustrated in Chapter 3.

2.1.4. Benefits of functional MRI (fMRI) with increased B_0

As one of the primary application of ultra-high field MRI, *f*MRI investigates the brain activity by detecting the changes of blood flow [59]. In 1990, a series of experiments carried out by Ogawa et al. [60] demonstrated the ability of MRI to detect and image the magnetic property changes in oxygenated and deoxygenated blood. The acronym "BOLD" was used to describe this Blood-Oxygen-Level Dependent effect, which has underpinned thousands of studies for non-invasive *f*mri [61].

The BOLD signal is detected from magnetic property changes when haemoglobins are oxygenated and deoxygenated. Neurons cannot store oxygen internally; therefore, during activation, haemoglobins release their oxygen to neurons and become deoxygenated. The deoxygenated haemoglobins are strongly paramagnetic, in contrast to the diamagnetic oxygenated haemoglobins. This net change in the magnetic susceptibility causes a magnetic field distortion in and around the blood vessels. Such susceptibility changes cause dephasing of the MRI signals and attenuates the signal intensity, leading to darkened pixels in a T_2* weighted image.

As explained above, the spatial SNR increases with the field strength and the BOLD contrast is theoretically stronger from the microvasculature. Therefore, the BOLD effect at higher fields should be more sensitive than that of lower fields. The BOLD sensitivity (BS) is expected to be maximised for best *f*MRI image quality, which is calculated as [61]:

$$BS = \frac{tCNR}{\sqrt{TR_{volume}}} \tag{2.31}$$

where *tCNR* denotes the temporal contrast-to-noise ratio. The TR_{volume} is the volume repetition time, which is constant with the same sequence parameters. The *tCNR* is calculated as [61]:

$$tCNR \approx \frac{TE \cdot \Delta R_2}{\sqrt{\frac{1}{SNR_0^2} + \lambda^2}} \tag{2.32}$$

where the SNR_0 increases with the B_0 and λ is constant and independent of B_0 [62]. The TE is chosen to match the tissue T_2*. R_2 is the relaxation rate ($1/T_2$*) and for the gradient echoes, the R_2 is replaced as R_2*. Theoretically, the ΔR_2 (*) increases linearly with B_0 linearly for large veins and quadratically for microvasculature [63]. Experimentally, it is proven that the ΔR_2 (*) increase is supra-linear and linear for large veins and linear and super-linear for grey matter [3, 64, 65].

2.2. Clinical applications

In the previous section, the improvement of SNR and BOLD sensitivity with higher field strength has been mathematically derived. In this section, clinical images acquired at 3 T and 7 T are presented and compared to demonstrate the clinical benefits from ultra-high field MRI. The intrinsic higher SNR allows the visualisation of small lesions that normally have ambiguous boundaries and details shown in images acquired at lower field. In addition, the higher SNR is immediately transferred into higher spatial resolution without a clearly elevated noise level. These advantages are extremely useful for detecting and diagnosing disease at an early stage. The

improved BOLD sensitivity also facilitates the characterisation of brain activities. Clinical images of cerebrum, blood vessels, breast, musculoskeletal system and *f*MRI are exhibited to demonstrate the above mentioned advantages of ultra-high field MRI. Additionally, the new application for X-nuclei imaging is also presented to demonstrate the wider application of ultra-high field MRI.

2.2.1. Morphological imaging

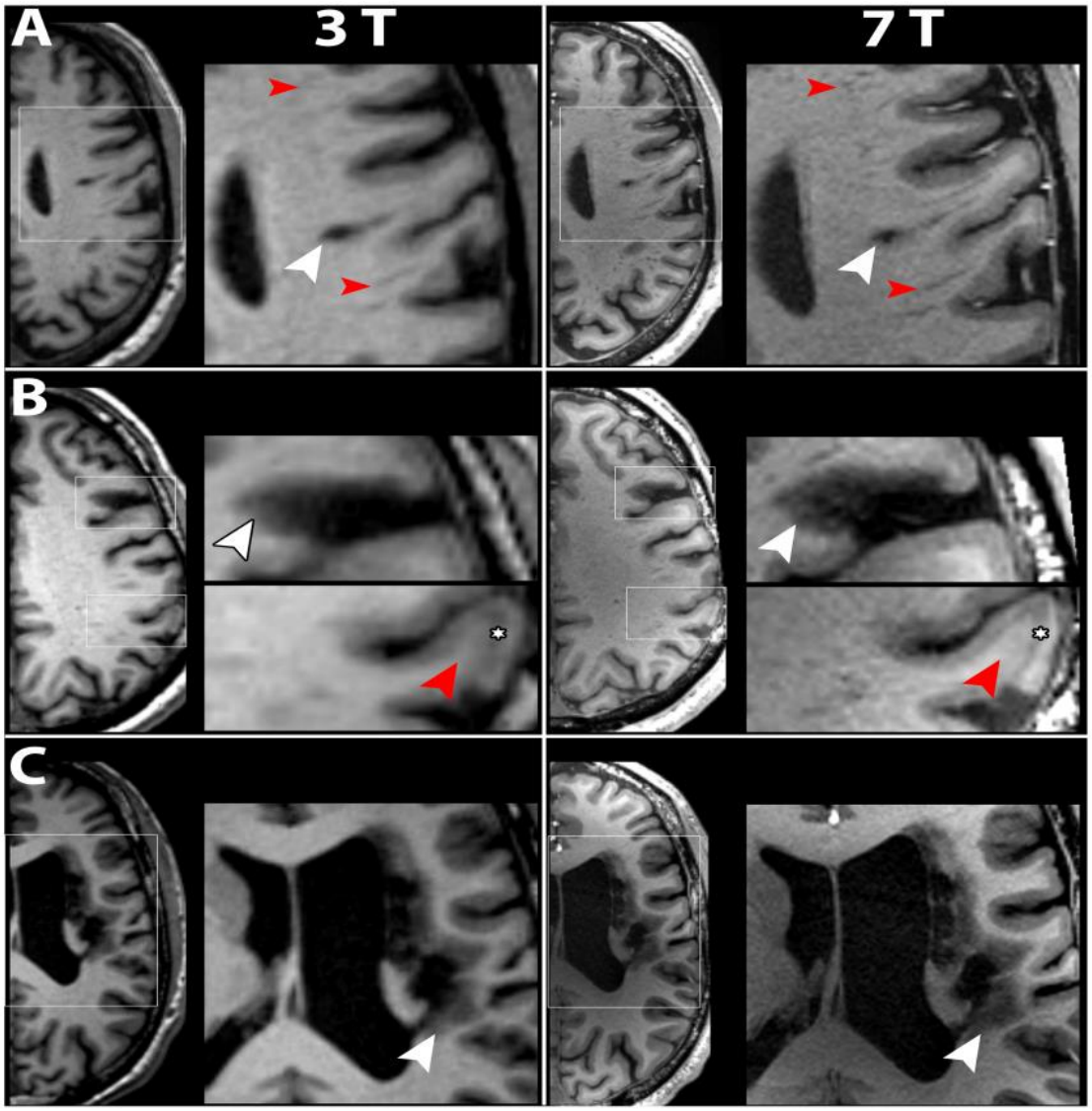

Figure 2-4.The Magnetisation-Prepared RApid Gradient-Echo (MP RAGE) images at 3 T and 7 T for patients A, B and C [1]. (Reproduced with permission.) Patient A: tissue defect areas are marked with white arrowheads and the Virchow-Robin spaces are marked with red arrowheads. Patient B: The chronic lesions are marked with white arrowheads and the sub-acute lesions were marked with red arrowheads. The cortical bands are marked with asterisks. Patient C: Small white matter lesions are marked with red arrowheads.

As MP RAGE is one of the most popular sequences for structural brain imaging [66], it was used to acquire brain images at 3 T and 7 T, respectively. In Figure 2-4, brain images acquired from three different patients are compared and the boxed areas are magnified for better visual comparison [1]. In patient A, the tissue defect area (white arrowheads) was larger and better confined at 7 T. The Virchow-Robin space (red arrowheads) was also easier to be detected with more details at 7 T. In patient B, the chronic lesion (white arrowheads) presented as a disruption of the cortical band, was better depicted with clearer boundaries and more details in the 7 T image. The area marked with red arrowheads indicated a sub-acute lesion, which was not well characterised and shown with ambiguous details in the 3 T image. However, benefited from a higher SNR and resolution at 7 T, the sub-acute lesion can be clearly detected. In addition, the cortical band can also be characterised as a superficial hyperintense layer and a deeper hypointense layer (asterisk) [1]. In patient C, the large infarct marked with white arrowheads, the differentiation of healthy tissue and hypointense gliosis was much easier at 7 T with richer details and clearer boundaries.

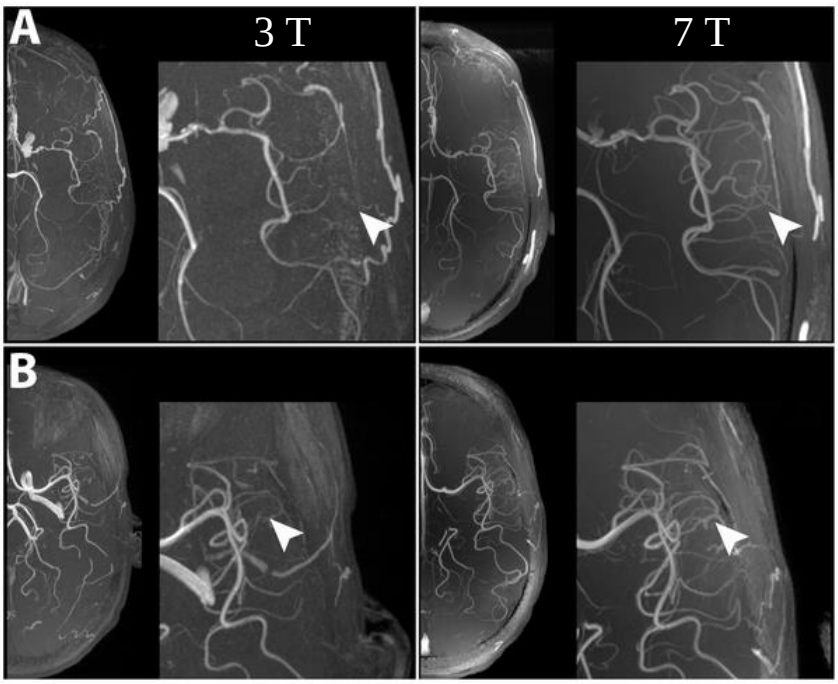

Figure 2-5. Angiography images for patients A and B at 3 T (left column) and 7 T (right column) [1] (Reproduced with permission).

In Figure 2-5, angiography images of two patients were acquired using the time-of-flight (TOF) method at 3 T and 7 T, respectively. Compared to images in the left column, the images obtained at 7 T not only have a lower global noise level, but also the branches of the main cerebral arteries are well depicted. The details of arteries marked by white arrows in both patients can be barely seen 3 T whilst the images acquired at 7 T clearly reveal the small arteries.

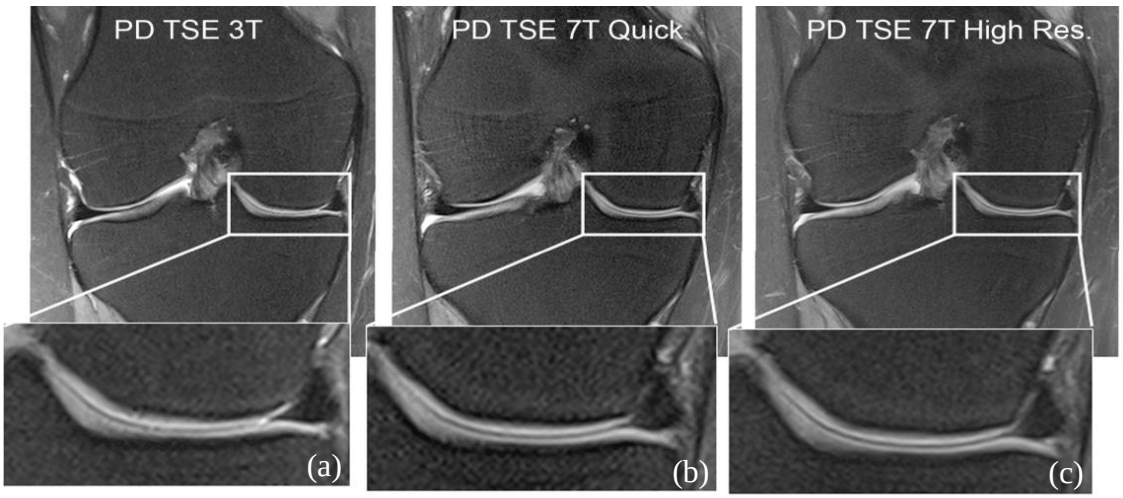

Figure 2-6. Knee images obtained at 3 T (a) and 7 T (b and c) with proton density (PD) turbo spin echo (TSE) sequence. The femoral condyle with meniscus is enlarged for better visualisation of the image quality [2]. (Reproduced with permission.)

The Figure 2-6 (b) was obtained at 7 T with a shorter scan time but the same resolution as the 3 T image in Figure 2-6 (a). The image quality of Figure 2-6 (b) is comparable to Figure 2-6 (a), both globally and locally. The image in Figure 2-6(c) was acquired with the same scan time as the 3 T image in Figure 2-6 (a). In this application, with the same scan time, the 7 T image clearly has less noise (white dots) than 3 T. The cartilages at the femoral condyle and meniscus are better characterised and more easily segmented.

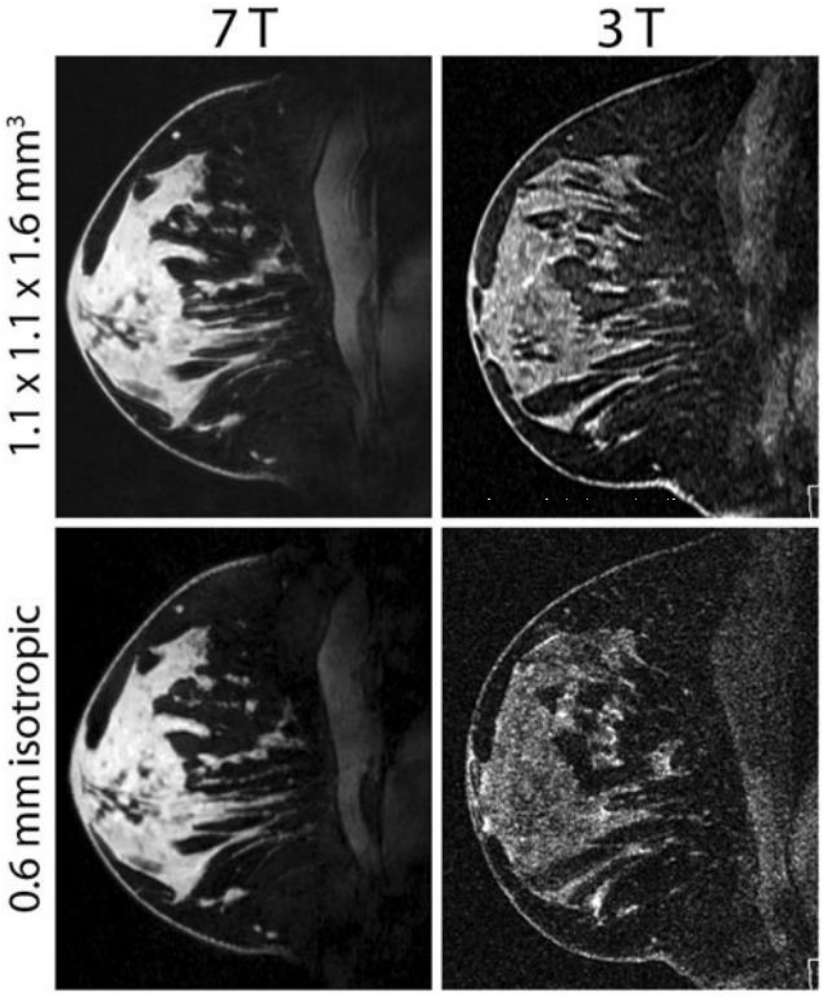

Figure 2-7. Comparisons between 3 T (right column) and 7 T (left column) breast images from the same subject with standard resolution (top row) and high resolution (bottom row) obtained with T1-weighted fat suppression (FS) sequence [4]. (Reproduced with permission.)

MRI has inherent higher sensitivity of soft tissue than mammography or ultrasound, offering better image quality regardless of the breast density [67, 68]. At higher fields, this advantage can be further enhanced. With a $1.1 \times 1.1 \times 1.6$ mm^3 voxel size, the 7 T image in the first row of Figure 2-7 [4] has lower background noise and more detail than that of the 3 T image. The higher SNR of 7 T can be employed to increase the spatial resolution and facilitate clinical diagnosis. When the voxel size is 0.6 mm isotropic, the 7 T image was capable of clearly revealing dendritic patterns and ligaments without noise. In contrast, the 3 T image was contaminated by noise and the details were not clearly visible. The significantly higher image quality of ultra-high field MRI facilitates the clinical diagnosis with greater accuracy and a higher possibility of detecting small lesions at early stages of cancer, therefore increasing the survival rate.

2.2.2. fMRI

In addition to the increased SNR for morphological imaging, the BOLD sensitivity is also increased as illustrated in Eq. 2.31 and Eq. 2.32. Images and statistic data acquired at 3 T and 7 T are compared to demonstrate the superior advantages of ultra-high field MRI in *f*MRI applications.

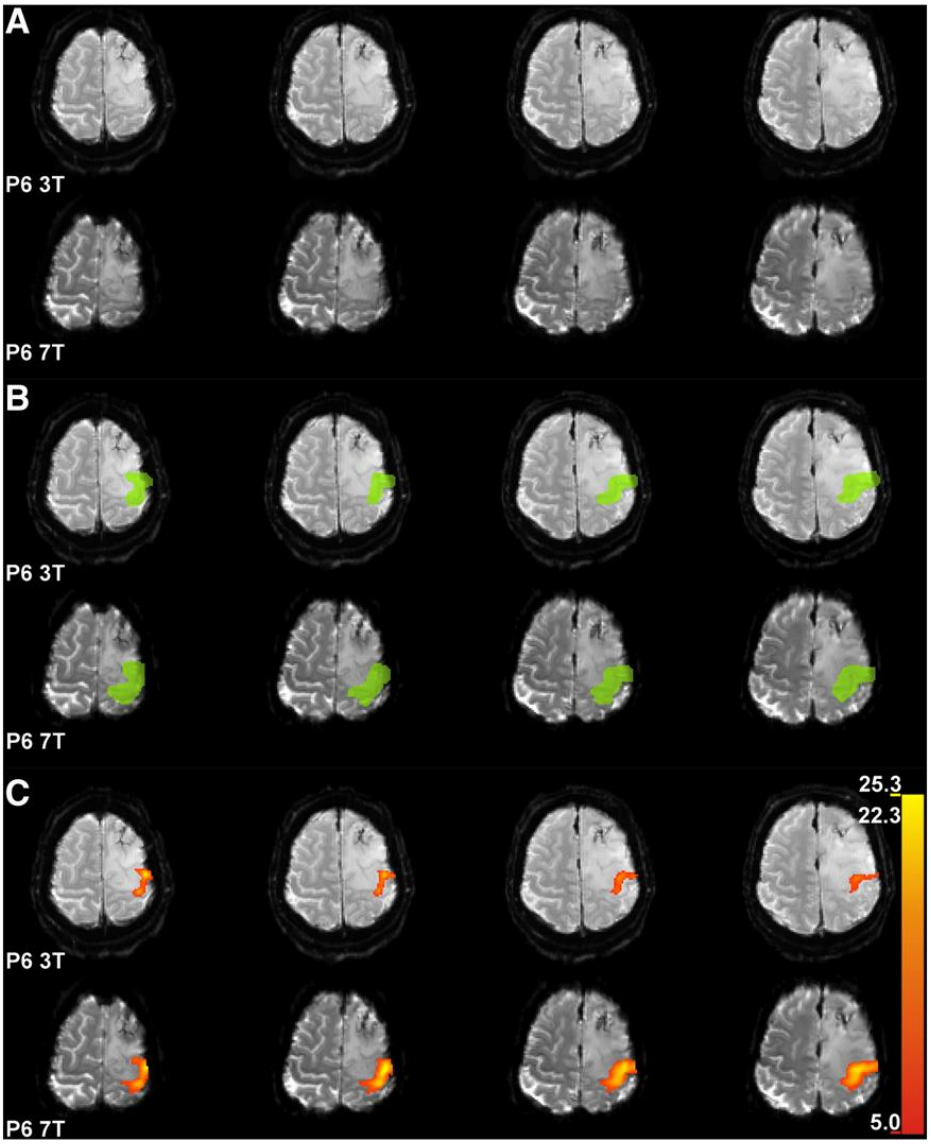

Figure 2-8. Functional Echo planar imaging (EPI) slices covering central parts of the primary motor hand area at 3 T and 7 T [6]. (A) Morphological EPI images. (B) Detected primary motor hard areas. (C) Region of interests (ROIs) of suprathreshold voxels. (Reproduced with permission).

In each group of comparisons, images shown in the top rows were obtained from 3 T and images in the bottom rows were obtained from 7 T. The 3 T (top row) and 7 T (bottom row) EPI images are shown in group A. In group B, light green neuroanatomical ROIs depict the primary motor hand area at 3 T (top row) and 7 T (bottom row). Larger areas are seen in the 7 T images, which indicate higher *f*MRI signal sensitivities than that of 3 T. Quantitative comparisons are

shown in Figure 2-8(C), suprathreshold voxels (p <= 0.05) within which the neuroanatomical ROIs are marked. With higher signal sensitivity at 7 T, both the area and the maximum t-value of the active voxels are larger than that of 3 T ($Max_{t-value,3T} = 22.3$, $Max_{t-value,7T} = 25.3$).

Table 2-1. Statistical measurements of *f*MRI at 3 T and 7 T

Measure	3 T value (SD)	7 T value (SD)
Voxel count	666 (292)	896 (385)
Mean t-value	10.7 (2.4)	11.6 (2.1)
Peak t-value	24.7 (8.0)	25.6 (6.6)
Signal change (%, mean of *f*ROI)	1.8 (0.5)	2.3 (0.7)
Contrast to noise ratio(CNR)	3.3 (0.7)	4.3 (0.8)
Peak CNR	9.7 (3.2)	13.0 (3.3)

Beisteriner et.al [6] conducted and compared statistical measurements of *f*MRI parameters of 17 patients for 3 T and 7 T, respectively. The data were used to provide a quantitative comparison as shown in Table 2-1. Due to the higher signal sensitivity at 7 T, more suprathreshold voxels were counted than at 3 T. In addition, all the statistical measurements showed a clear improvement at the higher field strength.

2.2.3. X-nuclei imaging

Theoretically, any unpaired protons, such as ^{23}Na, ^{31}P, ^{13}C can be employed for imaging. However, the inherent low concentration (i.e. ^{23}Na concentration is 22,000 times smaller than ^{1}H) of those nuclei in the human body prevent their clinical applications at low fields. With increased sensitivity from higher field strengths, specific imaging applications on X-nuclei become possible. In addition, the much longer RF wavelength and lower resonance frequency of X-nuclei MRI exempts it from engineering challenges that proton imagining has, such as the inhomogeneous image intensity and tissue overheating.

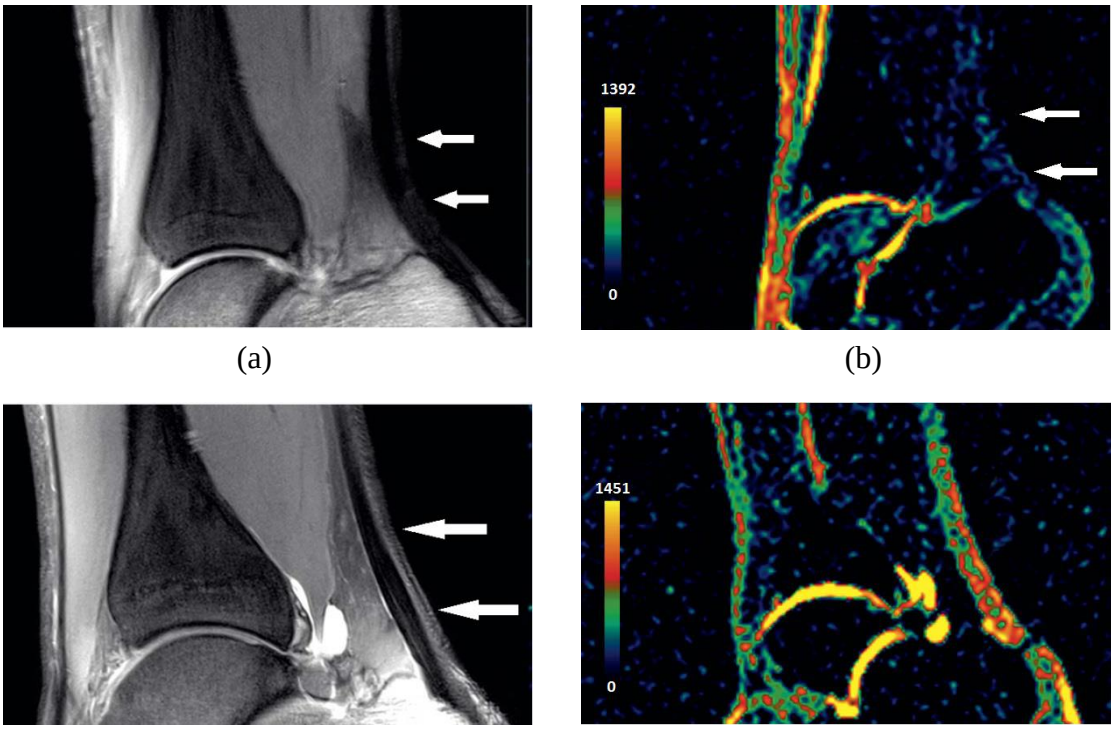

(a) (b)

(c) (d)

Figure 2-9. A morphological proton image (a) and a colour-coded sodium image (b) were acquired from a 27-year-old healthy volunteer at 7 T. A morphological proton image (c) and a colour-coded sodium image (d) were acquired from a 46-year-old patient with Achilles tendinopathy. Morphological images were acquired with proton-density-weighted turbo-spin-echo (PDW-TSE) and the corresponding sodium images were acquired with gradient echo sodium sequence [7]. (Reproduced with permission).

Comparing the proton images in Figure 2-9 (c) to those in Figure 2-9 (a), only a locally increased intensity is seen, which could be a result of various causes and thus is insufficient for clinical diagnosis of Achilles tendinopathy. On the contrary, significant increased sodium signals were found in the Achilles tendon of the patient with Achilles tendinopathy (1451 compared to 1392 in healthy people), which correspond to a higher glycosaminoglycan (GAG) content in the Achilles tendon that could be used for diagnosis of Achilles tendinopathy [5, 69]. The ultra-high field sodium MRI offers the opportunity of detecting the cartilage degeneration or injury at an early stage before morphological changes are seen by proton MRI.

2.3. Conclusion

In this chapter, the benefits of higher B_0 are illustrated with mathematical derivations and clinical examples. As shown, the increase of the intrinsic SNR with stronger B_0 provides better image quality with less noise for anatomical images, which can facilitate clinical diagnoses with less interference. The enhanced sensitivity of ultra-high field MRI enables new and earlier insights

of brain pathologies that are not available at lower fields. In addition, the benefits of ultra-high fields are also reported with increased various functional measurements. Ultra-high field MRI also finds its applications in X-nuclei imaging with significantly higher sensitivity for certain applications. However, before successfully reaping these benefits, several technical challenges related to RF engineering, namely, the inhomogeneous RF transmit field, the excessive heating and the long scan time, need to be overcome. These issues and the existing solutions will be reviewed in the next chapter.

Chapter 3. Technical Challenges and solutions of ultra-high field MRI

As demonstrated in Chapter 2, ultra-high field MRI brings improved SNR and BOLD effect that can facilitate clinical diagnoses and neuroimaging research. In addition, the X-nuclei imaging also finds its applications in ultra-high field MRI, which introduces new protocols for diagnosing certain diseases. However, the RF field related issues hamper these benefits. These issues occur during the RF transmission and reception. Specifically, the inhomogeneous transmit field can generate images with bright and dark spots that affect diagnostic accuracy. In addition, more RF power is deposited into the human body during transmission, which may cause irreversible tissue damage. During reception, the typical sequential acquisitions of the MRI protocols require a long duration scan; any motion occurring during this period can contaminate the received RF signal and cause motion artefacts, thus degrading the clinical value of the images. The primary aim of this project is to develop novel RF techniques for solving these RF-related issues. However, before reviewing the existing solutions for these issues, numerical models and clinical images are employed to present these RF related issues; thus demonstrating the importance of solving these issues. After analysing the advantages and disadvantages of existing solutions, the novel RF technique that combines an array structure with a rotating coil concept is investigated. In Chapters 4, 5 and 6, such a technique and corresponding algorithms are developed which make up the primary work of this thesis.

3.1. Inhomogeneous magnetic field

3.1.1. Interference of electromagnetic waves

Interference is a physical phenomenon existing in all types of waves that describes the interaction of waves. The interference of waves can form a resultant wave pattern with greater and lower amplitude. In MRI, the transmit and receive MR signals are presented as transmit and receive electromagnetic waves. As one form of waves, the electromagnetic waves exhibit the wave behaviour which may cause interference dependent on the coil-subject configuration and frequency. The wavelength λ in the dielectric is calculated as:

$$\lambda = \frac{c}{v\sqrt{\varepsilon_r}} \tag{3.1}$$

where c is the speed of the light in free space, v is the frequency of the electromagnetic wave and ε_r denotes the relative permittivity of the dielectric subject. Since the relative permittivity is highly dependent on the frequency and tissue type, the wavelength of the RF field is different at various

field strengths and in different tissues. The Table 3-1 lists relative permittivity and conductivity values for several brain tissues at different field strengths.

Table 3-1 Values of the relative permittivity and conductivity at 1.5 T and 3 T [70]

	Relative permittivity		Conductivity (S/m)	
	1.5 T	3 T	1.5 T	3 T
Cerebrospinal Fluid (CSF)	97.13	84.04	2.07	2.14
Gray matter	97.43	73.52	0.51	0.59
White matter	67.84	52.53	0.29	0.34

As shown in the Table 3-1, the relative permittivity decreases at higher field strength; however, the frequency increases faster than the change of relative permittivity. Therefore, according to Eq. 3.1, the wavelength decreases at a higher field. The wavelength of RF field in the air at 1.5 T and 3 T is about 468 cm and 234 cm [71, 72]. Since the relative permittivity of human tissues vary from 10~100, the wavelength of the RF waves reduce by a ratio of 3~10 in the human body. Given the fact that a large portion of human tissues is water, which has a relative permittivity of 78, the wavelength in human tissue is about 53 cm and 27 cm at 1.5 T and 3 T. Both of these wavelengths are longer than the dimensions of the human head and will not form interference inside the human head. However, the latter is smaller than the size of the torso and thus the interference is seen in the 3 T torso images as darkened and brightened regions [73]. The wavelength of the RF field in the air decreases to 100 cm at 7 T; correspondingly, the wavelength decreases to 11 cm in human tissue. This wavelength is only a fraction of the dimension of the human head, and thus constructive and destructive interference can form inside the human head, exhibiting darkened and brightened artefacts that degrade the image quality.

3.1.2. Transmit RF magnetic field (B_1^+) and receive RF magnetic field (B_1^-)

In ultra-high field MRI, the transmit and receive RF fields are significantly different and both of them can influence the acquired image; therefore, it is important to investigate their influences on the image homogeneity. The RF magnetic field in MRI is normally referred as the B_1 field to distinguish it from the B_0 field. During excitation, the transmit RF field perturbs the net magnetisation away from the parallel or anti-parallel B_0 direction. After removing the RF wave in the consequent reception, the flipped magnetisation realigns to the initial direction and induces a detectable RF field that is received by RF coils. The transmit profile B_1^+ denotes the regions and the strength of the flipped magnetisation, which is proportional to flip angle, and the receive profile B_1^-

depicts the capability of receiving signal for a coil. The mathematical calculation for B_1^+ and B_1^- are shown in Eq. 2.30. A numerical model built in the commercial software FEKO (EMSS, SA) is used to illustrate the changes of B_1^+ and B_1^- associated with the field strengths.

In Figure 3-1, the length of the coil was 200 mm (longitudinal) and the width was 80 mm (transversal). Eight capacitors and one voltage source (1V) were inserted into copper patches with 5 mm width. A phantom with human head size (ϕ = 200 mm) was placed 25 mm away from the coil. The dielectric constants of the phantom were set differently to simulate distilled water, physiological saline water and white matter at different resonance frequencies. Those parameters were set as ε_r =78, σ = 0.03 S/m for distilled water, ε_r = 78, σ = 1.67 S/m for physiological saline water [74] and ε_r =67.8, σ = 0.292 S/m, ε_r = 52.5, σ = 0.342 S/m, ε_r =43.8, σ = 0.413 S/m for white matter at 64MHz (1.5 T), 128MHz (3 T) and 298MHz (7 T) [75].

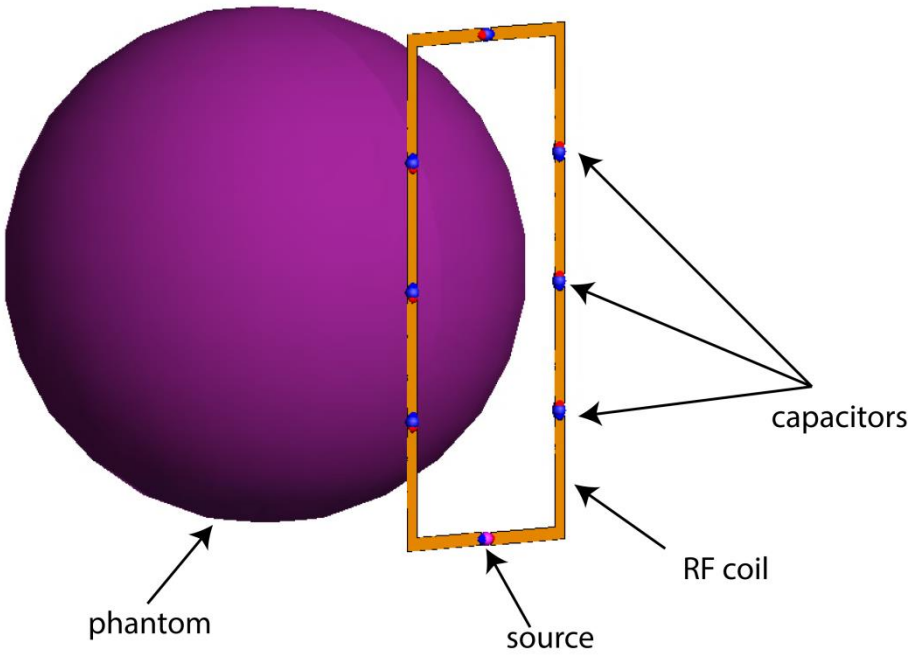

Figure 3-1. Numerical model of RF coil and dielectric phantom

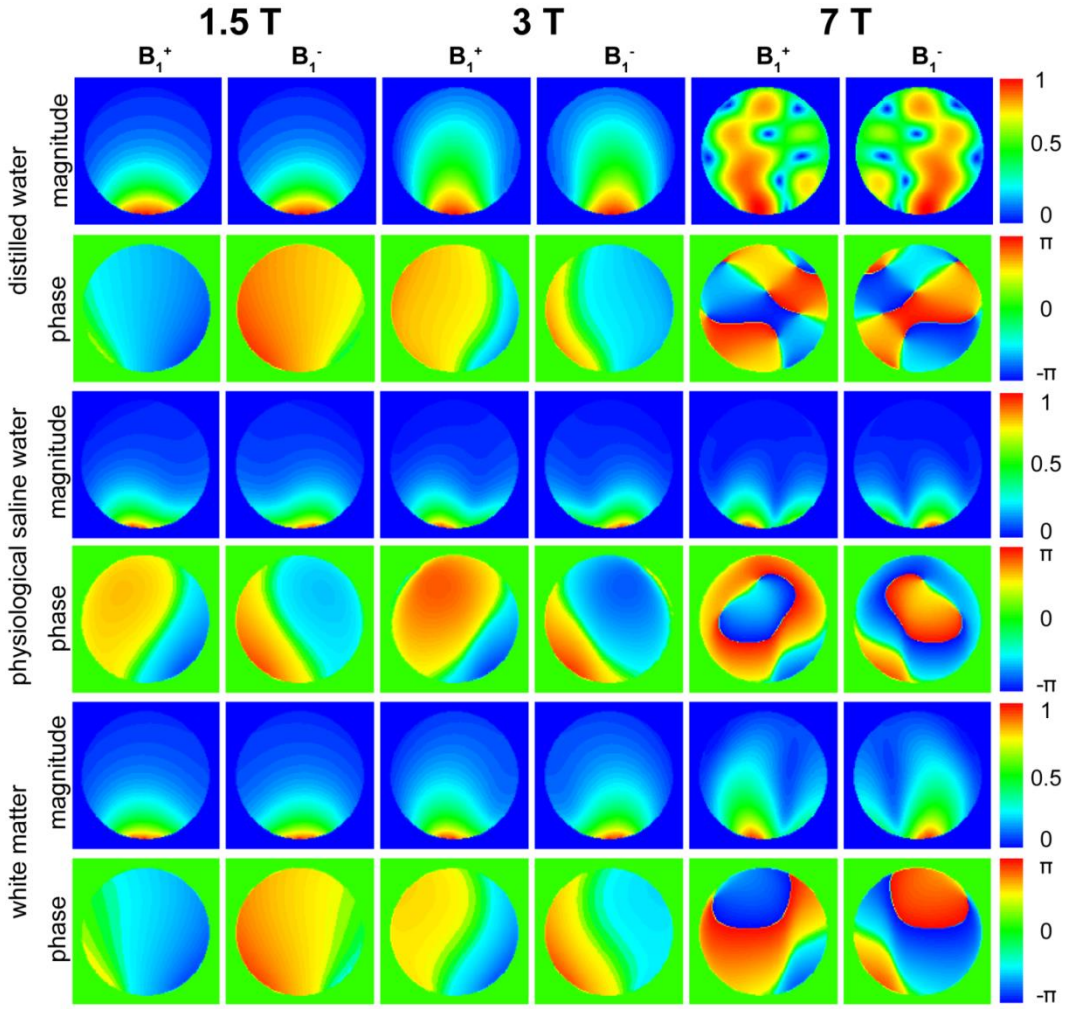

Figure 3-2. The simulated B_1^+ and B_1^- of the distilled water phantom, saline water phantom and white matter phantom. All plots are normalised.

The relative permittivity of the distilled water and saline water are the same, that is, they have the same wavelength according to Eq. 3.1. However, two dielectric media have very different conductivity constants. The former one is a nearly lossless dielectric, whereas the latter one is a heavily lossy dielectric. The impacts of this difference on B_1^+ and B_1^- are shown in the first and third row of Figure 3-2. With the very high conductivity of the saline water, the magnetic field loses its power rapidly as it propagates in the phantom. The B_1^+ and B_1^- can only penetrate a short distance, resulting in a shallower B_1 penetration. In contrast, since magnetic fields are not heavily dampened in the distilled water phantom, with the increases in the B_0 from 1.5 T to 7 T, the interference starts to emerge with darkened and brightened spots in the distilled water phantom. Comparing phase maps from 1.5 T to 7 T, we can see that more phase variations existed at higher field strengths. Since the dielectric property of the white matter is closer to the average value for human brain tissue, the B_1^+ and B_1^- profiles in the fifth and six rows can better demonstrate the

magnetic field distribution inside of the human brain. Both the transmit and receive profiles start to become asymmetric to the central axis at 7 T, and this distribution can cause destructive and constructive interference while using a volume transceive coil array.

3.1.3. Inhomogeneity B_1 and SI image

The inhomogeneous B_1^+ field and B_1^- field of the single coil at different field strengths are shown in Figure 3-2. However, when using a coil array to transmit and receive signals at ultra-high fields, the transmit magnetic fields generated by every coil will superpose and form constructive and destructive interference, a phenomenon commonly referred to as "B_1 inhomogeneity". Consequently, the images will have brightened and darkened regions. By ignoring the susceptibility effect, a gradient-echo (GRE) image can be calculated as [53, 76, 77]:

$$SI = W \sin(V\tau\gamma \left| B_1^+ \right|) \left| (B_1^-)^* \right| \tag{3.2}$$

where W is the weighting factor and the asterisk * denotes the complex conjugate operation. V and τ is the magnitude of the excitation voltage and the duration of the RF pulse. γ is the gyromagnetic ratio. This equation enables the presentation of the simulated SI images by using numerically calculated B_1^+ and B_1^- fields.

In Figure 3-3, an 8-element coil array loaded with a spherical phantom is built using FEKO. The magnetic fields obtained from this model are used to demonstrate the B_1 inhomogeneity and the corresponding inhomogeneous SI images. The size of the coils and the size and the dielectric constant of the phantom have the same values as those in Figure 3-2.

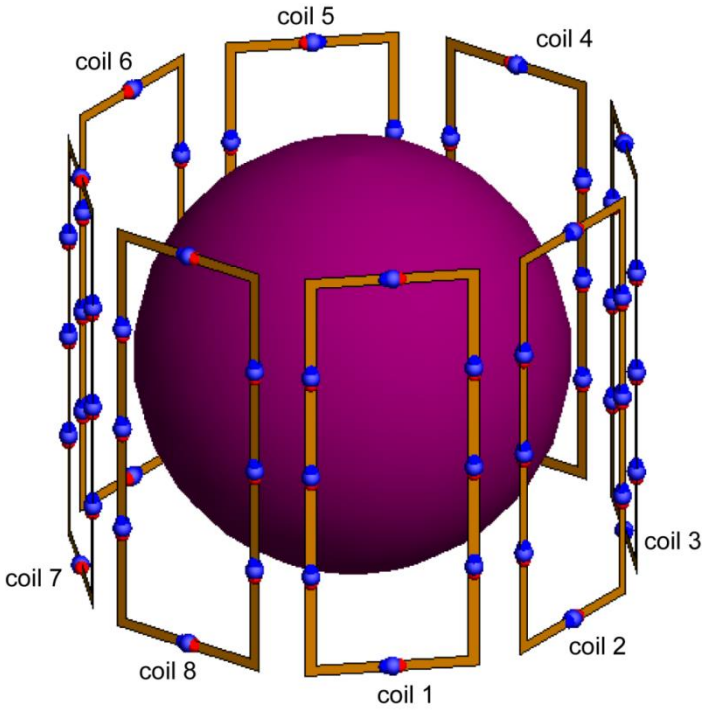

Figure 3-3. Numerical model of the RF coil array and the dielectric phantom

As shown in Figure 3-4, none of three dielectrics exhibit an inhomogeneous B_1^+ or inhomogeneous *SI* at 1.5 T. However, when the field strength increases to 3 T, the lossless property of the distilled water results in deep B_1 penetration that forms constructive interference, which exhibits as the brightened centre of the phantom. On the contrary, the centre of the *SI* image obtained with the saline water phantom is dark because the coil can barely transmit or receive signals from the centre due to the high conductivity dampening effect. This correlates with the B_1^+ and B_1^- maps of the saline water phantom in the Figure 3-2. Since the dampening effect becomes stronger with higher fields, the centre of the saline water *SI* image at 3 T is darker than at 1.5 T. With a very low conductivity constant ($\sigma = 0.03$), the magnetic fields in the distilled water are not dampened much and therefore have the strongest interferences, showing the most obvious inhomogeneous B_1^+ and *SI* image at 7 T. We can see the brightened centre and a darkened circular ring adjacent to the centre. In the *SI* image of the white matter phantom at 7 T, apart from the brightened centre, the areas near the coil are also brightened with higher local receive sensitivity. The inhomogeneous pattern in the white matter phantom is similar to the pattern in a human head, which has to be mitigated for better diagnostic accuracy.

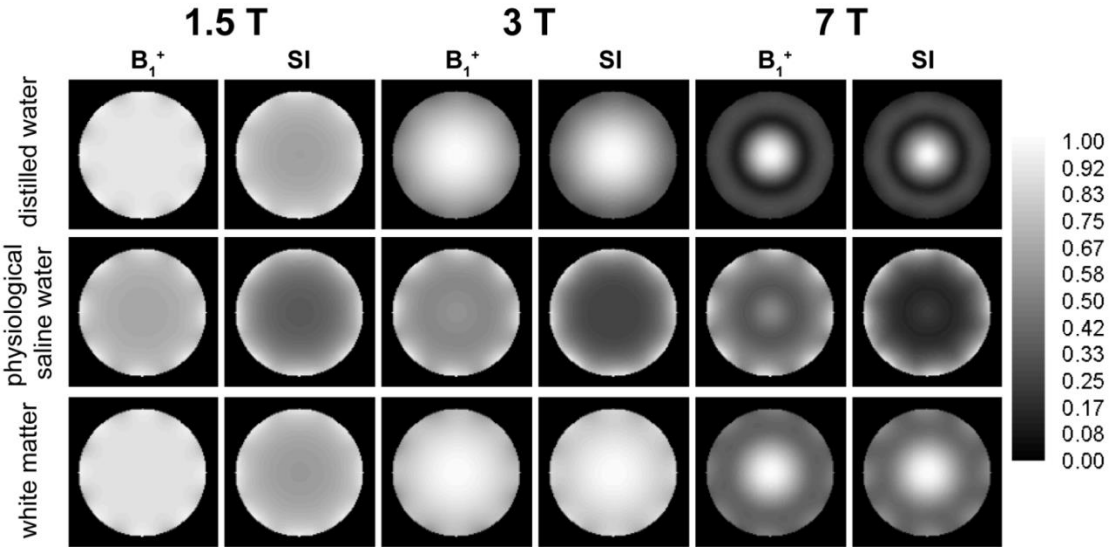

Figure 3-4. The B_1^+ and *SI* images of the distilled water phantom, saline water phantom and white matter phantom at different field strengths. The constructive and destructive interferences are clearly seen at 7 T *SI* images. All plots are normalised.

3.2. Specific absorption rate (SAR)

The excessive heating is considered to be the most intractable and primary issue that prevents clinical use of the ultra-high field MRI. It is caused by the over-dosed RF energy dissipation into human bodies. Since the rise in temperature inside human bodies is unable to be measured directly, the specific absorption rate (SAR) is used to measure the rate at which the RF energy is absorbed by the human bodies. It is calculated as:

$$SAR = \int_{sample} \frac{\sigma(r)|E(r)|^2}{\rho(r)} dr \tag{3.3}$$

where E denotes the electric field inside of the subject, and $\sigma(r)$ and $\rho(r)$ are conductivity and density at the r voxel location. From Eq. 3.3, we know that $SAR \propto |E|^2 \propto \omega_0^2$, and $\omega_0 \propto B_0$; therefore, SAR is linearly proportional to B_0^2 up to 250 MHz [8]. The SAR has a quadruple increase when the field increase from 1.5 T to 3 T. In a worst scenario, the SAR at 7 T has a 21.8-fold increase compared to at 3 T. Several studies have drawn different conclusions in regard to the SAR dependency on B_0 above 250 MHz. By using FDTD simulations, Collins et al. [78] suggested that the SAR increase at ultra-high fields would not be as linearly as low field. They also indicated that the slope of the SAR increase with the frequency would drop at ultra-high fields. The experiments carried by Vaughan et al. [79] indicated the SAR at 7 T had a two-fold increase compared to that of at 4 T.

Besides the B_0, the SAR is also dependent on the sequence parameters of a protocol, such as pulse duration, flip angle and repetition time. In order to compare the SAR at different frequencies with the same parameters, we assume the flip angle is excited to 90 ° with a 3 ms rectangular RF pulse (magnitude of B_1^+ is $1.957\mu T$) [80]. According to Eq. 2.7, $V = \frac{\alpha}{\tau\gamma\left|B_1^+\right|}$, and since SAR increases with the square of the driving voltage at any given condition [8], the SAR induced at a flip angle α for pulse duration τ is calculated as [78]:

$$SAR_{\tau/\alpha} = f(\frac{3ms}{\tau})^2(\frac{\alpha}{90^o})^2 SAR_{3ms/90^o} \tag{3.4}$$

where *f* is a scaling factor determined by the pulse type [81]. *f* = 1 for a rectangular pulse. For a given pulse sequence, the SAR is calculated as the sum of the energy absorbed in a repetition time (TR) divided by the TR [78]:

$$SAR = \frac{\sum_{n=1}^{N}(SAR_{\tau_n/\alpha_n}\ \tau_n)}{TR} \tag{3.5}$$

where τ_n and α_n denote the flip angle and pulse duration of the n-th pulse in a pulse train. It is reported that the average SAR increases to 6.130 W/kg at 8 T, about 45 times higher than 0.1349 W/kg at 1.5 T [78]. 1W/kg of SAR would increase the temperature of an insulated slab about one degree Celsius [82]. The International Electrotechnical Commission (IEC) and the US Food and Drug Administration have strict limits for both whole body heating and localised heating. The head and torso SAR limits are 3.2 W/kg for the whole head and 10 W/kg over any 10 grams of tissue in any 6-minute period. The whole body SAR is limited to 4 W/kg over any 15-minute period [83]. The SAR increases dramatically at ultra-high fields and imposes potential damage to tissues. In order to obtain an image with the same flip angle under the safety limit, the scan time may be extended with a longer TR to achieve a low SAR.

While the global SAR can be monitored and maintained under the safety limit, the patient-specific local SAR cannot easily be measured or monitored *in vivo*; therefore, predicting the local SAR via numerical models is important. The Finite Element Method and the Finite-Difference Time-Domain (FDTD) [84] methods are normally employed to calculate the SAR distribution. Studies that adopted the FDTD algorithm reported that the local SAR distributions are patient-, coil- and position-dependent [15, 85]. Demonstrated with the virtual family [86], these studies predicated

that the global and local SAR values and distributions were closely related to the coil structure and patient-coil positions.

3.3. Long scan time

The first live human MRI scan on 3rd June, 1977 took about 5 hours from the experiment started [87]. Nowadays, a MRI scan normally takes from 20 minutes to over 2 hours depending on the purpose [88]. A long scan time could cause discomfort to the patient, both physically and psychologically, and consequent movements will lead to motion artefacts in the images, degrading their clinical value. In a study of subjective acceptance of 7 T MRI, Theysohn et al. [9], reported that the long scan duration was the most disturbing factor that caused patient discomfort. The noise, low temperature and positioning/padding were also reported as secondary reasons for discomfort. With longer scan time, discomfort caused by these factors could become even worse and inevitability generate poor quality images. I have personally witnessed several scans that had to be ceased due to patient discomfort, which was attributed to the long scan time and the associated low temperature. As shown in Figure 3-5 (a), the brain image has obvious motion artefacts (marked with red arrows), which were induced during a part of the scan [89], that can seriously affect the diagnosis. The shoulder image in Figure 3-5 (b) is ambiguous due to the motion artefacts [90], and therefore has less clinical value. For brain functional investigations, the low temporal resolution prevents the acquisition of the fast brain reactions that carry important information. Therefore, it is important to shorten the MRI scan time.

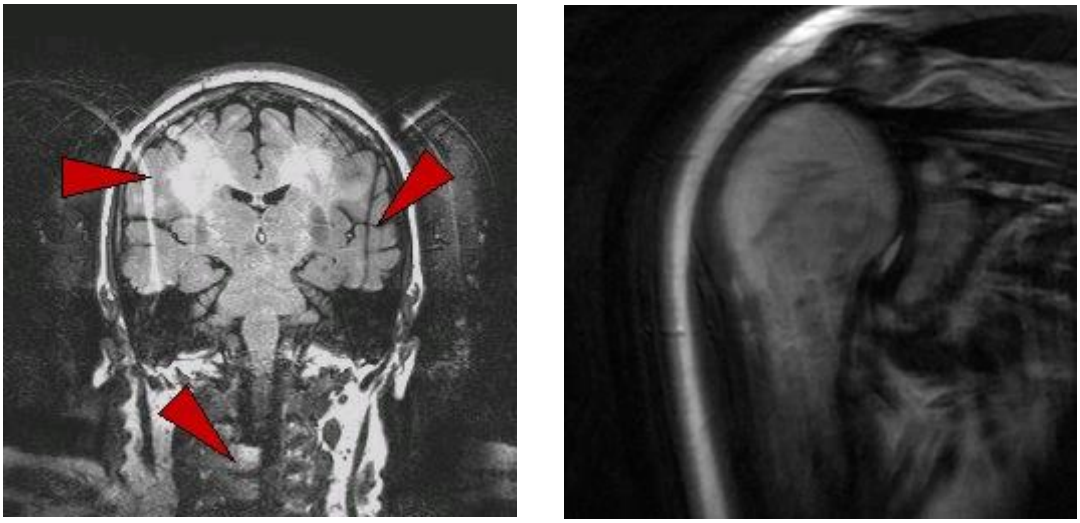

(a) (b)

Figure 3-5. (a) A human brain image with serious motion artefacts. Red arrowheads marked the aliasing artefacts that can seriously affect diagnosis. (b) A shoulder image contaminated with motion artefacts.

3.4. Solutions to high field issues

3.4.1. B_1 inhomogeneity mitigation

Different shimming strategies have been developed to improve the B_1 homogeneity, from hardware through to algorithms. They range from static shimming strategies that homogenise B_1 distribution, to those dynamic strategies that homogenise the flip angle with a Bloch equation.

3.4.1.1. Hardware design solution

The centre of the human brain is often brightened when the RF coil array is excited in circular polarised (CP) mode at 7 T. In addition, the left and right regions adjacent to the centre have about 50% lower intensity [78, 79]. For this specific application at 7 T, the B_1 homogeneity can be simply solved by the RF coil design. Since placing coupled surface coils on the sample can alter the transmit B_1 field excited by a volume coil, using a surface coil array passively or actively coupled to a transmit volume coil array could mitigate the B_1 homogeneity for human brain imaging. As demonstrated in [91] with numerical models, the B_1 homogeneity was improved one third by an 8-element passive coupled coil array. The follow up study with an 8-element actively tuned coupled coil array demonstrated the capability of improving B_1 homogeneity by 23%. However, the off-resonant coupled coils were manually adjusted and lack of freedom to realise a volume B_1 shimming. In order to fully exploit this method, a rapid B_1 field mapping strategy and a dynamic element tuning strategy should be developed.

3.4.1.2. Dielectric shimming

Another relatively simple way of homogenising B_1 distribution is to use high permittivity dielectric pads, in which the strong displacement current is induced to modify the B_1 distribution inside the subject. In their early study, Yang et al. [92] used both experimental and simulation results to demonstrate the possibility of using a water pad to improve the B_1 homogeneity. Later publications that used dielectric pads for abdomen imaging achieved improved image homogeneity at 3 T [93-96]. These dielectric pads were normally made with water or ultrasound gel mixed with dissolved paramagnetic material; therefore, the permittivity values of those pads were not very high, which limited the ability to mitigate B_1 inhomogeneity. In addition, a 3.2 kg dielectric pad of 30 mm thickness prevented the use of two pads, above and below the subject. In the last several years, both the weight and thickness of the dielectric pads have been dramatically reduced by using very high permittivity material [22, 35, 37]. The saturated suspension, made with barium titanate and water, has a very high permittivity ($\varepsilon_r \approx 300$), which enhances the B_1 modification and the SAR control ability by manipulating displacement current. More importantly, the thickness can be reduced to 10 mm and the weight to about 2 kg. These advancements make it possible to use multiple small pads for both local and global B_1 shimming. There is currently no standard model of this shimming strategy. It is hoped that an optimisation algorithm can take both the geometry and the dielectric property of the pads into consideration, to maximise the performance of dielectric shimming.

3.4.1.3. Parallel transmission

To date, parallel transmission is considered to be the most effective shimming strategy. The philosophy behind this method is to modulate the transmit profile with/without pulse design to realise a homogeneous transmit profile.

3.4.1.3.1. Parallel transmission without pulse design (RF shimming)

As a special case of parallel transmission, the RF shimming only employs the transmit profiles to modulate the magnitude and phase of each transmit channel. Therefore, constructive and destructive interference is avoided and eventually a homogeneous image is achieved. The shimmed transmit profile B_{1-shim}^{+} is calculated as:

$$B_{1-shim}^{+} = \sum_{n=1}^{N} w_n (B_1^{+})_n e^{j\varphi_n} \tag{3.6}$$

where N is the number of individual channels, and w_n and φ_n are the weighting factors of the *n-th* channel to modulate the magnitude and phase of the transmit B_1^{+}.

As illustrated above, the B_1 distribution in the human brain has a certain pattern if the coil array is excited in CP mode, which enables the manual adjustment of the magnitude and phase of each channel to obtain a homogeneous B_1^+. In [32, 33], the homogeneous head and torso images were obtained by manually adjusting the driving current of each channel. However, for better shimming of the inhomogeneous B_1^+, the transmit profiles can be measured and used in an optimisation algorithm to determine the magnitude and phase of each channel. Ibrahim et al. [21] employed a FDTD model and optimisation algorithm to explore the effect of homogenising B_1^+ with a 24-strut TEM resonator at 8 T. The magnitude and phase of each driving point was achieved by minimising the B_1^+ standard deviation referenced to that of CP mode. It is reported that the standard deviation of B_1^+ had a 2.5-fold improvement using the described method. A similar method was also employed to improve whole body and localised B_1^+ homogeneity at 7 T [31]. However, Mao et al. [36] indicated the incapability of this method for B_1 shimming by using FDTD simulations. In his study, he used a human head model with 23 tissue types and two sets of coil arrays were built, namely a 16-element coil array (element size: 150 mm × 20 mm) and an 80-element coil array (element size: 25 mm × 20 mm). The 16-element coil array was capable of shimming B_1 of a whole brain at 300 MHz (7 T) or a single slice of human brain at 600 MHz (14 T). However, it is incapable of shimming the whole brain at 600 MHz. A larger number of elements or a smaller region of interest (ROI) is beneficial to the B_1 shimming. With more elements, the 80-element coil array was capable of shimming B_1 for a whole brain up to 600 MHz. However, this will dramatically increase the hardware expense for elements and individual amplifiers to modulate the magnitude and phase. In addition, the B_1 mappings [97-99] for a large number of coils are time consuming.

3.4.1.3.2. Parallel transmission with pulse design

Besides modulating the magnitude and phase of each channel, the RF pulse modulation can be employed in the time or spatial domain to avoid using a large number of RF coils. Collins et al. [100] combined the transmit profiles and a sequence of RF pulses to homogenise the B_1^+ and remarkable improvement in B_1^+ homogeneity for a whole brain was reported with a 16-element coil array at 600 MHz. This method was considered as an intermediate strategy between RF shimming and more elaborated spatially selective RF pulsing techniques [23, 24]. The aim of the parallel transmission is to obtain a homogeneous transmit profile with simultaneously excited RF coils, where the RF pulse can be individually modulated in conjunction with the transmit profiles. This process will be briefly introduced and more explicit mathematical explanations can be found in [23, 24]. As mentioned, the homogenous transmit profile can be obtained as P_i [101]:

$$P_{desire}(r) = \sum_{n=1}^{N} S_i(r) P_i(r) \tag{3.7}$$

where the desired transmit pattern P_{desire} at voxel r is obtained as a linear superposition of individual RF pulses pattern P_i , which are weighted by the complex transmit sensitivity profiles S_i. Various B_1 mapping sequences and techniques [97-99] have been developed to acquire the transmit sensitivity (B_1^+) of each coil. However, Eq. 3.8 is in the image domain; therefore, to derive the individual RF pulse waveform, Eq. 3.8 must be transformed into the frequency domain. Thus P_{desire} is calculated as:

$$P_{desire}(k) = \sum_{n=1}^{N} S_i(k) \otimes P_i(k) \tag{3.8}$$

where k is the corresponding k-space coordinates and $\otimes$ denotes the convolution. In order to solve the individual $P_i(k)$, a matrix inversion must be performed. To facilitate this nontrivial task, the sensitivity profiles $S_i(k)$ are grouped into a single invertible matrix S_{full}, and the all $P_i(k)$ are formed into a vector P_{full} [23]. Therefore, Eq. 3.7 is modified as:

$$P_{desire}(k) = S_{full}(k) P_{full}(k) \tag{3.9}$$

and P_{full} is calculated as:

$$P_{full}(k) = (S_{full}(k)^H S_{full}(k))^{-1} S_{full}(k)^H P_{full}(k) \tag{3.10}$$

where individual $P_i(k)$ can be extracted from $P_{full}(k)$.

Once the $P_i(k)$ is solved, the actual B_1 waveform in time domain is determined as:

$$B_{1i}(t) = W(t) P_i(k(t)) \tag{3.11}$$

where the $W(t)$ is the weighting function that corresponds to the k-space sampling trajectory.

3.4.2. SAR control

While the B_1 is well shimmed for homogeneous imaging, the SAR is more critical for a safe scan. The global SAR can be monitored and controlled [17-20, 29], whereas the local SAR is impossible to be measured in real time. As demonstrated above, the local SAR is coil-, position- and patient-dependent; therefore, the distribution and value of the local SAR may vary dramatically across different cases. Based on the work done by Collins et al. [16], a safety scaling of 60 was

considered to be enough to ensure the local SAR remained under the limit in a worst case scenario. However, Greef et al. [34] claimed a safety factor of 1.4 was sufficient, a conclusion was derived from local SAR calculations on six numerical models using the FDTD algorithm. The variation in the safety factors could have resulted from different coil arrays used for scans, different coil-patient positioning and different sequences. While the generic factor for RF power scaling is not determined, it is certain that this scaling will inevitably limit the efficiency of the RF system, thereby compromising the benefits of using ultra-high field MRI, such as extended scan time of up to 67% [17] and low flip angles with poor SNR. Therefore, it is meaningful to accurately predict and estimate the local SAR distributions and values. By employing the low-resolution pre-scan, numerical modelling and calculations, registration techniques, the method proposed by Jin et al. [15] has reported to dramatically improve the accuracy of the prediction of SAR values. Alternatively, a group of methods called electric property tomography (EPT) [14, 28, 30, 34, 102] were developed in the last decade. This type of approach estimates the dielectric property of the subjects from the acquired B_1 maps. Currently, this approach is still under development since it relies heavily on the B_1 mappings, which normally have singular values at noises at ultra-high fields. It is hoped the EPT method can benefit *in vivo* SAR estimation once the dielectric property can be mapped precisely.

3.4.3. Scan time reduction

MRI scans take a long time because they acquire data in a sequential fashion, realised by the switching magnetic gradient field firstly described by Lauterbur [103]. As illustrated above, the scan time may be extended further than it should be in order to maintain SAR values under the safety limits at ultra-high fields. The scan duration depends on the switching rate and the strength of the gradient coils. Scans with a higher slew rate normally require less time to perform. Hardware developments have dramatically improved the performance of the gradient coils and enable fast imaging protocols, such as the echo planer imaging sequence [104], the fast spin echo sequence [105], and the fast gradient echo imaging [106]. However, these expensive hardware improvements are reaching limitations. As the gradient field strength and the switching frequency increase, the electrophysiological reactions become stronger, which could cause peripheral nerve stimulation [107, 108] and cardiac stimulation [109, 110].

Meanwhile, parallel imaging with partial *k*-space data has been intensively studied and developed in the last decade. Different from the full *k*-space fast imaging sequence mentioned above, parallel imaging acquires only partial *k*-space data and uses different algorithms to reconstruct the image. Simultaneous Acquisition of Spatial Harmonics (SMASH) [13] employs the sensitivity variations of a coil array to partially replace the gradient encoding. SENSitivity Encoding (SENSE) [11, 12] exploits the spatial sensitivity weightings of the coils to reconstruct images with

partially acquired k-space data. Generalized Autocalibrating Partially Parallel Acquisition (GRAPPA) [10] uses the acquired *k*-space data to find the coefficients from coils and reconstruct the missing (not collected) *k*-space data. More recently, compressed sensing (CS) [111, 112] has attracted interest as it exploits the sparsity of the MRI data and acquires less data than the above mentioned algorithms. The researchers have shown the promising possibilities of combining parallel imaging and compressed sensing for greater scan time reduction [113, 114]. However, the compressed sensing is still under the development due to its randomised sampling pattern and long-time non-linear reconstruction, whereas the parallel imaging has been successfully integrated on the host computer of the MRI system.

All parallel imaging methods share the same philosophy, which employs spatial encoding provided by RF coils to partially replace the time-consuming gradient encoding. Theoretically, increasing the number of RF coils in the phased array can achieve higher acceleration factors and further reduce the scan time [11, 38, 39, 115-120]. However, this method has certain practical limitations for both head and cardiac imaging. It is necessary to reduce the coil size while increasing the number of coils for the same application. Although the acquisition acceleration is improved with more elements, the B_1 penetration is reduced and the mutual coupling is increased, which can undermine the coil performance. As reported by Schimitt et al. in [116], due to the coupling and eddy current losses, the SNR of a coil in the 128-channel array is only 43% that of a single coil of the same size. The side effects of smaller and denser coil array limit improving SNR by means of increasing the number of coils, especially for the central SNR. Wiggins et al. [39] reported that the 50 mm diameter coil in a 96-element coil array was on the edge of sample noise dominance at 3 T, even with a close-fitting helmet and optimised coil design. Compared to a 32-element coil array [38] built on the same helmet, the unoptimised (root-sum-of-square) central SNR of the 96-element array was even 20% lower than that of the 32-element coil array. After optimisation of the SNR combination [38], the central SNR was still 5% lower than the 32-element coil array. This highlights the importance of maintaining a large coil size to achieve a better B_1 penetration and sample noise dominance for better SNR, especially those signals in the centre. Similarly, a 128-channel array with small coils (64 mm×64 mm) improved central SNR by only 3% compared to array with a quarter of coils (32 channels). In contrast, with larger coils for a 32-channel array, the central SNR and surface SNR had a 1.4-fold and 2.5-fold SNR increase compared to an 8-element commercial coil array. In terms of imaging acceleration, the reduction factor increased from three for the 32-channel array to four for the 96-channel array. That is, only 8.3% of data can be further dropped when the number of the channels is tripled.

As illustrated in the above studies, employing a large number of receive-only coils has successfully demonstrated the superficial SNR increase, whereas the central SNR increase is subject to the coil structure. The scan time can be reduced by about 10% by tripling or quadrupling the number of coils. However, as the MRI enters the ultra-high fields, the whole body coils for uniform excitation are no longer available. Instead, a custom made multi-channel transmit/transceive coil array is necessary to provide homogeneous excitation. This will further reduce the advantages introduced by more coils since the transmit penetration will also be shallower with smaller coils. Therefore, the ability to improve the central SNR will be less than that when using lower field MRI. With a shallower B_1 penetration and stronger coupling, not only is the parallel imaging ability undermined, but also the B_1 homogeneity mitigation, by means of transmit SENSE, is impaired. In addition, the hardware expense will increase with the number of coils and those of the associated transmit and receive RF channels.

As an alternative method, the recently developed single element rotating RF coil (RRFC) [40, 41] can also be used for scan time reduction without the above-mentioned issues. With a single coil element, the coil is naturally decoupled and the size of the coil can be larger to provide a deeper B_1 penetration. Since the rotation violates the time-invariant requirement of the Fourier transform, the Time Division Multiplexed – SENSitivity Encoding (TDM-SENSE) algorithm was developed to reconstruct artefact-free images by solving simultaneous linear equations $Ax=b$, where A is the encoding matrix, b is the acquired k-space data and x *is* the unsolved image. As shown in Figure 3-6 (a), the coil element rotates about the subject, transmitting and receiving signals at different time t_0, t_1, t_2… The extra degree of freedom provided by the rotation enables the RRFC to emulate a large number of sensitivity profiles without increasing the number of coils. Comparing Figure 3-6 (a) with (b), it is clear that a large number of sensitivity maps introduced more variations in the encoding matrix, thereby improving the condition of the encoding matrix. This property could be used for acquisition acceleration with the RRFC. Theoretically, the undersampled k-space was able to be compensated by increasing the digital signal sampling rate and the rotation speed. However, in practice, this method is restricted by the limitations of the rotation speed, the sampling rate and the rank of the encoding matrix with the compensated data. Validated with the human head imaging, the single element RRFC was able to achieve a two-fold scan time reduction with a single element.

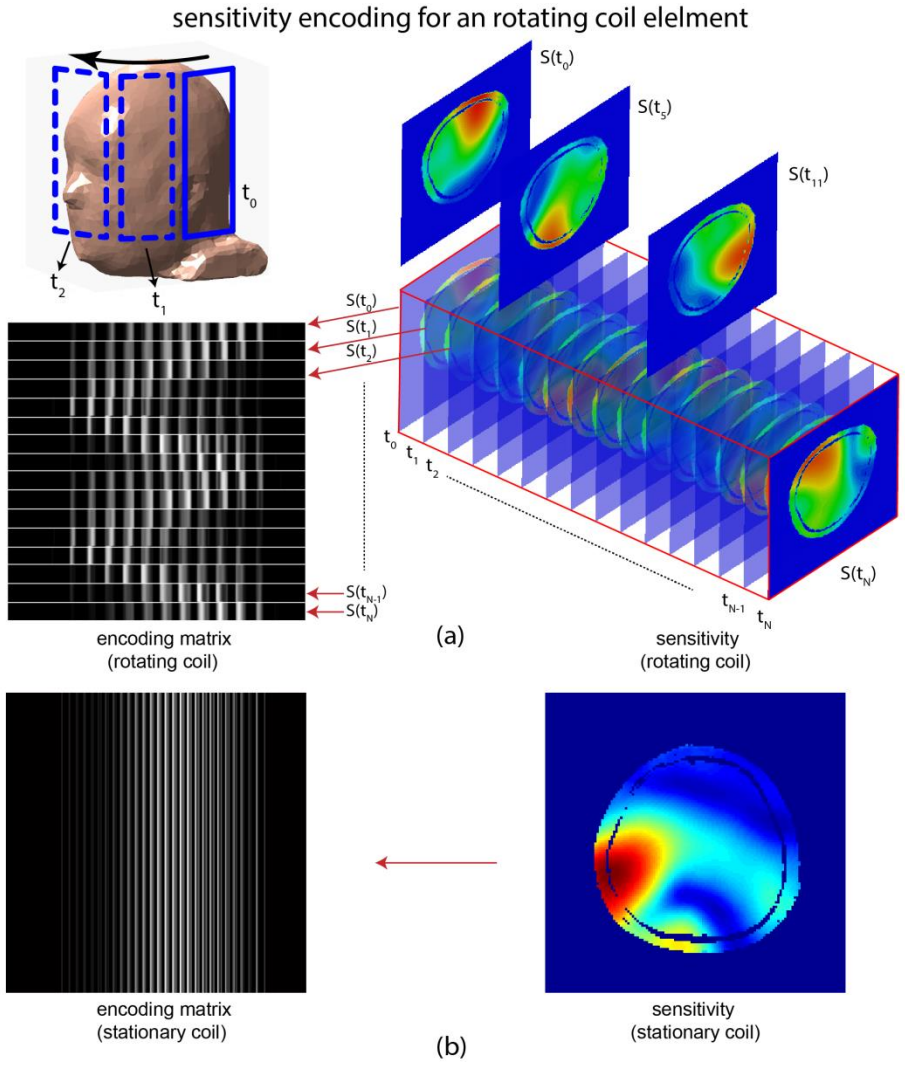

Figure 3-6. (a) The single element rotating coil and its time-varying sensitivity encoding. (b) A sensitivity of a static coil and its encoding matrix.

3.5. Discussion and conclusion

In this chapter, we have introduced the technical challenges of ultra-high field MRI and the corresponding existing solutions. The inhomogeneous B_1 biases the image and affects the clinical diagnoses. The excessive energy (high SAR) deposited in human body and the consequent heating may cause potential tissue damage. In order to maintain the RF energy level, the scan time may be extended with a lower flip angle. But a lengthy scan time can cause inevitable motion that will violate the time-invariant requirement of Fourier transform and result in artefacts which seriously degrade the image quality.

To overcome these high field problems from a hardware point of view, phased array coils with multiple elements and their individual channels are widely adopted with appropriate algorithms to cope with those issues. As the most promising method to mitigate B_1 inhomogeneity, RF shimming and parallel transmission with spatial-selective pulse require multiple coils and individual transmit

channels to modulate the transmit profiles or RF pulses. The dependent SAR control also prefers multiple coils that have higher degrees of freedom to maintain the SAR under the safety limits. Since the local SAR is more likely to exceed the limits before the global SAR reaches its limit [121-123], accurate estimation of the SAR distribution is critical for SAR control. Intensive studies [124-127] based on numerical models have demonstrated the successful control of local SAR with coil arrays. Recently, *in vivo* electric properties tomography (EPT) [14] has been developed to estimate the dielectric property using information from B_1 maps. This method provides opportunity of estimating an *in vivo*, real-time local SAR that is patient-, coil- and position-dependent, which may not be accurately modelled by numerical simulations. Essentially, all the parallel imaging algorithms [10-12, 128] share the common philosophy of using multiple coils and their spatial information to partially replace the time-consuming gradient encodings. The compressed sensing technique [111, 112] can also be combined with parallel imaging with multiple coils to further reduce the scan time [113, 114, 129].

Since all the techniques that solve the ultra-high field issues require the use of phased array coils, it is worth optimising the coil array design to benefit parallel transmission and parallel imaging. More coils provide higher degrees of freedom for better efficiency of B_1 shimming and SAR control. In addition, in parallel imaging, more distinct spatial sensitivity profiles can be employed to further reduce scan duration. However, placing more coils in a confined space will inevitably increase mutual coupling and decrease the size of the element. Consequently, the reduced B_1 penetration and increased coupling will undermine the performance of parallel transmission, SAR control and parallel imaging.

The newly developed single element rotating coil offers new vision in regard to solving ultra-high field issues. The rotation introduces another degree of freedom in the spatial domain to design solutions for B_1 shimming, SAR control and parallel imaging. Specifically, the rotating coil has abundant transmit/receive coil sensitivity profiles that can be used for RF shimming, parallel transmission and parallel imaging. The rotation also tends to scatter the RF local heating across a wider region instead of allowing it to accumulate in a certain region. However, with only one coil, the rotating coil has its own limitations in regard to resolving above mentioned issues. Since both methods have their advantages and limitations in ultra-high field MRI, in Chapters 4 and 5, we will strategically combine the rotating coil concept with a coil array structure to exploit their advantages in attempting to solve ultra-high field issues.

Chapter 4. A phantom based study to realise highly accelerated acquisition and mitigated B_1 inhomogeneity with a rotating RF coil array (RRFCA) at 7 T

As discussed in Chapter 3, strategically combining the rotating technique and the coil array could provide enhanced imaging acceleration and better B_1 inhomogeneity mitigation. In this chapter, the imaging acceleration ability and B_1 inhomogeneity mitigation strategy of a 4-element rotating radiofrequency coil array (RRFCA) was numerically investigated and experimentally validated at 7 T with a homogeneous phantom. This chapter is largely based on the journal article "Highly accelerated acquisition and homogeneous image reconstruction with a rotating RF coil array at 7 T – A phantom based study", accepted for publication by the *Journal of Magnetic Resonance* in November, 2013. Editing has been mainly carried out in the introduction for the best coherence with other chapters.

Publication details

Mingyan Li, Zhentao Zuo, Jin Jin, Rong Xue, Adnan Trakic, Ewald Weber, Feng Liu, Stuart Crozier, "Highly accelerated acquisition and homogeneous image reconstruction with rotating RF coil array at 7T-A phantom based study", *Journal of Magnetic Resonance,*Vol. 240, 102-112. 2014

Manuscript revision history

Submitted to *Journal of Magnetic Resonance*	15 August 2013
Interim Decision (minor revision)	20 October 2013
Revision submission	1 November 2013
Accepted	10 November 2013
Available online	14 November 2013

Author contributions

Mingyan Li	Numerical modelling, code implementation, analysis and interpretation, manuscript preparation, experiment implementation
Zhentao Zuo	Hardware design and manufacture, experiment implementation
Jin Jin	Numerical modelling, code implementation, analysis and interpretation, manuscript reviews
Rong Xue	Hardware design and manufacture, experiment implementation
Adnan Trakic	Analysis and interpretation, manuscript reviews
Ewald Weber	Hardware design and manufacture, manuscript reviews
Feng Liu	Analysis and interpretation, manuscript reviews
Stuart Crozier	Analysis and interpretation, manuscript reviews

4.1. Introduction

As illustrated in chapter 3, phased array coils (PACs) and a single rotating coil accelerated acquisitions differently and thus each had limitations and advantages. PACs need more coils to further reduce the scan time however, this raises other issues related to RF coil performance that may undermine the capability of parallel imaging and parallel transmission. For a single element RRFC, in order to achieve a higher reduction factor with the dedicated TDM-SENSE algorithm [40], the ADC sampling rate and (mechanical) rotation velocity need to be increased, which could be a practical issue particularly for large volume coils.

The aim of this chapter is to strategically combine the array structure and the rotating concept to potentially address those limitations and achieve better performance. A new algorithm was developed for the rotating RF coil array (RRFCA) to provide higher imaging acceleration factors and reconstruction without significant B_1 inhomogeneity. During the course of rotation, each coil in the rotating RF coil array (RRFCA) provided a larger number of distinct and useful sensitivity profiles (as a function of time/rotation) for acceleration. This means that to reach the same reduction factor, fewer coils are needed, allowing room for larger coils to benefit parallel imaging and parallel transmission. An additional benefit of this scheme is the increased signal-to-noise ratio (SNR) owing to increased number of coils, thus potentially providing better image quality.

The proposed transceive rotating coil array were used for imaging a homogeneous phantom at 7 T. However, as demonstrated in Chapter 3, if the coil array was excited in the commonly used

circularly-polarised (CP) mode [79, 130], centre-brightened and periphery-darkened images were typically seen at 7 T. Compared to conventional methods introduced in Chapter 3, the RRFCA offered additional spatial degrees of freedom that could be used to mitigate the B_1 inhomogeneity.

In this chapter, a 4-element RRFCA model with a human head-sized homogeneous phantom was first numerically tested. New algorithms for acquisition acceleration and B_1 shimming strategy were investigated and developed for the RRFCA. An RRFCA prototype was then built and tested at 7 T to validate the numerical results.

4.2. Method

4.2.1. General Theory

4.2.1.1. SENSE for Stationary Phased Array Coils (PACs)

In SENSitivity Encoding (SENSE), the phased array coils are employed to provide multiple sensitivity profiles, which are used to partially replace Fourier encoding by magnetic field gradients [12]. Each RF coil weighs the received MR signal with its sensitivity, which has both magnitude and phase. Consequently, the density of *k*-space samples can be reduced by exploring the redundancy of signals, thereby reducing the image acquisition time. Since the *k*-space is partially acquired, image reconstruction with the inverse Fourier transform will generate aliasing artefacts. The general method to reconstruct an image is to solve a system of simultaneous linear equations:

$$Ax = b \tag{4.1}$$

where A is the encoding matrix in the form of Eq. 4.2; x is the unknown image; b denotes the *k*-space data acquired in the experiment, arranged in a vector form with size $(c \times K) \times 1$, wherein c denotes the number of the receivers, and K denotes the size of the *k*-space acquisition. To resolve N pixels with R times acceleration, the length of K is N / R.

In matrix form, A is given by:

$$A = \begin{bmatrix} \begin{pmatrix} e_{1,1}S_{1,1} & \cdots & e_{1,n}S_{1,n} \\ \vdots & \ddots & \vdots \\ e_{k,1}S_{1,1} & \cdots & e_{k,n}S_{1,n} \end{pmatrix} \\ \vdots \\ \begin{pmatrix} e_{1,1}S_{c,1} & \cdots & e_{1,n}S_{c,n} \\ \vdots & \ddots & \vdots \\ e_{k,1}S_{c,1} & \cdots & e_{k,n}S_{c,n} \end{pmatrix} \end{bmatrix} \tag{4.2}$$

where $k \in [1, K]$, $n \in [1, N]$

where A is formed by concatenating c blocks of matrices, each of which represents the encoding matrix of the corresponding coil c. $e_{k,n}$ and $S_{c,n}$ represent the Fourier and sensitivity encoding kernels as function of the voxel position, respectively. The explicit expression of matrix A is:

$$A_{c,k}(n) = e^{ikn} S_c(n) \tag{4.3}$$

where n denotes the position of the *n-th* voxel, k is the *k-th* sampling position in k-space and S_c is the complex spatial sensitivity of the *c-th* coil. The size of A is $(c \times K) \times N$,

The received noise increases as gradient encoding is partially substituted by the RF sensitivity encoding [11]. In parallel image reconstruction, the noise amplification is characterised by the RF coil-dependent geometry factor map (g-map) [11], which can be calculated as follows:

$$g = \sqrt{[(S^H \psi^{-1} S)^{-1}]_n (S^H \psi^{-1} S)_n} \tag{4.4}$$

where S is the sensitivity matrix and n denotes the voxel under consideration within the set of voxels to be separated, and ψ is the receiver noise correlation matrix.

4.2.1.2. Rotating-SENSE for Rotating Radiofrequency Coil Array (RRFCA)

For stationary arrays, the sensitivity profiles for encoding matrix remain unchanged from row to row within the same block (i.e. same coil). The number of sensitivity maps is therefore limited by the number of stationary coils. The RRFCA encoding matrix has a similar form to Eq. 4.2; nevertheless, the encoding matrix for RRFCA needs to take into account the varying sensitivity profiles:

$$A^R = \begin{bmatrix} \left\{ \begin{pmatrix} e_{1,1}S_{1,1,1} & \cdots & e_{1,n}S_{1,n,1} \\ \vdots & \ddots & \vdots \\ e_{M,1}S_{1,1,1} & \cdots & e_{M,n}S_{1,n,1} \end{pmatrix} \right. \\ \vdots \\ \left. \begin{pmatrix} e_{k-M+1,1}S_{1,1,t} & \cdots & e_{k-M+1,n}S_{1,n,t} \\ \vdots & \ddots & \vdots \\ e_{k,1}S_{1,1,t} & \cdots & e_{k,n}S_{1,n,t} \end{pmatrix} \right\} \\ \vdots \\ \left\{ \begin{pmatrix} e_{1,1}S_{c,1,1} & \cdots & e_{1,n}S_{c,n,1} \\ \vdots & \ddots & \vdots \\ e_{M,1}S_{c,1,1} & \cdots & e_{M,n}S_{c,n,1} \end{pmatrix} \right. \\ \vdots \\ \left. \begin{pmatrix} e_{k-M+1,1}S_{c,1,t} & \cdots & e_{k-M+1,n}S_{c,n,t} \\ \vdots & \ddots & \vdots \\ e_{k,1}S_{c,1,t} & \cdots & e_{k,n}S_{c,n,t} \end{pmatrix} \right\} \end{bmatrix} \tag{4.5}$$

where $k \in [1, K]$, $K = N / R$, $n \in [1, N]$, $t \in [1, N / M / R]$, M is the length of a k-space line.

where the element of A^R is written as: $A^R_{c,k,t}(n) = e^{ikn} \boldsymbol{S}_{c,t}(n)$.

It is clear that the Fourier encoding kernel is consistent between the stationary and rotating array; however, it can be seen from Eq. 4.5 that, sensitivity encodings for each coil c (in each curly braces) at different step t (in round bracket) are different to each other as the coil rotates. Therefore, more variations exist between the rows of the system matrix, which can potentially be used to improve its condition. These additional degrees of freedom can be exploited to further reduce the scan time.

The noise behaviour analysis of the rotating-SENSE is similar to that of the stationary case. However, to employ Eq. 4.4 for noise analysis, the encoding matrix A^R was represented as multiplication of two matrices as [131]:

$$A^R = FS \tag{4.6}$$

where F and S represent the Fourier encoding matrix [11] and sensitivity matrices, respectively. Eq. 4.6 delineates F and S, while the latter is used to calculate the g-maps by using Eq. 4.4.

4.2.2. RRFCA Optimisation

4.2.2.1. Coil Geometry Optimisation & Comparison

In this study, the stationary coil array and rotating coil array were compared in terms of parallel imaging acceleration ability. Typically, the coil size is closely related to the parallel imaging and parallel transmission [132] performance [23, 24, 101, 133]. Larger coils can penetrate deeper, providing improved performance in transmission and reception, albeit at a higher mutual coupling and noise propagation, which consequently degrades the imaging and transmission performance. In the rotating scheme, each coil of the RRFCA generates a number of sensitivity profiles depending on its position. To begin a comparative process, an 8-element stationary PACs was first optimised. To provide a balanced comparison, the elements of the 4-channel RRFCA and the stationary 8-channel PACs had the same physical dimensions.

To eventually facilitate neuroimaging, the diameter of coil former for the 8-element PACs was set to 280 mm. The width of each element was set at 90 mm, leaving enough interspace (20 mm) for accommodating the counter-wound inductive decouplers. Once the width of the coil was determined, the B_1 penetration depth and mutual coupling were only related to the longitudinal length of coil. The B_1 penetration depth was characterised by the normalised magnetic field strength calculated along the axis orthogonal to the coil at the z = 0 plane. The calculation was facilitated by using a commercially available package FEKO (EMSS, SA). FEKO is a computational electromagnetics software package which is based on the Method of Moments (MoM) integral formulation of Maxwell's equations. FEKO/MoM is especially suitable for coil simulation and field calculation for homogeneous phantom because it employs surface meshing that significantly reduces the number of unknowns, instead of using volume meshing of the entire calculation space. Figure 4-1 (e) illustrates the magnetic fields from the proximal end to distal end. Figure 4-1 (a) shows that a larger coil had a smaller magnetic field strength in the proximal region (section a: 0 mm to 35.2 mm). In section b (35.2 mm to 105.6 mm), coils of different sizes seemed to produce magnetic fields with similar strength. Beyond the centre point (section c: 105.6mm to 220 mm), it is revealed that larger coils penetrated deeper into the sample. Magnetic fields measured at sections a, b and c, and their coefficients (c_1, c_2 and c_3) were adopted for optimising the coil size. The relationship between coil size and mutual coupling is shown in Figure 4-1 (d). We note that the mutual coupling increases with the coil size. The coil size was optimised as follows:

$$\max\left\{c_2 \cdot m_2 + c_3 \cdot m_3 - c_1 \cdot m_1 - c_4 \cdot m_4\right\} \tag{4.7}$$

where, c_1, c_2, c_3 denote coefficients for normalised magnetic field; m_1, m_2, m_3 are the calculated magnetic field strength; m_4 and c_4 are mutual coupling vector and its coefficient, respectively.

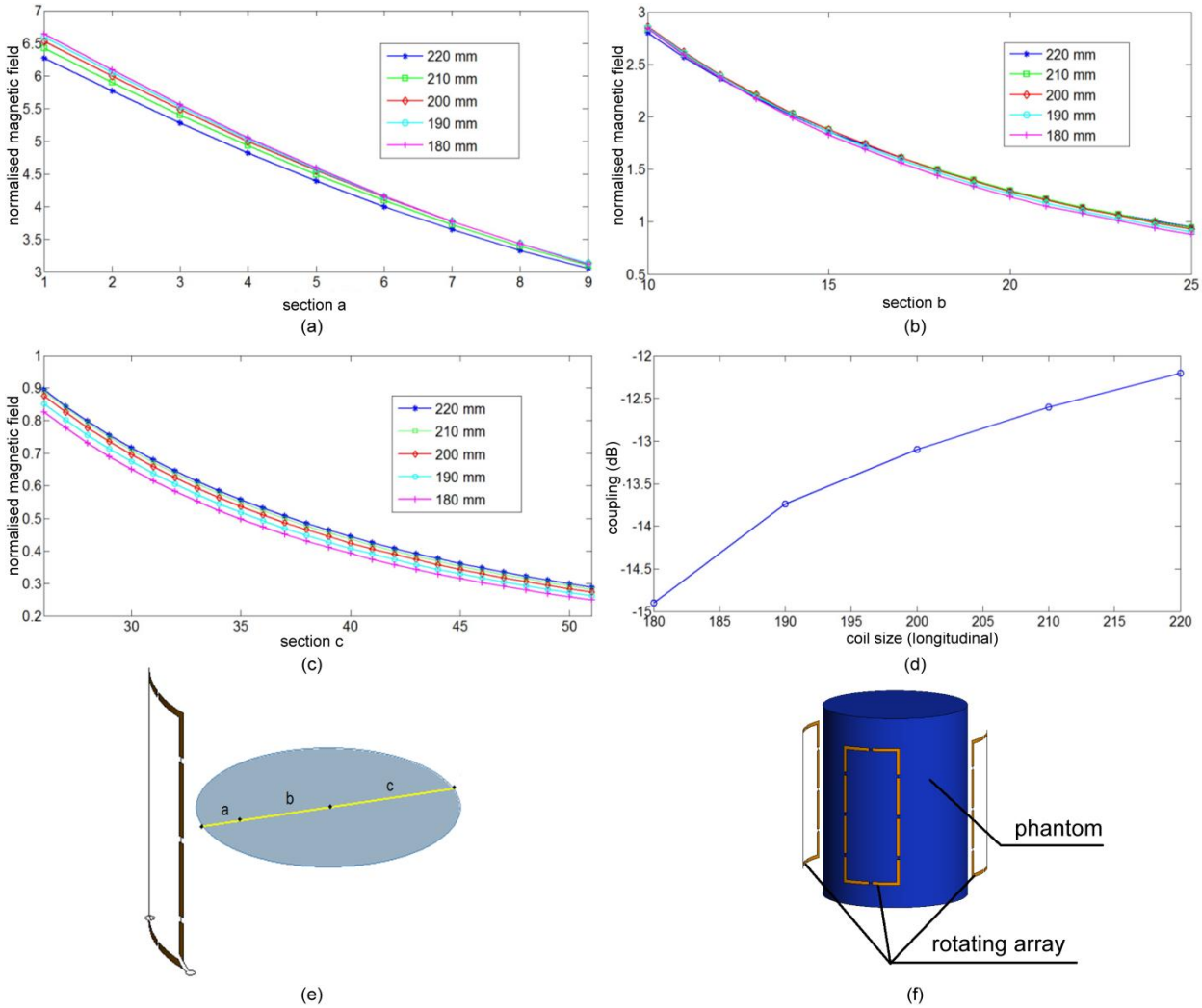

Figure 4-1. Penetration depth (normalised magnetic field) and coupling with varying coil sizes from 180 mm to 220 mm. (a) Normalised magnetic field in proximal end (section a); (b) normalised magnetic field in middle end (section b); (c) Normalised magnetic field in far end (section c); (d) Relationship between mutual coupling and coil. (e) Illustration of normalised magnetic field along axes at z = 0 plane; (f) Illustration of proposed RRFCA

The proposed RRFCA consisted of four coils as shown in Figure 4-1 (f). Similar to the structure of the single-channel RRFC, the RRFCA had three layers. The outer and inner layers formed a U-shape shell, which was stationary, providing support for the rotor and isolation to the patient. The middle layer, where the RF elements were attached, was rotatable. The diameter of inner layer and outer layer were set to 250mm and 300mm, respectively.

4.2.2.2. Sensitivity Encoding Optimisation

In the previous works [40, 41], the RRFC rotated about the subject continuously. In order to improve the sensitivity encoding ability of the RRFCA, we firstly modify the previous continuous rotating into a stepping fashion as shown in Figure 4-2, and then strategically choose

angular sampling positions in the stepping fashion according to Eq. 4.8. As illustrated in Figure 4-2, the proposed RRFCA coil rotated in a counter-clockwise direction starting from the *t-th* angular position. At each angular position, the coil sampled one phase-encoding line. The angular displacement θ between adjacent acquisitions was calculated to achieve the best imaging acceleration performance (minimised *g*-factor) as follows:

$$\underset{\theta}{\operatorname{argmin}}\left\{\sqrt{\frac{\sum_x\sum_y(g_{x,y}(\theta)-1)^2}{N}}\right\} \tag{4.8}$$

where θ was the angular displacement between two *k*-space lines, $g_{x,y}(\theta)$ was the g-factor calculation at voxel (x, y) in an image with N pixels. The summation was performed in both directions over the entire image.

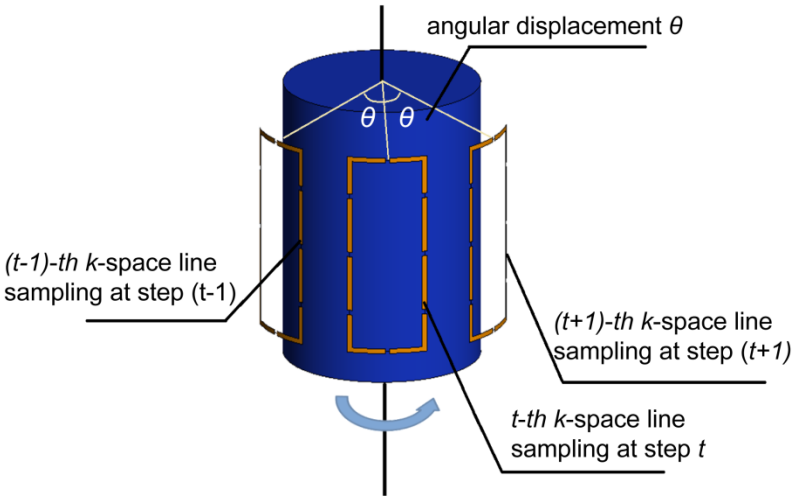

Figure 4-2. The illustrations of stepping mode by a single rotating element in the RRFCA. The coil visits three sampling positions from (*t-1)-th* step angular position on the left to right counter-clockwisely. Interval of each sample position is θ. By optimising θ, imaging acceleration ability of RRFCA is maximised.

4.2.3. Prototyping

The 4-element RRFCA was numerically modelled and the circularly polarised components of the steady state magnetic field were calculated to generate signal intensity (*SI*) images. The images were then compared with the experimental *SI* image to validate the accuracy of the numerical calculations. The good correlation between the two images permitted further investigation of B_1 shimming strategies and image reconstruction by means of rotating sensitivity encoding.

4.2.3.1. Experimental Setup

The 4-element RRFCA prototype consisted of four coils, each of which was 90 mm in width (transversal) and 210 mm in length (longitudinal) determined by the optimisation results of Eq. 4.7. Coils were placed equidistantly around the coil former (ϕ: 280 mm). The acrylic cylindrical phantom (ϕ: 220 mm, h: 300 mm) was filled with a liquid solution consisting of 2.62 g (0.0448 mol) NaCl and 2.14 g (0.0047 mol) $NiSO_4\,6H_2O$ per 1000 g distilled water. The dielectric properties of the resulting solution were subsequently measured with the Dielectric Assessment Kit (SPEAG, Switzerland) as ε_r = 78.35 and σ = 0.53 S/m, respectively. All images were acquired on a Siemens 7 T whole body system (Magnetom 7 T, Siemens Healthcare, Erlangen, Germany) with standard FLASH sequence as shown in Figure 4-3 (a).

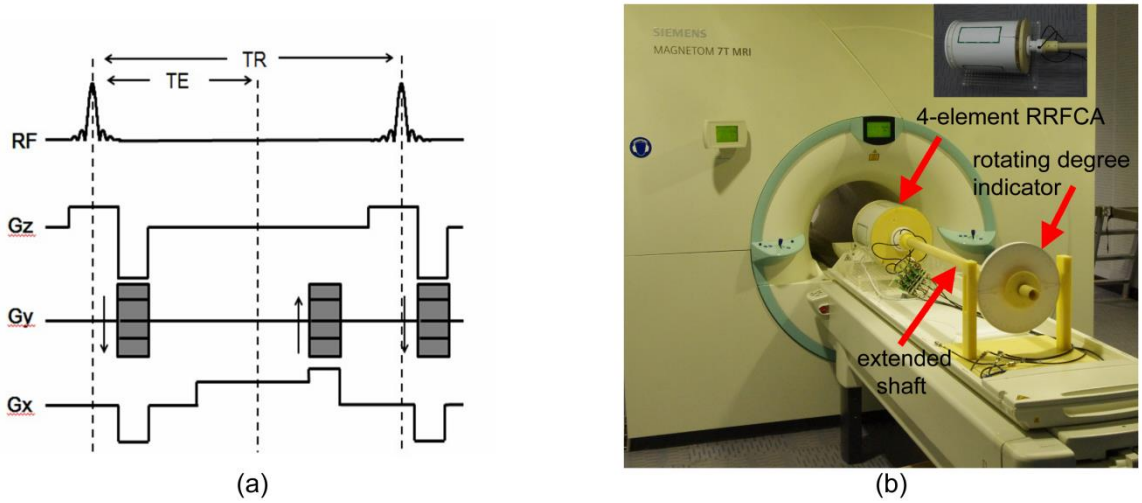

Figure 4-3. (a) The standard FLASH sequence. Repetition time (TR) is 300ms and Echo time (TE) is 7.9ms. (b) Experimental setup for RRFCA in CP-mode. Extended shaft allows adjusting rotating degree of RRFCA manually outside the tunnel without moving the RRFCA in and out from tunnel. This is important for the accuracy of experiment. The angular position is measured with a resolution of 1 degree using the rotation degree indicator.

In the stepping mode, after transmitting and receiving one *k*-space line of data at one angular position, the RRFCA moved to the next position for the subsequent sampling. In this preliminary study, the stepping angle was manually adjusted. The angular displacements were determined according to the sensitivity encoding optimisation results. At each required position, a complete *k*-space matrix was acquired. The accelerated acquisitions with RRFCA were achieved retrospectively; that is, corresponding *k*-space lines were extracted and combined to numerically model the *k*-space data in stepping mode with a reduction factor *R*. The experimental setup is shown in Figure 4-3 (b).

The Siemens standard Dual Echo Steady State (DESS) sequence was employed to acquire B_0 map with the 4-element transceive array. The B_0 map was then used to determine the current adjustment of second-order shim coil to realise the B_0 field corrections over a region that slightly larger than the phantom. The current adjustment stopped till the full width at half maximum was less than 10Hz and the shim current kept constant throughout experiment.

4.2.3.2. Numerical Calculations

Numerical simulations were performed according to the experimental setup as described in the previous section. All simulations were performed using FEKO. Programs for post-processing and optimisation were written in MATLAB (Mathworks, Natick, MA). The steady state RF magnetic fields were transferred from FEKO to MATLAB in order to calculate the circularly polarised magnetic field [53] and signal intensity [53, 77, 134]. The elliptical magnetic fields can be decomposed into two circularly polarised components as:

$$B_1^+ = \frac{\left(B_x + iB_y\right)}{2} \tag{4.9a}$$

$$B_1^- = \frac{(B_x - iB_y)^*}{2} \tag{4.9b}$$

where B_1^+, B_1^-, B_x and B_y denote the position dependent complex magnetic field quantities; B_x and B_y are the vector components calculated in FEKO, i is the imaginary unit, * asterisk indicates the complex conjugation.

By employing B_1^+ and B_1^-, the *SI* image for a single coil can be estimated as [77]:

$$SI_{calc} = W_0 \left|(B_1^-)^*\right| \sin(V\gamma\tau \left|B_1^+\right|) \tag{4.10a}$$

where W_0 is proportional to the proton density distribution, that is the water content within the voxels that contributes to the magnetic resonance (MR) signal; $\left|B_1^+\right|$ which is the magnitude of B_1^+ field calculated when the driven voltage V of the coil is 1V. γ is the gyromagnetic ratio, τ is the RF pulse duration.

In this work, the coil array was excited in circularly polarised (CP) mode, and the SI_{calc} of the coil array is calculated as the sum of squares of individual coil images:

$$SI_{calc} = \sum_1^c \left(SI_{calc-CP}\right)_c^2 \tag{4.10b}$$

where *c* counts the number of the coils, and $SI_{calc-CP}$ stands for *SI* image of each coil under the CP-mode excitation.

4.2.4. Homogeneous Image Reconstruction by Rotating SENSE

4.2.4.1. Ensemble B_1^+ Shimming Strategy

At ultra-high fields, B_1^+ shimming is typically required for conventional array coils to achieve homogenous excitation. Given that a large number of transmit profiles are available with the rotating scheme, more degrees of freedom are available for mitigating the B_1^+ inhomogeneity. In the stepping mode of RRFCA, each *k*-space acquisition in phase direction is associated with a unique angular position, and therefore unique transmit and receive sensitivities. This implies that lost signals (dark spots) in one angular position could be compensated at other angular positions, as long as the 'ensemble' B_1^+ is homogeneous.

The 'ensemble B_1^+' is not an instantaneous excitation profile as the common notion of B_1^+; instead, it can be expressed as the summation of B_1^+ profiles during all acquisitions. Homogeneous ensemble B_1^+ represents equalised excitation of each voxel throughout the scan. By optimally choosing the excitation phase of each individual channels, the ensemble B_1^+ can be homogenised.

$$\arg\min_{\alpha} \left\| \sum_{p=1}^{t} \sum_{c=1}^{c} \left| (B_1^+(V,\alpha))_c \right|_p - \left| B_1^+ \right|_{desired} \right\|_2 \tag{4.11}$$

where $|B_1^+|_{desired}$ represent the magnitude of desired uniform excitation profile. $\left|(B_1^+(V,\alpha))_c\right|_p$ is the magnitude of excitation profiles passing *t* angular positions with an array with *c* channels. *V* and α are the excitation voltage and phase for each channel, respectively. They remain unchanged for all acquisitions. In this work, only the phases of channels were set as optimisation variables.

4.2.4.2. Homogeneous Image Reconstruction Preparation

The *k*-space data with ensemble B_1 shimming as described by Eq. 4.11 was simulated. SI_{calc} images at each optimised angular position were calculated according to Eq. 4.10 and then transformed into *k*-space. The *k*-space lines with corresponding phases were extracted and used to form the equivalent *k*-space data for the RRFCA in the stepping mode. Uniform undersampling was then achieved along the phase encoding direction.

Since each acquisition of the RRFCA is associated with different excitation and reception profiles, the image reconstruction requires a different approach to that of conventional imaging. By

introducing the concept of composite sensitivity that includes the contribution to the image from both excitation and reception, the proton density weightings can be extracted using a reconstruction algorithm in a similar form to conventional parallel imaging. The composite sensitivity can be expressed as:

$$sensitivity_{com} = \sin(V\gamma\tau \mid B_1^+ \mid_{shim}) B_1^- \tag{4.12}$$

where $sensitivity_{com}$ is the composite sensitivity, which is the combination of specific transmit profile $\left|B_1^+\right|_{shim}$ and the coil sensitivity B_1^- . $\left|B_1^+\right|_{shim}$ and B_1^- were calculated by numerical simulations.

4.2.5. SNR

In MRI, one of the main drives to increase the main magnetic field strength (B_0) is to improve the SNR. At low field, the B_1^+ and B_1^- are relatively independent of B_0 because of the much longer wavelength inside the sample, leading to the independence of SNR from both B_1^+ and B_1^- . Compared to low-field MRI, in ultra-high field MRI, the B_1^+ and B_1^- vary dramatically in the image domain, and the SNR varies spatially with RF fields [78, 135]:

$$\frac{V_{signal}}{V_{noise}} \propto \frac{B_0^2 W \sin(\tau V\gamma \mid B_1^+ \mid)\left|(B_1^-)^*\right|}{\sqrt{P_{sample}}} \tag{4.13}$$

where W is the weighting factor related to tissue- and sequence-specific factors. τ, V, γ are the same parameters explained in Eq. 4.10 . P_{sample} is the power dissipated throughout the sample.

In parallel imaging with the coil array, the SNR is penalised by the reduction factor R and geometric factor g [11]:

$$\frac{SNR_{PPI}}{SNR_{full}} = \frac{1}{g\sqrt{R}} \tag{4.14}$$

where SNR_{full} and SNR_{PPI} denote the SNR without and with acceleration. The SNR produced by the 8-PACs and 4-RRFCA as function of the reduction factor was numerically analysed according to Eq. 4.13 and Eq. 4.14.

4.3. Results

4.3.1. *SI* Mapping and Comparison

The experimentally acquired FLASH image in CP mode is shown in Figure 4-4(a). After applying scaling factor W_0 and $U = V\gamma\tau$ obtained as [136], the simulated image SI_{calc} in Figure 4-4 (b) showed little difference compared with the experimental data. The excitation profile of CP mode, the corresponding flip angle map and the single coil receive sensitivity profile are shown in Figure 4-4 (c), (e) and (d), respectively.

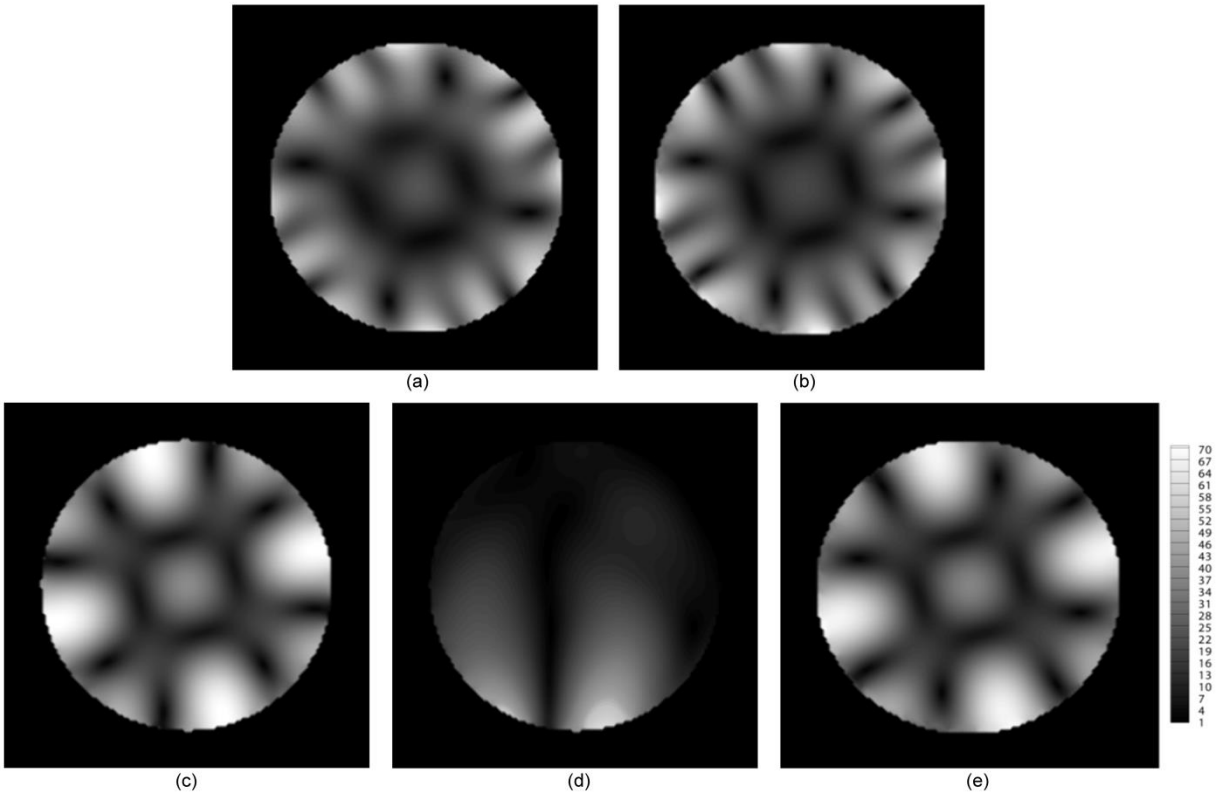

Figure 4-4. Experimentally acquired and simulated *SI* image. (a) SI_{exp} at 60˚ position. (b) SI_{calc} after applying the mapping coefficient at 60˚ position; (c) B_1^+ in CP mode with 4-element RRFCA (simulated). (d) B_1^- of single coil (simulated). (e) flip-angle after applying the coefficients (simulated).

The maximum and average flip angles in CP mode were around 70˚ and 18˚, respectively. A good correlation between SI_{calc} and SI_{exp} validated the numerical calculations, which allowed us to accurately investigate the subsequent B_1 shimming and image reconstruction using numerical simulations.

4.3.2. B_1 Shimming Result from Simulation

Without B_1 shimming, the B_1^+ profile excited under CP mode is shown in Figure 4-5 (a). Since the wavelength was shorter than the diameter of the phantom, the signal loss caused by destructive interference was clearly seen in the form of dark spots. Combined with the centre-brightening as a result of constructive interference, the excitation was extremely inhomogeneous. With an ensemble B_1^+ shown in Figure 4-5 (b), it was not feasible to reconstruct a homogeneous image by RRFCA. However, by strategically choosing the individual drives of each channel as illustrated in Eq. 4.11, a specific excitation profile can produce a homogeneous ensemble B_1^+ once the RRFCA has visited all the angular positions. Since multiple RF amplifiers might not be widely available, here a more feasible approach of adjusting the phases of individual channels was simulated. Setting the phases of each channel to 161˚, 112˚, 73˚ 31˚, produces the corresponding B_1^+ profiles shown in Figure 4-5 (c). In contrast to conventional B_1 shimming for stationary PACs at 7T, the adjusted excitation profile of RRFCA (Figure 4-5(c)) was inhomogeneous for each transmission. However, the superposition of such a B_1^+ field profile over all angular positions generated a homogeneous ensemble B_1^+ as shown in Figure 4-5 (d). By comparing Figures 4-5 (b) and (d), it is clear that the circular signal dropout in Figures 4-5 (b) can be successfully compensated.

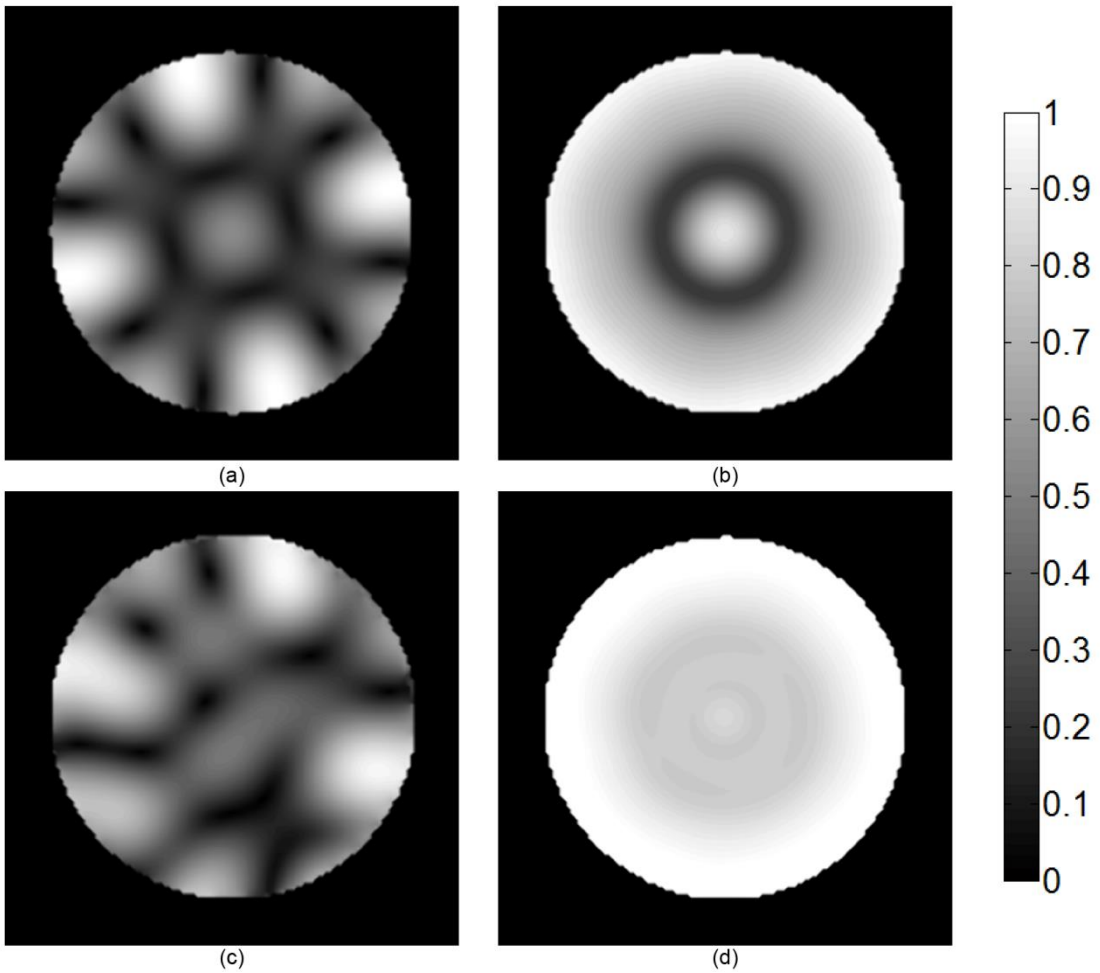

Figure 4-5 (a) B_1^+ in CP mode by simulation (b) ensemble B_1^+ of RRFCA under CP mode excitation. (c) B_1^+ shimming profile at certain angular position. (d) Homogeneous ensemble B_1^+. The plots are normalised.

4.3.3. Composite Sensitivity and g-map Comparisons

Under this scheme, composite receive sensitivity was dependent on B_1^+. As shown in Figure 4-6 (b), the composite sensitivity calculated using Eq. 4.12 had more variations compared to the traditional sensitivity in Figure 4-6 (a). More unique profiles could potentially further improve the parallel imaging performance due to the increased orthogonality of sensitivity encodings.

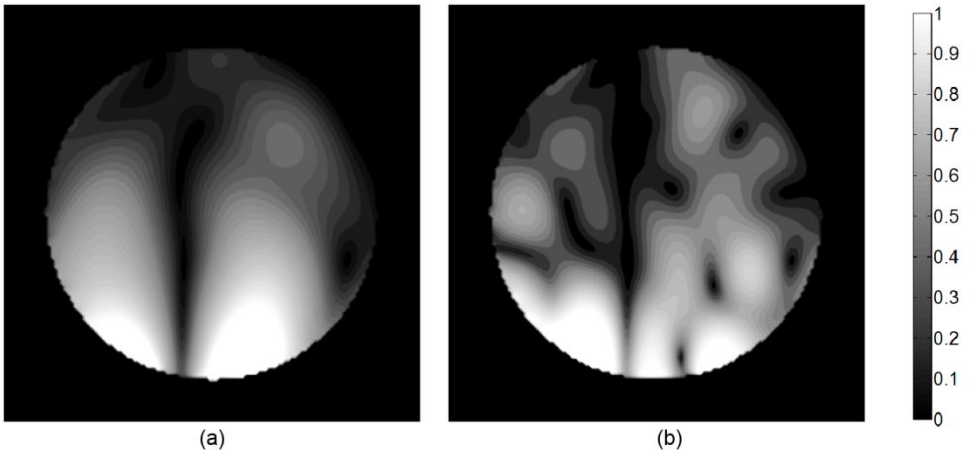

Figure 4-6. (a) Sensitivity profile under homogeneous excitation for stationary PACs. (b) Composite sensitivity for RRFCA under specific excitation. The plots are normalised.

The *g*-map is an important visualisation tool to analyse the performance of imaging acceleration. In Figure 4-7 (a), *g*-maps of 4-element RRFCA, 4-element PAC and 8-element PAC are compared as function of the reduction factor *R* (with *R* ranging from 2 to 4). This figure illustrates that under all reduction factors, the RRFCA had the most uniform *g*-maps and lowest max *g*-factors, that is, best noise suppression and imaging acceleration ability. The advantage of RRFCA over the stationary 4-element PACs (i.e. with the same number of coils) was evident from Figure 4-7. The *g*-maps of the RRFCA were also slightly better than those of the stationary 8-element PACs, even though the latter had twice as many elements. Figure 4-7 (b) displays the max *g*-factor of PACs and RRFCA at various reduction factors. With only 4 coils, max *g*-factors of stationary PACs increased from 1.2 to 4.9 (*R*: 2~4), while the same measure for the RRFCA only varied from 1.05 to 1.3, which was an improvement compared to the 8-element stationary PACs (i.e. with *g*-factors ranging from 1.1~1.7).

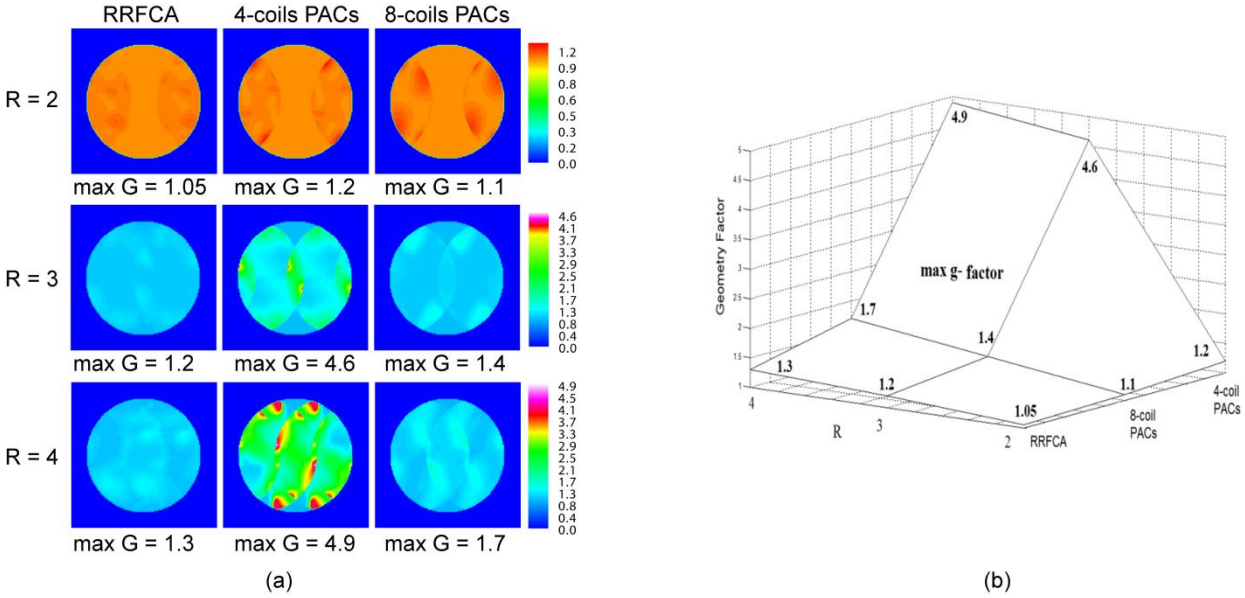

Figure 4-7. (a) left column, g-maps of RRFCA under different reduction factors; middle column, g-maps of 4-element stationary PACs under different reduction factors; right column, g-maps of 8-element stationary PACs under different reduction factors. (b) Max geometry factors obtained and plotted versus the type of coil array and the reduction factor *R*.

4.3.4. SNR Comparisons

In ultra-high field MRI, the stationary coil array normally has a higher SNR (brighter spots) near the coils along the wave propagation direction, but lower SNRs are commonly seen in areas between adjacent coils. The RRFCA is able to address this issue with the rotating scheme. In Figure 4-8 (a), the SNR maps of RRFCA, 4-element PACs and 8-element PACs are illustrated in the left, middle and right column respectively, at different reduction factors. Compared to the stationary PACs, the SNR of RRFCA was notably more uniform. Signals were evenly distributed within the subject as a result of sampling at multiple angular positions. Compared to the 4-element PACs, with the same number of coils, RRFCA had better SNR uniformity than its counterpart due to the rotating scheme. However, with twice as many coils, the SNR of 8-element PACs was comparable to that of RRFCA; nevertheless, spatial variations were apparent for the PACs. Figure 4-8 (b) shows that higher SNR of RRFCA was produced along the central axis of the phantom at z = 0 plane. Compared to the stationary PACs with the same coil element (red dotted line), the SNR of RRFCA (blue solid line) was not only higher, but also more uniform (i.e. with no significant signal dropouts). Compared to the RRFCA, the SNR of the 8-element PACs was only higher in the central region of the sample, albeit with significantly more variations across the FOV.

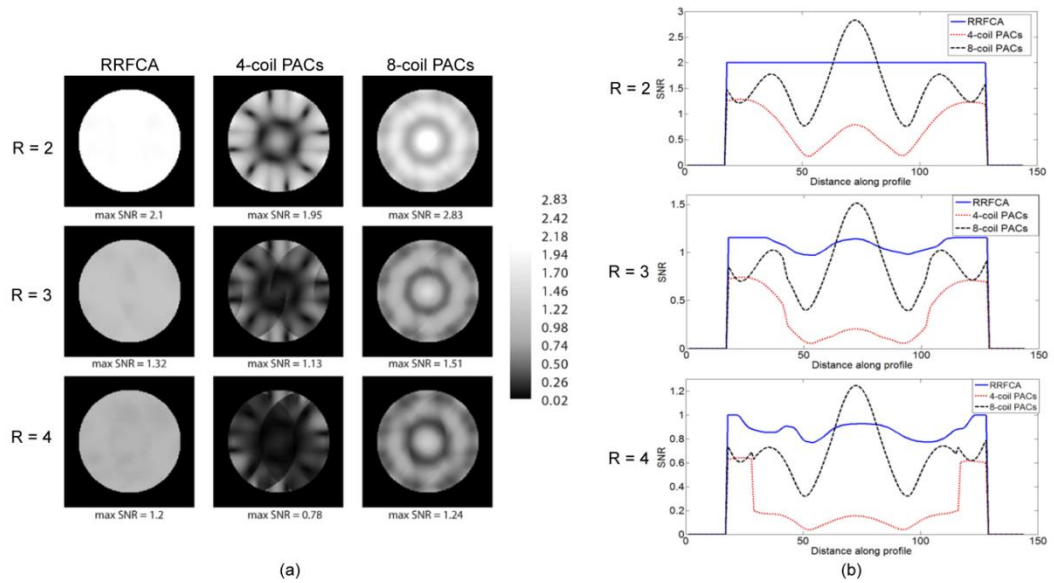

Figure 4-8. (a) SNR comparisons among RRFCA, 4-element PACs, 8-element PACs under different reduction factors. Left column, SNR of the RRFCA in stepping mode under different reduction factors; middle column, SNR of the 4-element stationary PACs under different reduction factors; right column, SNR of 8-element stationary PACs under different reduction factors.

(b) SNR profiles along axes of phantom at z = 0 plane for RRFCA, 4- and 8-element PACs under different reduction factors. From top to bottom, R = 2, 3 and 4 respectively.

4.3.5. Image Reconstruction and Error Maps

The simulated homogeneous phantom image reconstructions obtained with the RRFCA and 8-element PACs at R = 4 are shown in Figure 4-9 (a) and (c), respectively. A typical aliasing artefact was observable with the 8-element stationary PACs, and error map (d) also correlated with the same aliasing characteristics. Different from the stationary coil array, the rotating array displayed uniformly dispersed artefacts across the FOV, as shown in Figure 4-9 (b). When converged to the same level of residual, the RMSD (Root-Mean-Square-Deviation) and AP (Artefact Power) of RRFCA reconstructed image were 13.3% and 24% lower compared to the 8-element PACs, respectively (i.e. RRFCA: RMSD = $1.1e^{-2}$ and AP = $2.5e^{-4}$; 8-PACs: RMSD = $1.28e^{-2}$ and AP = $3.3e^{-4}$).

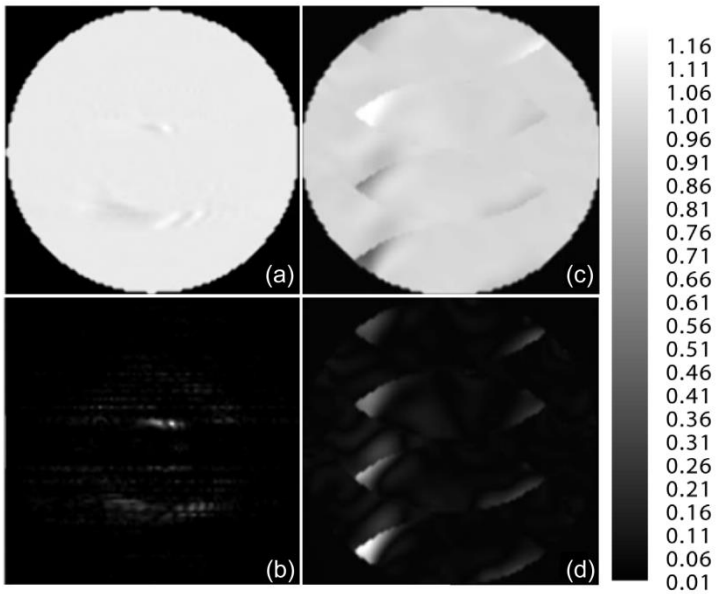

Figure 4-9. (a) Image reconstructed with RRFCA and (c) 8-element stationary PACs at R = 4. (b) and (d), error images of RRFCA and 8-element stationary PACs.

4.4. Discussion

4.4.1. On B_1^+ and B_1^-

Performing B_1 shimming and SENSE using RRFCA involves a large amount of sensitivity mappings. It is impractical to measure all B_1^+ and B_1^- profiles at all positions. Instead, B_1^+ and B_1^- were only acquired at several angular positions. At other positions, B_1^+ and B_1^- profiles were estimated by numerically rotating the acquired profiles, thanks to the use of homogeneous phantom and perfect symmetry of the experimental setup. An extended shaft was used to adjust the stepping angle of the coil just outside the MRI system without repositioning the coil-phantom set for each acquisition. Plastic foam was used to align the cylindrical coil former and the phantom along the z axis with good symmetry. Before sampling, several images at different angular positions were acquired and studied to ensure the alignment of RRFCA system and phantom. The alignment between RRFCA and phantom along the z direction was important to ensure accurately estimating sensitivity profiles by means of numerical rotation. In-vivo imaging may require multiple B_1 mappings. $\left|B_1^+\right|$ can be obtained by Actual Flip-angle Imaging method [98], and the B_1^- can be obtained by employing the inverse method [136] with the help of accurate numerical calculations.

4.4.2. On Practical Consideration

4.4.2.1. Cabling the Rotating Array

In our previous work [40, 41], the frictionless inductive coupler was used to transmit/receive signal for RRFC with continuous rotation. However, because of the different mechanisms for signal encoding and reconstruction, the RRFCA was not required to rotate continuously during sampling, but only to sample each *k*-space line at certain pre-calculated angular positions in different acquisitions. Since the angular displacement of coil array is between -180° and +180° for position control, RF cables for individual channels were properly extended (Figure 4-3 (b)) to accommodate any angular rotations within this range.

4.4.2.2. Motorising the Rotating Array

The reconstruction algorithm presented in the current study is based on SENSE [11], albeit with varying sensitivity profiles provided by rotating arrays. This SENSE-based algorithm requires accurate sensitivity mapping using pre-scans, which implies that the coil positions in actual imaging should be identical to those in the pre-scans. Inaccurate positioning would result in sensitivity misalignment and corresponding imaging artefacts. Methods to motorise the array coil with automatic and accurate coil-positioning will be investigated in our future studies. For example, piezoelectric motors are known for their excellent positioning accuracy, non-magnetic nature, high torque, fast response time and hard brake without backlash.

4.4.2.3. Rotation speed and Safety

The RRFC revolves about the subject in a continuous fashion and reconstruct image with TDM-SENSE [40] algorithm which needs a high rotation speed. The experiments on 2 T whole-body and 4.7 T small-animal showed that rotation velocity up to 1200 rpm (revolutions per minute) was sufficient to achieve good images [40]. It was evidenced that rotational velocity of small animal coils up to 20,000 rpm is feasible using air turbines and ceramic bearing [137]. However, in the present study, the RRFCA adopted SENSE-like encoding with stepping mode does not need high angular velocity. The time required for the transition of adjacent angular position is on the same order of the sequence repetition time (TR). For example, the average angular velocity required is merely 25 rpm for a 15° rotation in 100 ms. With such a rotation speed (on the order of 10 rpm), the acoustic noise induced by mechanical rotation is not considered significant. To ensure safety, the rotor of the RRFCA is fully enclosed by a stationary U-shape hollow shell, which isolates any moving mechanical parts from subjects.

The specific absorption rate (SAR) [138, 139] issue was not discussed in this preliminary study. However, local SAR control is of paramount importance for *in vivo* imaging. Complex tissue

distribution and the interaction with transmit coils may cause unpredictably high local SAR, which may cause tissue damage. Our initial study on this subject indicated that RRFCA with larger number of transmit magnetic and electric profiles can significantly increase the capacity in both B_1 shimming and local SAR control [140].

4.5. Conclusion

In this chapter, the imaging acceleration ability and an image reconstruction strategy for a 4-element RRFCA were numerically investigated and experimentally validated. Under the rotating scheme (stepping mode), each coil was capable of acquiring multiple sensitivity profiles, leading to good imaging acceleration performance demonstrated by uniform *g*-maps and small maximum *g*-factors (max-g = 1.3 at R = 4). The 4-channel RRFCA outperformed both the 4- and 8-element stationary PACs in terms of SNR uniformity and *g*-map. By carefully choosing the acquisition positions and corresponding transmit/receive profiles in the rotation scheme, the RRFCA was able to reconstruct uniform images for the homogeneous phantom at high reduction factors using relatively simple methods. In the next chapter, we report the RRFCA for *in vivo* imaging. However, since tissue-coil interactions become more complex in heterogeneous subjects, the simple sensitivity estimation methods used in this chapter are no longer suitable for *in vivo* applications. Therefore, a dedicated rotation-dependent *in vivo* sensitivity estimation algorithm will be developed in the next chapter.

Chapter 5

In vivo rotation-dependent sensitivity estimation and imaging acceleration for human brain imaging with rotating coil arrays at 7 T

In this chapter, the feasibility of using the RRFCA for human brain imaging was tested. Unlike homogenous phantoms, human heads have complex structures with heterogeneous dielectric properties. Therefore, the sensitivity estimation method used in the previous chapter for the homogeneous phantom is insufficient to accurately estimate *in vivo* rotation-dependent sensitivity. In order to use the proposed rotating rotating-SENSE algorithm introduced in Chapter 4 for fast imaging, a dedicated rotation-dependent sensitivity estimation method for *in vivo* imaging is developed in this chapter. This chapter is largely based on the journal article "*In vivo* sensitivity estimation and imaging acceleration with rotating RF coil arrays at 7 T", which was accepted for publication by the *Journal of Magnetic Resonance* in December, 2014. Slight editing has been carried out for best coherence with other chapters.

Publication details

Mingyan Li, Jin Jin, Zhentao Zuo, Feng Liu, Adnan Trakic, Ewald Weber; Yan Zhuo, Rong Xue, Stuart Crozier, *In vivo* Sensitivity Estimation and Imaging Acceleration with Rotating RF Coil Arrays at 7 Tesla, *Journal of Magnetic Resonance*, vol. 252, pp. 29-40, 2015

Manuscript revision history

Submitted to *Journal of Magnetic Resonance*	8 July 2014
Interim Decision (major revision)	20 August 2014
Revision submission	20 October 2014
Accepted	17 December 2014
Available online	26 December 2014

Author contributions

Mingyan Li	Numerical modelling, code implementation, analysis and interpretation, manuscript preparation.
Jin Jin	Numerical modelling, code implementation, analysis and interpretation, manuscript reviews
Zhentao Zuo	Hardware design and manufacture, experiment implementation
Feng Liu	Analysis and interpretation, manuscript reviews
Adnan Trakic	Analysis and interpretation, manuscript reviews
Ewald Weber	Hardware design and manufacture, manuscript reviews
Yan Zhuo	Experiment implementation, manuscript reviews
Rong Xue	Hardware design and manufacture, experiment implementation
Stuart Crozier	Analysis and interpretation, manuscript reviews

5.1. Introduction

As introduced in Chapter 4, the rotating-SENSE algorithm was developed for acquisition acceleration and image reconstruction with the rotating array. Similar to SENSE [11, 12], the rotating-SENSE algorithm requires sensitivity information for image reconstruction and acceleration. In the last chapter, a small number of sensitivity maps (B_1^-) acquired at several angular positions were numerically rotated to estimate the sensitivity at other positions. This technique was used for human brain imaging at 2 T [40, 41] owing to the relatively weaker coil-tissue interaction [141-145] (dielectric resonance [8, 130, 134, 146, 147]). In the previous chapter, this approach has also been used for imaging a homogeneous phantom at 7 T, provided the phantom and the RRFCA system are both symmetrical. However, this method is not applicable for *in vivo* sensitivity estimation at 7 T, because the *in vivo* sensitivity maps at different angular positions vary significantly due to the strong coil-tissue interactions. Since measuring the sensitivity at every angular position is impractical and affects fast imaging performance, a practical and robust sensitivity estimation method is needed for *in vivo* applications of the RRFCA at ultra-high fields.

In this chapter, a novel sensitivity estimation method is specially developed for *in vivo* applications of the RRFCA. Instead of simply rotating the acquired sensitivity to new angular positions, the *in vivo* sensitivity maps will be deformed in a non-linear fashion. These deformations can be calculated with image registration techniques by registering *in vivo* sensitivity profiles to those in a library acquired from volunteers scans or numerical calculations. This approach is based on the observation that the B_1^- map is not particularly sensitive to small local changes, in terms of dielectric properties and structures of tissues. Instead, B_1^- maps are typically related to the global dielectric property distribution relative to the RF system [21, 134, 148], with lower spatial frequencies. This sensitivity deformation can be modelled numerically using image registration techniques [149-151], as these techniques are commonly used in finding the spatial correspondence between two images. Additionally, image registration has recently found application in modelling the magnetic field variations due to changes in dielectric distributions between different subjects [15].

In this chapter, the proposed numerical method will be applied to estimate the sensitivity maps within a human head when RF elements are at various angular positions. The estimated sensitivity profiles will then be used to reconstruct images. Additionally, they can assist the optimisation of the rotating techniques, in which the rotation parameters are adjusted to minimise the maximum *g*-factor associated with the rotating coil array. The *g*-maps, reconstructed images and SNR maps of the RRFCA and stationary coil array will then be compared.

5.2. Methods and materials

As described in last chapter, the RRFCA moves to various angular positions during acquisition, so that different *k*-space phase-encoding lines are associated with distinct coil sensitivity profiles which improve encoding capability. In order to reduce the overall scan time, sensitivity maps at most angular positions are estimated from a small number of measured *in vivo* sensitivity maps, by employing the proposed algorithm. The linear superposition of individual sensitivity maps with global coverage of the sample can benefit the registration algorithm [152] (details are discussed in later sections). However, four physical elements with 90˚ intervals of the RRFCA prototype are insufficient to provide a complete coverage. Consequently, two sets of sensitivity maps, with angular separation of 45˚ (e.g. position 1: 0˚+45˚ in Figure 5-1), are used together to simulate a rotating array with 8 elements equidistantly distributed in the angular direction. Considering that all elements are identical, the range of angular displacement that the RRFCA needs to travel is from -22.5˚ to + 22.5˚. In order to test the robustness of the estimation algorithm at the maximum angular rotation, sensitivity with 22˚ displacement (position 3) from position 1 is estimated. In addition, the

intermediate angular position displacement (10˚ at position 2) is also estimated. (as shown in Figure 5-1, estimate B_1^- at position 2 and 3 from acquired B_1^- at position 1). To verify the robustness of the proposed algorithm, two volunteers of different genders and distinctly different head sizes were imaged.

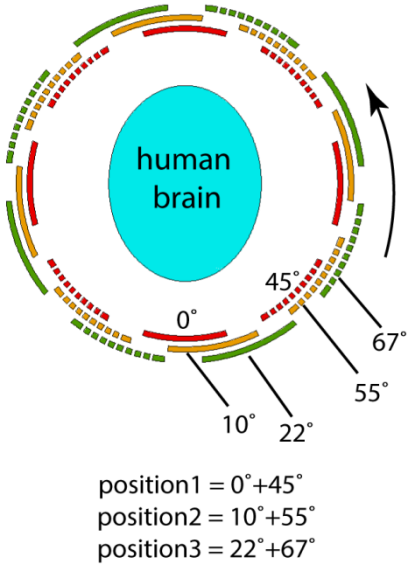

Figure 5-1. The sensitivity profiles of the 4-element RRFCA were acquired at angular positions at 0°, 10°, 22°, 45°, 55° and 67°, denoted with red, yellow, green, dashed red, dashed yellow and dashed green. Sensitivity maps acquired at these positions were recombined as three positions for better registration performance: position 1 (0° + 45°), position 2 (10° + 55°), position 3 (22° + 67°).

5.2.1. Registration based in vivo sensitivity estimation

In this work, the new sensitivity estimation method uses the acquired sensitivity at the initial position to estimate the sensitivity at other positions by employing a sensitivity library and registration techniques. The library provides source images, which are made up of sensitivity maps at all angular positions acquired during scans of volunteers. The registration techniques are employed to find the spatial transformation that aligns the source image (library sensitivity) to the target image (actual acquired sensitivity) from its initial position, and this transformation is applied to other angular positions for estimating corresponding sensitivity maps. The rotational sensitivity at arbitrary angular positions is acquired by following four steps:

(1). Create a library by acquiring sensitivity maps at all angular positions from the scans of the volunteers. During the actual patient scanning, sensitivity maps at an initial position (i.e., position 1 in Figure 5-1) are acquired. Image processing is applied to both groups of sensitivity maps to smooth profiles and correct singular values.

(2). Instead of registering individual coil sensitivity maps, they are linearly combined before being registered, to improve accuracy and efficiency. The combination coefficients are determined with a condition number of 1 to achieve the optimal sensitivity estimation when individual sensitivity profiles are later extracted (see Step (4)).

(3). As illustrated using a flow chart in Figure 5-2, the source profile $\overrightarrow{S_1^8}$ (combined 8 library B_1^- maps at position 1) is registered to the target profile $\overrightarrow{T_1^8}$ (combined 8 *in vivo* B_1^- maps at position 1). The corresponding transformation Ψ_1^8 is extracted and applied to the combined library sensitivity map at arbitrary angular position (α°) to obtain the estimated combined sensitivity map $\overrightarrow{E_\alpha^8}$.

(4).Repeat step (3) 8 times for all the linear combinations to estimate all the combined sensitivity maps. The individual sensitivity map $\overrightarrow{E_\alpha^1}$ at α° angular position (i.e., position 2, 3 in Figure 5-1) is calculated by multiplying the inverse of the coefficient matrix. N^2 in Figure 5-2 denotes the number of pixels.

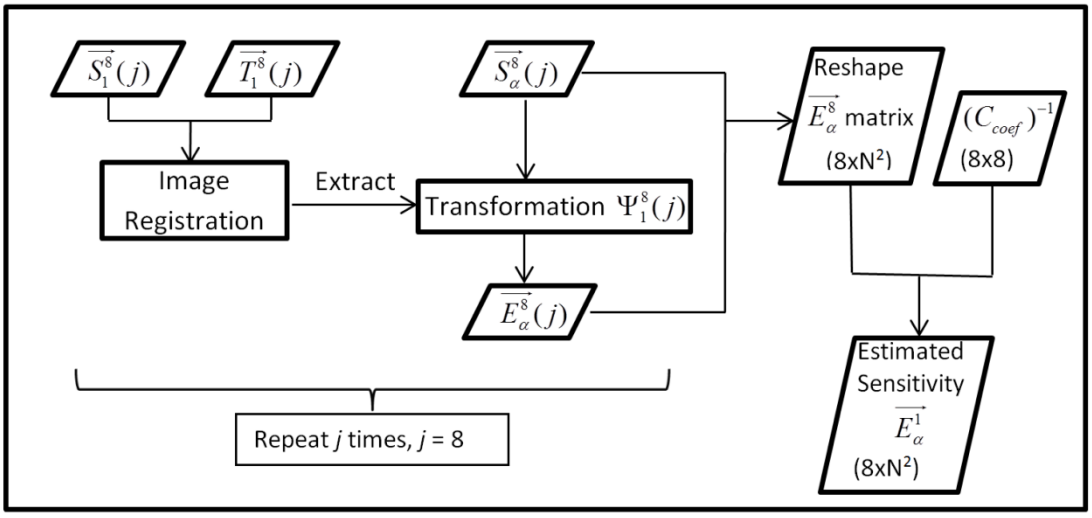

Figure 5-2. Flow chart of the registration based rotation-dependent sensitivity estimation.

5.2.1.1. In vivo sensitivity mapping and singular value correction

The most common sensitivity mapping method for a stationary coil array is to derive relative coil sensitivity by dividing the individual coil image using a predominantly uniform reference image. Both the coil image and the reference image can be obtained from either full *k*-space sampling [11, 153] or fully sampled central *k*-space [154, 155]. Without a uniform volume transmit coil, the reference image is typically approximated as the root sum of square (RSS) image:

$$RSS = \left| \sqrt{\sum_{j=1}^{J} (\vec{I}_j)^2} \right| \tag{5.1-a}$$

$$\vec{S}_j = \frac{\vec{I}_j}{RSS} \tag{5.1-b}$$

where J is the total number of coils in an array; $\vec{I}_j$ is the full-FOV image obtained with the j-th coil; $\vec{S}_j$ is the sensitivity map of the individual coil.

The direct division in Eq. 5.1-b can easily generate singular values. The different singular value distributions of each coil can cause inaccurate reconstructions which, particularly in this work, can misinform the registration process.

Singular values are commonly seen at the interfaces (i.e. skin and skull, skin and air) for both magnitude and phase of the sensitivity maps. In addition, the phase of sensitivity is often unpredictably wrapped for the ultra-high field MRI. To prepare sensitivity profiles for registration, a multi-level singular value removal algorithm was developed. Similar to methods employed in [156], the map was first divided into reliable and unreliable regions. The unreliable regions consist of singular values of the magnitude map, sensitivity voids and phase discontinuities [157]. An interpolation/extrapolation procedure [158], based on polynomial fitting, was then performed to correct the sensitivity profiles in the unreliable regions.

5.2.1.2.Optimal sensitivity combination

Due to the complex coil-tissue interactions at the ultra-high fields, after loading a heterogeneous subject like the human brain, the sensitivity of each coil becomes distinct [159]. For this reason, single coil sensitivity based estimation is compromised by insufficient coil-tissue information. In addition, the registration algorithm works less efficiently with signal voids that are commonly seen in single-channel sensitivity maps. For better estimation, sensitivity profiles are linearly combined before applying registration. A similar method has been reported for optimal B_1 mapping [152]. This process is expressed as:

$$C_{coef} S_{single} = S_{combined} \tag{5.2}$$

where C_{coef} denotes an 8×8 coefficient matrix; S_{single} is the sensitivity matrix resized to $8\times N^2$ (resolution is $N\times N$) and each row is a single coil sensitivity. $S_{combined}$ contains the linearly combined sensitivity maps.

During rotating, the coil-tissue interaction is fully transformed from one angular position to another and Eq. 5.2 is applied accordingly. As shown in Figure 5-2, to decompose the estimated individual coil sensitivity $\overrightarrow{E_\alpha^1}$ from estimated combined sensitivity maps $\overrightarrow{E_\alpha^8}$, the inversion of C_{coef} is multiplied to both sides of equation. With the method described in [152], the matrix C_{coef} is determined with condition number 1 to minimise error.

5.2.1.3. The registration technique for sensitivity estimation

The goal of registration is to find the spatial correspondence between the source and target images. Registration techniques are widely used in medical imaging [149, 150, 160, 161], such as when information from multiple modalities are combined (computed tomography (CT), MRI, positron emission tomography (PET)), intra-subject motion correction, distortion correction, dynamic imaging reconstruction and high-field MRI safety assessment [15]. A typical registration algorithm includes two components: a similarity metric and geometric deformation. The registration algorithm employed here followed, in part, previously published works [151, 162], while various components were adapted to suit the current application. For example, a similarity metric was modified to cope with complex-valued sensitivity maps.

Similarity metric

The similarity metric measures how well the source image aligns to the target image. Various metrics have been developed for image registration, such as squared difference (SD), mutual information (MI) [163, 164] and pattern intensity (PI) [165].

Sensitivity maps are complex images. Both magnitude and phase of B_1^+ and B_1^- exhibit a rotational property [159] which offers opportunities to apply image registration techniques for estimating sensitivity maps. Magnitude images are relatively easy to be registered because the features are clear; however, registering phase images is problematic due to phase-wrapping. Even when the phase images are unwrapped, the unwrapping quality and phase ranges are difficult to control which can undermine the registration performance. To avoid this problem, the registration process in this work was not solely performed on phase images, but on the complex sensitivity maps. The PI metric was modified to cope with complex numbers. The SD metric was chosen for

registering magnitude images due to its fast processing speed. Two registration processes were set to different convergence parameters for optimal performance.

For a source image $I_s(x,y)$ and a target image $I_t(x,y)$, a two-dimensional SD and PI are defined as:

$$SD = \frac{\sum_{x=1}^{X}\sum_{y=1}^{Y}(I_s(x,y)-I_t(x,y))^2}{XY} \tag{5.3-a}$$

$$PI_{r,\sigma} = \sum_{x,y}\sum_{(x-u)^2+(y-v)^2\le r^2}\frac{\sigma^2}{\sigma^2+(\left|I_{diff}(x,y)-I_{diff}(u,v)\right|)^2} \tag{5.3-b}$$
$$I_{diff} = I_t - I_s$$

where *x* and *y* are the voxel coordinates in the image, *X* and *Y* are the numbers of the voxels along each dimension. In Eq. 5.3-b, I_{diff} is the difference image. The parameter *r* defines the size of the neighbourhood, in which the variations are taken into account. The parameter σ is a sensitivity controller to decide whether the variation is a structure or not.

Geometric deformation

Two types of geometric deformation, affine transformation and non-rigid transformation, were employed in this work. The affine transformation included translations and rotations, making it best suited for global transformations. The non-rigid transformation was applied to compensate the inefficiency of the affine transformation in local areas. In the non-rigid transformation, a deformation field recorded all displacement vectors at each voxel from an aligned source image to the target image. In this work, a free-from deformation (FFD) based on B-splines [166] was adopted for non-rigid transformations. The FFD worked by deforming a source image by manipulating a mesh of control grids [167]. To improve its efficiency, a coarse-to-fine multilevel B-spline approximation was adopted to generate a series of B-spline functions incorporating bicubic interpolation functions for calculation of the deformed pixel values.

5.2.2. Image reconstruction and encoding optimisation

The rotating coil array emulates a large amount of coils with only four physical RF elements, thereby improving the condition of the encoding matrix to facilitate a higher reduction factor. However, the encoding ability of RRFCA can be further improved by strategically choosing the rotating degree for each stepping, which is determined by the *g*-map based optimisation algorithm [168].

5.2.2.1. Image reconstruction with rotating-SENSE

The number of sensitivity profiles limits the sensitivity encoding ability of a stationary coil array; therefore, the sensitivity profiles in the encoding matrix remain unchanged from row to row for each coil. However, the encoding matrix (A_R) of the RRFCA has more variations in its rows by taking rotational sensitivity into account:

$$A_R = \begin{bmatrix} ES_1 \\ ES_2 \\ \vdots \\ ES_4 \end{bmatrix} \tag{5.4}$$

where $E = e^{iK_\kappa r_\rho}$ and $S_j = S_j(r_\rho, t)$; $\kappa \in [1, \mathrm{M} \times N/R]$, $t \in [1, M/R]$, N is the length of a k-space line, M is the number of k-space lines and R is the reduction factor. E and S_j denote the Fourier encoding and sensitivity encoding matrices, respectively. K_κ denotes the κ-th k-space sampling position; r_ρ and t in S_j denote the sensitivity at the position of ρ-th voxel of the step t.

The Fourier encoding kernel is consistent between the stationary and rotating array; however, sensitivity maps for individual coils j at each step t are different as the coil rotates. This variation improves the condition of encoding matrix and can be exploited for further scan time reduction [168].

The noise behaviour analysis of the rotating-SENSE is similar to that of the traditional stationary array. However, to employ g-maps [11] for noise analysis, the sensitivity matrix S needs to be delineated from encoding matrix A_R:

$$A_R = FS \tag{5.5}$$

where F and S represent the Fourier encoding matrix and sensitivity matrix, respectively. The sensitivity matrix S consists of the acquired sensitivity and estimated sensitivity profiles. See [168] for the process of separating F and S.

5.2.2.2. Sensitivity encoding optimisation

The proposed method of estimating *in vivo* sensitivity maps enables us to investigate the optimal rotating scheme using numerical simulations. By optimally choosing the sampling position of each step, the sensitivity encoding capability can be maximised. At each angular position, the coil sampled one phase-encoding line. The angular displacement θ between adjacent acquisitions was determined by achieving the best imaging acceleration performance as follows:

$$\underset{\theta}{\operatorname{argmin}}\left\{\sqrt{\frac{\sum_{x=1}^{M}\sum_{y=1}^{N}(g_{x,y}(\theta)-1)^2}{M\times N}}\right\} \tag{5.6}$$

where θ denotes the angular displacement between two *k*-space lines, $g_{x,y}(\theta)$ is the *g*-factor calculation [11] at voxel (x, y) in an image with $M \times N$ pixels.

5.2.3. Experimental validation

The 4-channel RRFCA was used to scan two subjects, A and B, at 6 angular positions (0°, 10°, 22°, 45°, 55° and 67° in Figure 5-1). These data were firstly combined to simulate an 8-channel RRFCA (for reasons described previously). To test the proposed algorithm in an intra-subject case, images of subject A were acquired at two slices with 12 mm spacing. Sensitivity maps of one slice were used as the library. In the inter-subject case, sensitivity maps of subject A were used as the library to estimate sensitivity maps of subject B. The image registration techniques were then applied to both datasets for the estimation of the rotation-dependent sensitivity profiles at desired positions.

To study the rotating coil array in the reception mode independently without the complication from changing transmission profiles, a 4-element RRFCA was used as a receive-only coil array [168]. An additional transmit coil array was built to provide an unchanged and relatively uniform transmission. The experimental setup is shown in Figure 5-3 (b) with one healthy volunteer on a whole-body 7T MRI scanner (Magnetom 7T MRI, Siemens Medical Solutions, Erlangen, Germany). All imaging protocols were approved by institutional review board of Institute of Biophysics of Chinese Academy of Sciences (Beijing), and signed consent forms were collected. Small-flip-angle (FA = 30˚) GRE images of two slices were acquired with TE/TR = 4/1000 ms (in plane voxel size = 2mm × 2mm).

The RRFCA system consisted of three layers. The stationary inner layer was isolated from the rotating coils and provided support to a patient's head. The receive coils were attached to a rotatable middle layer and the transmit coils were attached to a stationary outer layer. The radius of the inner layer was set to 125 mm to comfortably accommodate the human head. As shown in Figure 5-3 (a) and (c), the transmit coil array consisted of eight loop coils, each of which was 160 mm in length and 130 mm in width. They were attached equidistantly to a coil former. A capacitance decoupling method was used to keep the coupling at a reasonably low level of −12dB ~ −14dB when loaded. To reduce the interaction and parasitic capacitance between the transmit and receive coils, besides employing active detuning circuits, a transmit coil former with a large radius should be used.

However, in order to minimise the signal drop caused by the increased distance and to guarantee consistent rotation, the radius of the middle layer was set to 140 mm to provide a 15 mm separation from the inner layer. (Figure 5-3 (a), $Ø_{transmit}$: 400mm, $Ø_{receive}$: 280mm).

An extended shaft [168] was used to adjust the rotation angle outside of the MRI tunnel without repositioning the coil-subject set for acquisition at each angular (stepping) position. However, unlike the experiment setup using phantoms [168], the rotation indicator and the extended shaft were installed at the rear of the magnet bore (Figure 5-3(b)) to allow enough space for the patient.

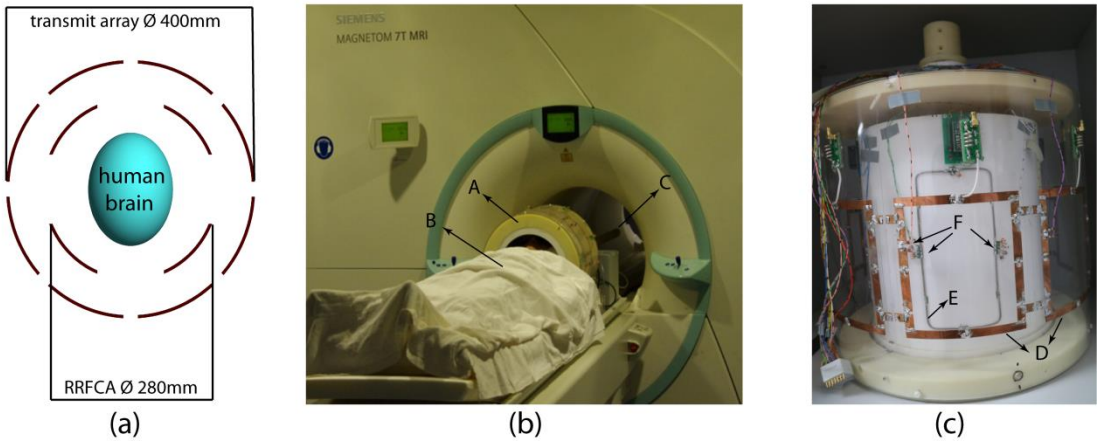

Figure 5-3. (a) Top view of the RRFCA setup. The outside layer is the stationary 8-element transmit coil array with 400 mm diameter, inner layer is the 4-element RRFCA with 280 mm diameter. (b). RRFCA system loaded with a volunteer. [A] RRFCA system. [B] Volunteer. [C] Extended shaft pointing to rear of MRI. (c). Close-up of the RRFCA system. [D] Transmit coils made of copper patches attached to outside stationary former. [E] Receive coil attached to the internal rotatable former. [F] Detuning circuits on both transmit and receive coils.

5.3. Results

Figures 5-4 (a) and (b) show the gradient recalled echo (GRE) images of two slices from subject A. The GRE image of subject B (same slice location as Figure 5-4 (b)) is shown in Figure 5-4 (c). Their corresponding sensitivity maps are shown in (d), (e) and (f). Since there is a large difference in head size and thus in global dielectric properties between subjects, large sensitivity variations are found even at the same slice location. As seen from Figures 5-4 (a) and (b), the anatomical structure and dielectric property of the two slices (subject A) from one subject are very different, but their sensitivity maps have minor changes shown in Figures 5-4 (d) and (e). This correlates with the observation that the sensitivity is more related to global dielectric changes rather than local changes.

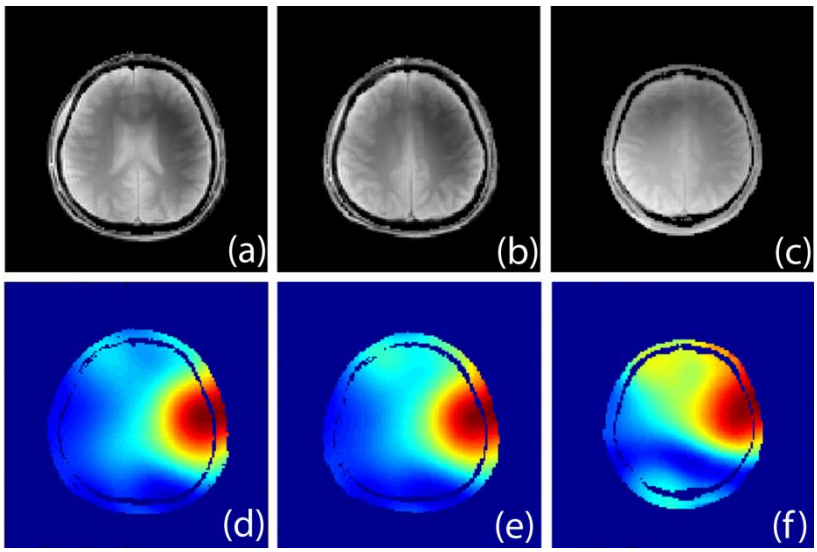

Figure 5-4. (a) and (b) are GRE images of two slices (12 mm separation) from subject A at position 1 (0°). (c) Image from subject B of the same slice position in (b) at position 1 (0°). Their corresponding sensitivity maps are shown in (d), (e) and (f) respectively.

The raw magnitude and phase maps of sensitivity derived from Eq. 5.1 are shown in Figures 5-5 (a) and (c), respectively. As predicted, coil sensitivity maps should be smooth with a small local gradient. However, in Figures 5-5 (b) and (d), we can see that the coil sensitivity maps had abrupt changes which were associated with high gradients (marked as red dots). Magnified regions in the red boxes show the singular values. In addition, the phase map in Figure 5-5 (c) also exhibits the phase wrapping at the skin/air and the skull/tissue interface.

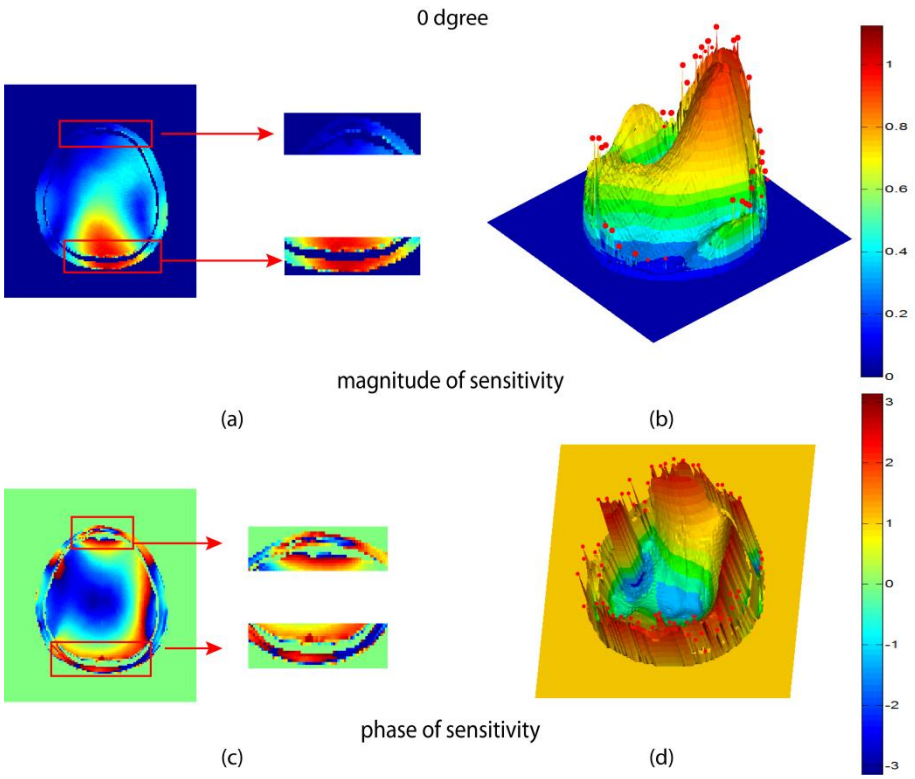

Figure 5-5. (a) and (c) are raw magnitude and phase plots of sensitivity. The areas in the red boxes are enlarged to show singular values. In (b) and (d), the red dots denote the singular values. Compared to adjacent areas, these spikes have higher gradients and are mostly seen at the interfaces. Besides singular values, undulating errors across the raw sensitivity profiles also need to be corrected for better registration efficiency.

With the developed multi-level fitting algorithm, both the magnitude and phase images were smooth with the singular values corrected. In Figure 5-6 (a), the signal voids were also extrapolated for image registration purposes. Compared to Figures 5-5 (b) and (d), the high gradient and undulating errors were corrected. Both the magnitude and phase plots of sensitivity were smooth and natural.

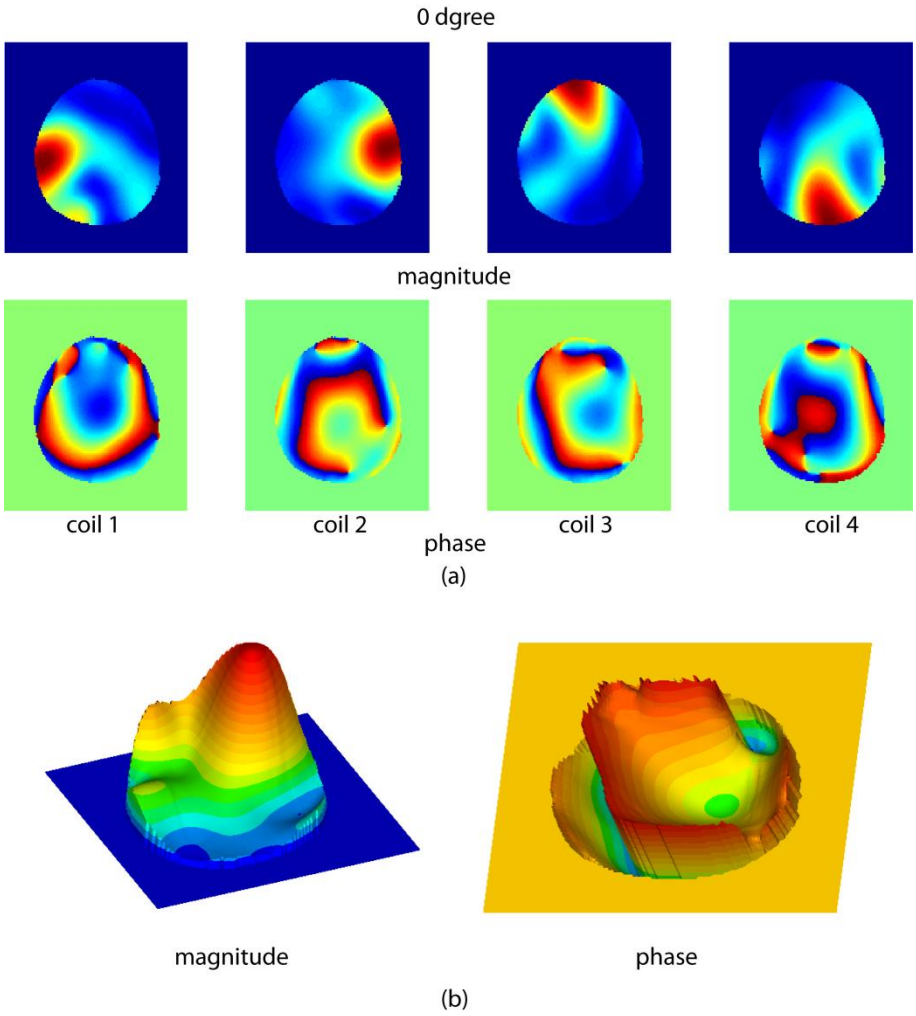

Figure 5-6. (a) magnitude (top row) and phase (bottom row) plots of refined sensitivity map at 0°. (b) 3D magnitude (top row) and phase (bottom row) plots of refined sensitivity map for single coil.

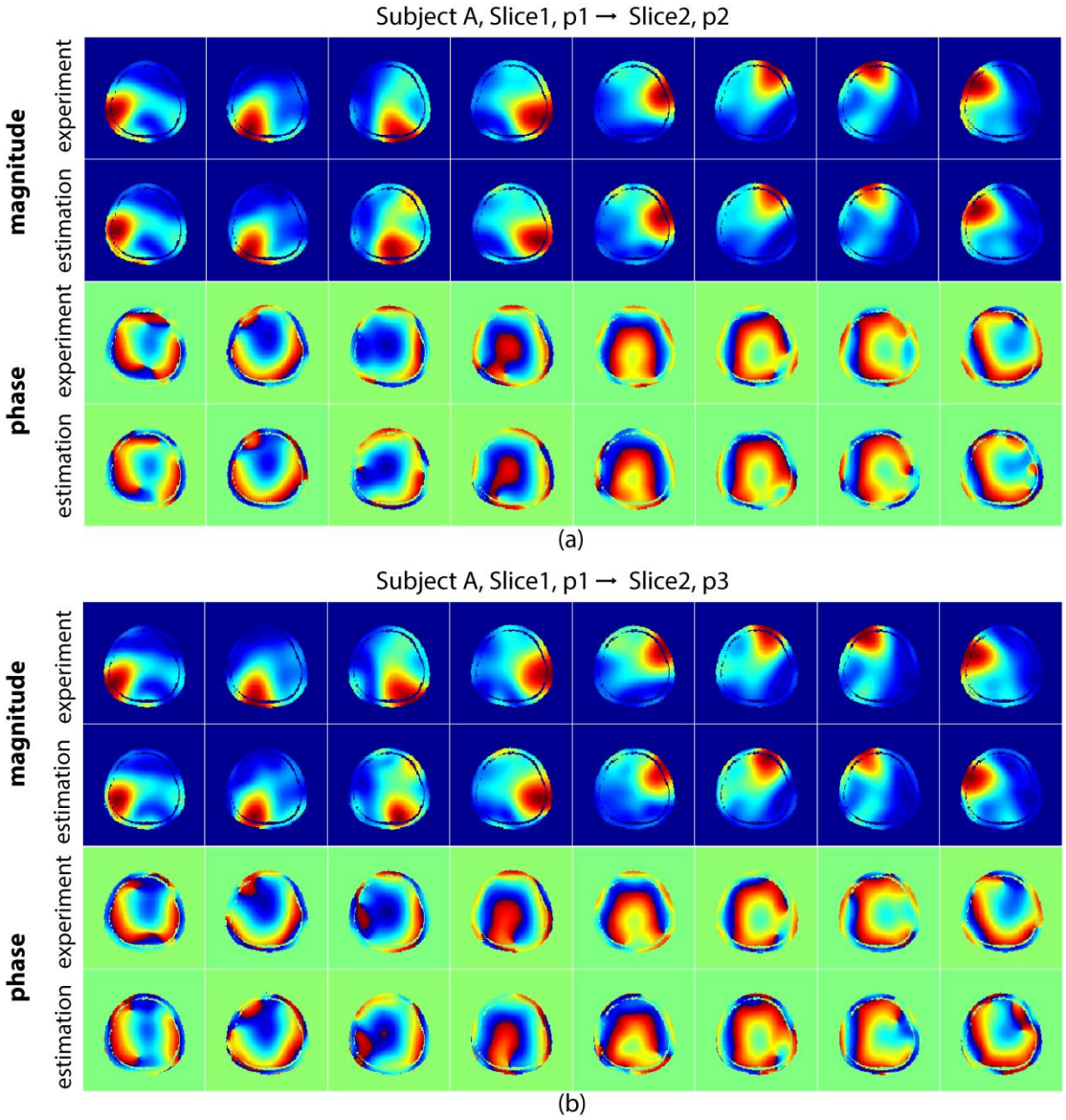

Figure 5-7. Intra-subject case: comparisons between experimentally measured and numerically estimated sensitivity maps at position 2 (p2 in (a)) and position 3 (p3 in (b)). First row, experimentally acquired magnitude maps at p2; second row, numerically estimated magnitude maps at p2; third row: experimentally acquired phase maps at p3; fourth row, numerically estimated phase maps at p3.

The experimentally acquired and numerically estimated sensitivity maps for the intra-subject case are compared in Figure 5-7. With a 10° angular displacement (p2 in Figure 5-7 (a)), the estimated magnitude maps in the second row of Figure 5-7 (a) were very similar to the measured sensitivity maps in the first row. Both the global features and the local details were estimated accurately. Estimated phase maps in the fourth row only showed small local variations compared to the acquired maps. Combining the magnitude and phase plots into a complex-numbered sensitivity, the root-mean-square error (RMSE) of the estimated sensitivity is 0.048. In Figure 5-7(b), the

angular displacement increased to 22° (position 3), which was also the largest displacement for the rotational sensitivity estimation under the current configuration. From the comparisons between the estimated and measured sensitivity maps in Figure 5-7(b), we note that the minor local discrepancies started to present, although the global features of sensitivity maps were well captured by the registration based algorithm. The RMSE increased to 0.068 at p3, which suggested a slightly decreased accuracy of estimating sensitivity with a larger angular displacement.

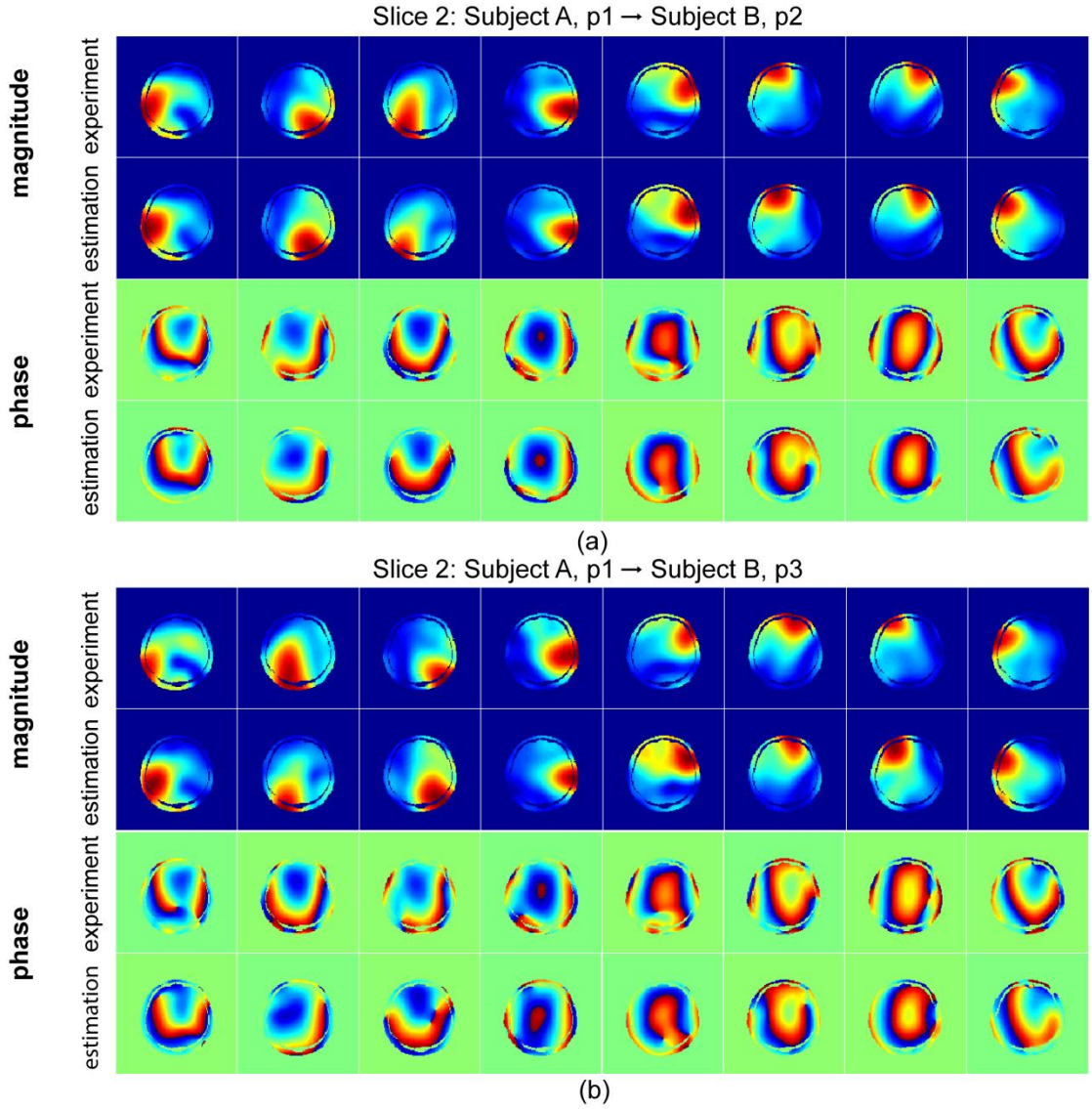

Figure 5-8. Inter-subject case: comparisons between experimentally measured and numerically estimated sensitivity maps at position 2 (p2 in (a)) and position 3 (p3 in (b)). First row, experimentally acquired magnitude maps at p2; second row, numerically estimated magnitude maps at p2; third row: experimentally acquired phase maps at p3; fourth row, numerically estimated phase maps at p3.

For the inter-subject case, the experimentally acquired and numerically estimated sensitivity maps at position 2 (p2 in Figure 5-8 (a)) and position 3 (p3 in Figure 5-8 (b)) are compared in Figure 5-8. The female subject had a noticeably smaller head than that of the male subject, therefore the sensitivity maps of two subjects have more differences compared to the intra-subject case. However, as shown in Figure 5-8 (a), the registration based algorithm was able to estimate the magnitude and phase maps of sensitivity accurately, both globally and locally. The RMSE was 0.054, which is slightly higher than that of the same position in the intra-subject case (RMSE = 0.048). Different from the intra-subject case, the RMSE reduced to 0.045 when the angle was then increased to 22° for position 3.

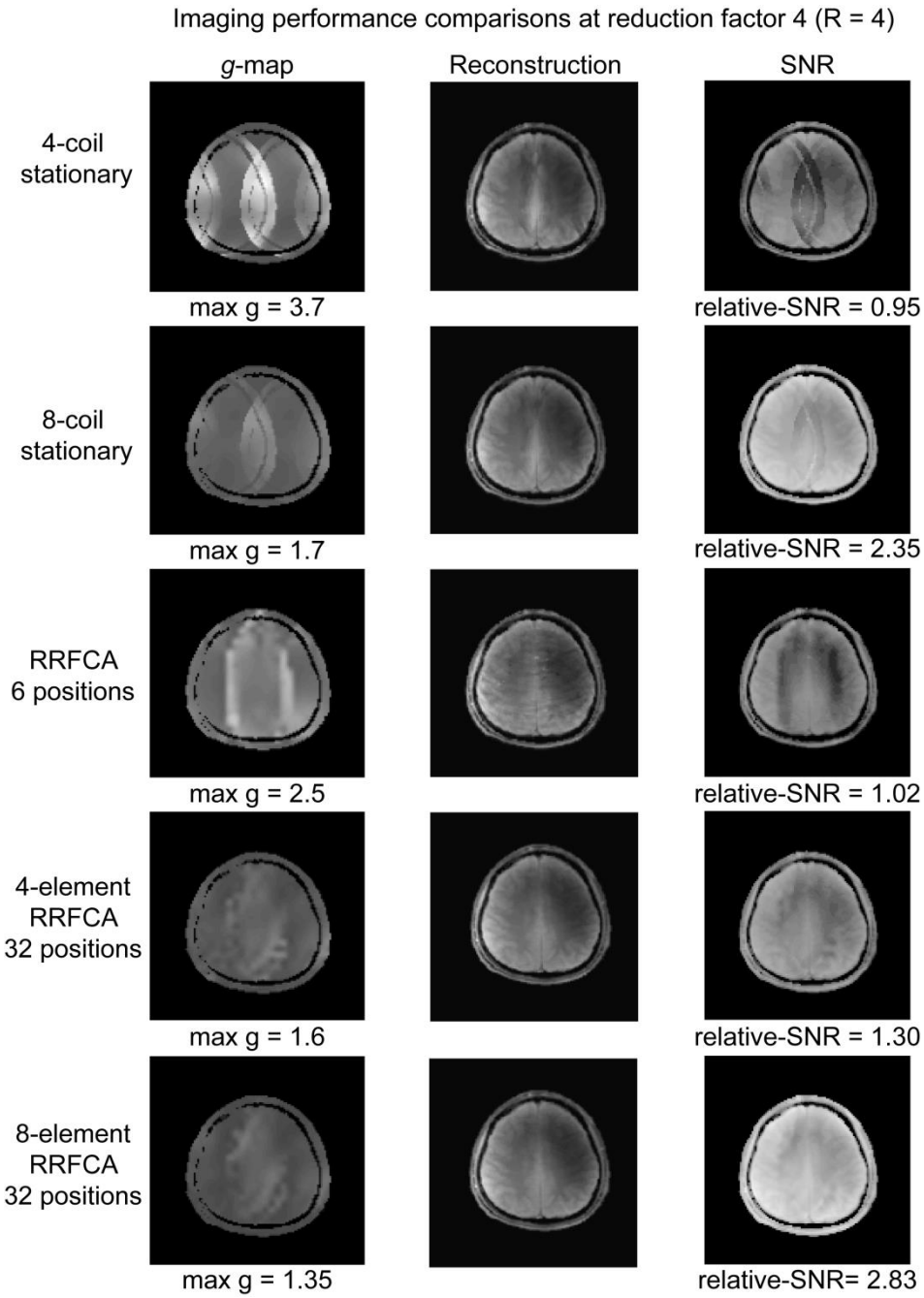

Figure 5-9. *g*-map, image reconstruction and relative-SNR map comparisons between 4- and 8-element stationary coil array (first and second rows), 4-element RRFCA visiting 6 positions (third rows), 4- and 8-element RRFCA visiting 32 positions (fourth and fifth rows). Left column, *g*-map comparisons; middle column, image reconstruction comparisons; right column, relative-SNR map comparisons. All SNR calculations were relative to that of a single rotating coil without undersampling (SNR = 1).

To illustrate the imaging acceleration and reconstruction ability of the RRFCA, the *g*-maps, reconstructed images and the SNR maps are shown in Figure 5-9 when the reduction factor was four (R = 4). The measurements with 4-element RRFCA sampled at two angular positions (position 1: 0˚+45˚) were used together to emulate an 8-element stationary coil array. In the first and second rows, results reconstructed from the experimental data for 4- and 8-element stationary arrays are shown, respectively. However, the coils of the RRFCA were naturally decoupled (−18dB S_{xy}), which would be more difficult to realise with an 8-element coil array in the same size. Therefore the max *g*-factor in the second row may be higher than 1.7 and the averaged relative-SNR may be lower than 2.35 in practice.

Since the SNR is hard to calculate accurately for ultra high field MRI, the SNR maps in this work were calculated relative to that of a single rotating coil without undersampling (R = 1). As we can see in Figure 5-9, with a high reduction factor (R = 4), the 4-element stationary coil array had a very high *g*-factor (max-*g* = 3.7) and a 0.95 averaged relative-SNR, which corresponded to a very noisy image with strong aliasing artifact. In contrast, under the rotating scheme of visiting 32 positions, the max *g*-factor (the fourth row) of 4-element RRFCA decreased to 1.6, which was comparable to the stationary coil array with twice as many elements (max *g* = 1.7) in the second row. The reconstructed image was better with lower RMSE and artifact power [169] (RMSE = 0.023, artifact power = 0.0082) compared to the 4-element stationary array (RMSE = 0.039, artifact power = 0.0231). However, fewer sensitivity profiles were available when visiting fewer angular positions, leading to higher *g*-factors and less capability in imaging acceleration. As shown in the third row, the maximum *g*-factor increased to 2.5 by only visiting six positions, and aliasing artifacts started to emerge in the reconstructed image. It is well known that the SNR is proportional to the square root of the number of channels [170, 171]. To provide a fair comparison, an 8-channel RRFCA was simulated by combining two sets of sensitivity profiles of the 4-channel RRFCA with a 45˚ rotation. The *g*-map, reconstructed images and the SNR maps were shown in the fifth row for such a coil array. Compared to the second row, we can see that with the same number of coils, not only was the relative-SNR of RRFCA (relative-SNR = 2.83) higher than that of the stationary array (relative-SNR = 2.35), but also the global SNR map was more uniform.

5.4. Discussion

5.4.1. The library data

The library data was used to provide sensitivity maps at all angular degrees, and the registration algorithm was used to bridge the discrepancy between the library and actual sensitivity maps. Theoretically, the library data can be either experimentally measured or numerically calculated. The experimentally acquired sensitivity maps may be more realistic, but obtaining 3-dimensional maps at multiple positions can be time-consuming. Acquisition speed may be further restricted due to the potential heating problems for ultra-high field MRI.

Commercially available electromagnetic (EM) software can be employed to calculate sensitivity maps and avoid such problems. With different algorithms, EM field distributions and related coil sensitivity can be calculated by solving Maxwell's equations. The Method of Moments (MOM) [144, 158, 172-175], used for calculating the EM field, is efficient for homogeneous loads, but it is not feasible to calculate heterogeneous dielectric loads due to the complexity of calculating the Green function [176]. The Finite Element Method (FEM) [177], discretising heterogeneous subjects into tetrahedral or hexahedral elements, is capable of representing complex heterogeneous subjects smoothly and providing a more accurate solution. However, the FEM requires very large computational resources for discretising the subjects and would have taken substantial amount of time to accurately evaluate B_1. The Finite-Difference Time-Domain (FDTD) method [78, 84, 178-182] has advantages over the FEM as it simplifies the discretisation into regular boxes, and the iterative solution saves on computational resources. Working in conjunction with a graphical processing unit (GPU), the calculation time can be dramatically reduced [183].

5.4.2. Transmit B_1^+

A signal intensity image is determined by both transmit profile B_1^+ and receive sensitivity B_1^- as illustrated in Eq. 5.7. At low field, the $\left|B_1^+\right|$ is uniform and thus can be excluded from the sensitivity encoding matrix in the SENSE reconstruction. However, to include the $\left|B_1^+\right|$ influence in the SENSE reconstruction at ultra-high fields, the actual sensitivity map in the encoding matrix should be in the form of Eq. 5.8 [77].

$$SI = M_0 \left|B_1^{-*}\right| \sin(V\gamma\tau \left|B_1^+\right|) \tag{5.7}$$

$$sensitivity_{actual} = \sin(V\gamma\tau \left|B_1^+\right|_{shim}) B_1^- \tag{5.8}$$

where γ is the gyromagnetic ratio and M_0 is proportional to the proton density distribution. τ and V denotes the RF pulse duration and coil driving voltage. The asterisk denotes the complex conjugate operation.

In this work, an 8-element coil array was manufactured and actively detuned to provide an unchanged B_1^+ in the course of rotation. However, the $\left|B_1^+\right|$ inevitably changed as the array rotated, which may have introduced a small bias into the reconstruction when this changing field was not considered in the encoding matrix. To further improve the sensitivity encoding ability of the RRFCA and faithfully reconstruct the image, it may be advantageous to adopt a composite sensitivity concept [168]. Our future work will involve the development of the sensitivity estimation algorithm for the RRFCA working in transceive mode.

5.4.3. SNR calculation

As an important metric to quantitatively evaluate image quality, the SNR calculation for MRI has been extensively studied [55, 78, 79, 171, 184]. At ultra-high field (>3T), the SNR can be expressed as [78, 135]:

$$SNR = \frac{V_{signal}}{V_{noise}} \propto \frac{B_0^2 \int\limits_{VOI} W \sin(V\gamma\tau\left|B_1^+\right|)\left|B_1^-\right| dv}{\sqrt{P_{sample}}} \tag{5.9}$$

where the integration is performed over the volume of interest (VOI) and W is a weighting factor related to tissue and sequence. The P_{sample} is the power dissipated in the sample, which is too complex to be efficiently calculated for rotating array coils at ultra-high fields. Thus the relative SNR was reported. In this work, to simplify the comparison, the P_{sample} for different arrays were considered the same [182], since transmission power remained approximately the same for different arrays.

In parallel imaging, the reduced k-space data are recovered by employing the coil sensitivity profiles. However, the noise is inevitably amplified in the reconstruction process, especially with a high reduction factor. The SNR calculation when employing parallel imaging algorithms, such as SENSE, can be calculated as below [11], provided that the channel number does not change:

$$\frac{SNR_{PI}}{SNR_{full}} = \frac{1}{g\sqrt{R}} \tag{5.10}$$

where g and R denotes the g-map and reduction factor, respectively. The SNR is also proportional to the square root of the number of channels [171, 185]. In order to provide a fair *SNR* comparison, we simulated the 8-channel RRFCA by combining data obtained with a 45˚ separation.

5.4.4. RRFCA structure and data sampling

5.4.4.1. Coil geometry

Using a large number of RF coils can increase the SNR and significantly accelerate the imaging process [38, 39, 116, 117]. However, placing a large number of coils in a constrained space will decrease the coil size, leading to a shallower B_1 penetration. Namely, the smaller coils receive less signal from the centre compared to larger coils. In addition, a coil array with higher density can increase the difficulty of decoupling. Coil coupling undermines the parallel imaging performance and reduces the *SNR*. By employing the rotating scheme, the RRFCA not only provides a large number of sensitivity profiles without additional RF channels, but also allows bigger coils to be used with less decoupling complexity.

5.4.4.2. Data sampling

The RRFCA is designed to sample one *k*-space line at each stepping position, and then move to the next angular position for the following sampling. In this preliminary *in vivo* study, the stepping angle was manually adjusted and a full *k*-space matrix was sampled at each angular position. The accelerated acquisition was numerically modelled by extracting and combining the corresponding *k*-space lines.

5.4.4.3. Rotation speed and acoustic noise

In this proof-of-concept work, the RRFCA was manually rotated to sample data at several angular positions in order to validate the proposed *in vivo* sensitivity estimation algorithm. In our previous works [40, 41], the rotating coil was pneumatically driven to achieve up to 870 rpm for human head imaging with negligible acoustic noise, compared with noise generated by the gradient system. For animal imaging, since the coil is much smaller, the rotation speed can easily exceed 10,000 rpm. Our recent experiments on a 9.4 T pre-clinical system have shown that the rotating coil can faithfully reconstruct the images at speeds of, or exceeding, 5500 rpm.

5.5. Conclusion

In this chapter, an *in vivo* rotational sensitivity estimation algorithm for the RRFCA was proposed and verified using human head imaging. Using registration techniques and library data, the algorithm was able to estimate sensitivity maps with arbitrary angular displacement. The estimated sensitivity maps were then fed into the rotating-SENSE algorithm to improve the imaging acceleration ability of the 4-element RRFCA. The 4-element RRFCA outperformed the 4-element

stationary array and was comparable to 8-element stationary PACs in terms of *g*-map and reconstruction quality. The 8-element RRFCA has been shown to significantly improve image quality compared to a stationary 8-element coil array. In the future, a sensitivity estimation algorithm for a transceive RRFCA with "composite sensitivity" (discussed in Chapter 4) will be developed. Additionally, an automatic rotation control system for the RRFCA will be developed by means of, for example, a non-magnetic piezo-electric or ceramic motor.

Chapter 6. A rapid and practical imaging scheme for a rotating RF coil with radial trajectory at 9.4 T

In the previous two chapters, with the developed rotating-SENSE and rotation-dependent *in vivo* sensitivity estimation algorithms, the 4-element RRFCA was able to reconstruct artefact-free images with only a quarter of scan duration compared with a typical full *k*-space acquisition. However, those custom-developed algorithms cannot reconstruct images on the host computer of the MRI system, which prevents the use of rotating technique for applications that require prompt image output.

In this chapter, we report the possibility of using radial sampling to develop a practical and rapid imaging strategy in the rotating framework. A large part of this chapter is modified from a manuscript which is ready to be submitted as a journal paper, "A rapid and practical imaging scheme for a rotating coil with radial trajectory at 9.4 T".

6.1. Introduction

In the previous works described in Chapters 4 and 5 [40, 41, 168, 186-188], MR image data were collected in Cartesian sampling trajectories with various sequences, such as, Fast-Low-Angle-SHot (FLASH) [189] or Gradient Recalled Echo (GRE). Motion artefacts would appear using direct inverse Fourier transform since the rotation of the RF coil violated the time-invariant requirement of Fourier transform. In order to obtain artefact-suppressed images, the rotating-SENSE algorithm was developed to iteratively reconstruct images with the information from rotation-dependent sensitivity maps. At low field, the rotation-dependent sensitivity maps can be estimated with extra scans and simple numerical operations. However, the unpredictable coil-tissue interactions at ultra-high fields complicate the *in vivo* sensitivity estimation, hence a hybrid numerical algorithm using registration techniques and a library database was developed to achieve an accurate *in vivo* sensitivity estimation [190]. In this algorithm, low-resolution scans and numerical calibrations are needed for sensitivity estimation, which will slightly extend the overall scan time. In addition, images can only be reconstructed off-line, since the custom-developed estimation and reconstruction algorithms are not built into the MRI system. An efficient and practical image reconstruction scheme is needed to apply the rotating technique for clinical use that requires fluent workflow.

The motion artefact caused by coil rotation is similar to those generated by patient motions, which raises the possibility of using a radial trajectory to mitigate motion artefacts. Although the mechanisms of artefact generation are different for coil rotation and subject motion, the unique

features of the radial sampling and rotating technique could be employed to suppress the motion artefacts generated by the rotating coil. Consequently, the image can be rapidly reconstructed on-line without measuring B_1^+ and B_1^- maps.

In this chapter, the feasibility of using radial sampling with a single-element rotating coil for rapid imaging was investigated. The mathematical analysis of such an imaging scheme is first undertaken, and then the numerical modelling and experimental validations are performed on various subjects using a 9.4 T preclinical system. The radial trajectory is further optimised in order to achieve optimal image reconstruction quality with algorithms that can reside on the host computer.

6.2. Methods and Materials

6.2.1. Radial sampling and its unique features

For completeness of discussion, the radial sampling scheme is briefly reviewed here. Radial sampling was firstly introduced in [103] in 1970s. But shortly afterwards, Cartesian trajectories became more popular thanks to its superior robustness against system imperfections. However, in recent years, radial sampling has been actively revisited for a wide range of applications such as dynamic imaging [129, 191-193] and noise suppression. As shown in Figure 6-1 (b) and (c), a radial trajectory samples *k*-space along radial spokes instead of horizontal lines as used in Cartesian sampling in Figure 6-1 (a). The spokes of a standard "full-length" radial trajectory (Figure 6-1 (b)) start and end at the high-frequency regions of the *k*-space; whereas, for the "half-length" radial trajectory, sampling starts from *k*-space centre as shown in Figure 6-1 (c). In this chapter, they are referred as "full-length" radial trajectory and "half-length" radial trajectory, respectively. Both spokes are used in this chapter with the same ultra-short TE (UTE) sequence to compare their effects against the image reconstruction. The angle between adjacent spokes is calculated as:

$$\Delta\phi = 2\pi / N_{spoke} \tag{6.1}$$

where N_{spoke} denotes the number of spokes, which is usually suggested to be [194]:

$$\begin{aligned} N_{spoke} &= \frac{\pi}{2} \cdot N \quad \text{full-length} \\ N_{spoke} &= \pi \cdot N \quad \text{half-length} \end{aligned} \tag{6.2}$$

where N denotes the image resolution.

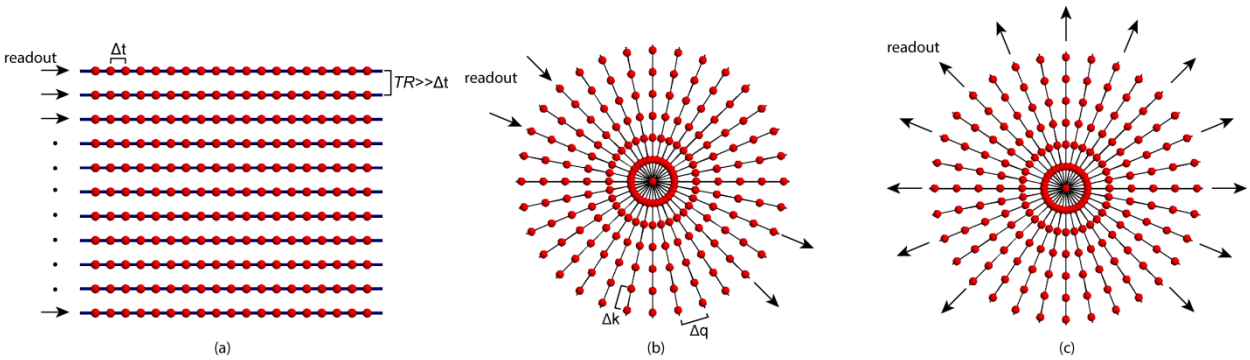

Figure 6-1 Three different sampling trajectories. (a). Cartesian trajectory where readout is along the frequency encoding direction. Δt denotes the time needed for a frequency encoding. TR denotes the repetition time. (b). A "full-length" radial trajectory. Δk denotes the Nyquist distance and Δq denotes the distance of the outmost rim (c). A "half-length" radial trajectory starts from the *k*-space centre.

Two unique features of radial trajectory sampling could be used to suppress motion artefacts, namely the varying readout directions and the oversampled central *k*-space [192, 193, 195]. As shown in Figure 6-1(a), Cartesian trajectory samples each phase-encoding (PE) line in the same readout direction. Therefore, the motion induced during a PE step (TR) is much larger than from within in a frequency encoding step (TR >> Δt), and thus motion artefacts constantly accumulate in the PE direction as shown in Figure 6-2 (b). However, with varying readout directions of the radial trajectories in Figs. 6-1(b) and (c), motion artefacts are "smeared" over the image to reduce the motion artefacts. More importantly, the oversampled central *k*-space is the primary feature used to suppress motion artefacts. As shown in Figure 6-1(b) and (c), the sampling distance (Δq) between two adjacent *k*-space points is smaller than the Nyquist distance (Δk) except in the outermost ring (Δq = Δk). In addition, Δq becomes much smaller towards the *k*-space centre. This feature offers the oversampling of the central *k*-space, providing an averaging effect that suppresses the motion artefacts as shown in Figure 6-2(c).

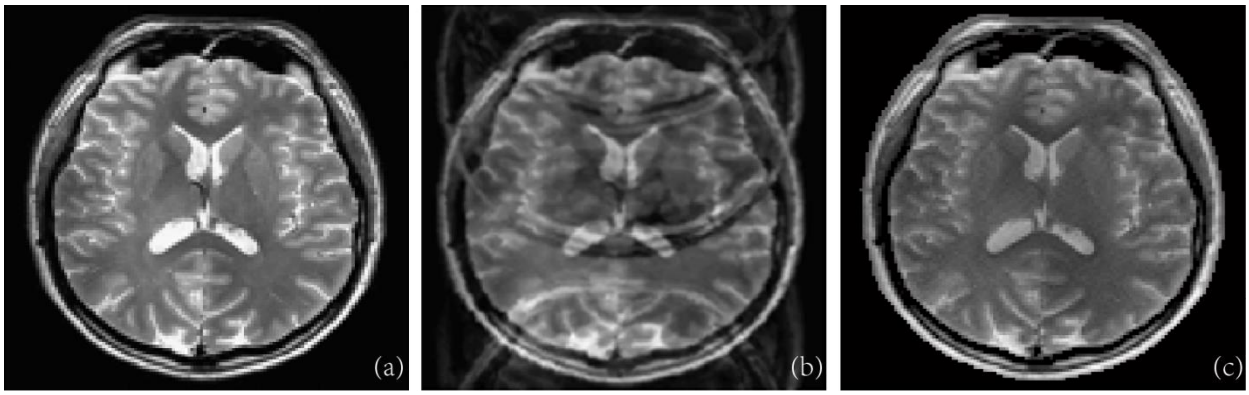

Figure 6-2 (a) Original image acquired without motion. (b) Image reconstructed from Cartesian sampling with simulated motions (c) Image reconstructed from radial sampling with simulated motions.

Data acquired via radial trajectory are not located on a regular grid, which prevents the use of fast inverse Fourier transform (IFFT) to reconstruct images. Two types of algorithms are usually used to reconstruct radial sampled data, namely the filtered back projection algorithm or the regridding algorithm [196]. As a more widely used algorithm, the procedure to reconstruct images using the regridding is explained here.

The goal of the regridding is to interpolate the data on the radial spokes to the Cartesian grid; and then the IFFT can be performed to reconstruct the image. The common steps of the regridding algorithms include density compensation, convolution and evaluation on a grid, 2D IFFT, and roll-off correction. Since the radially sampled data do not have a uniform sampling density, the density compensation is adopted before the interpolation. To derive a good interpolation without distortion in the image domain, an approximated sinc kernel is convoluted to the radial data. Usually, the Kaiser-Bessel kernel is used to interpolate with a reasonable window size, which is calculated as [197]:

$$G_{KB}(\mathrm{k}) = \begin{cases} \sqrt{\frac{1}{L} I_0(\beta\sqrt{1-(2\,\mathrm{k}/\,\mathrm{L})^2})} & |\mathrm{K}| \le \frac{1}{2} \\ 0 & |\mathrm{K}| \le \frac{1}{2} \end{cases} \tag{6.3}$$

where L denotes the desired kernel width, $I_0(k)$ is the zero-order modified Bessel function of the first kind, and β is the shape factor reported in [198]. However, convoluting to a finite kernel to the k-space will generate a signal modulation in the image domain, which is referred to as the roll-off effect. This effect can be compensated by dividing the image by the Fourier transform of the Kaiser-Bessel window, which is approximated as:

$$G_{KB}(\mathrm{x}) = \frac{\sin\sqrt{(\pi\,\mathrm{Lx})^2 - \beta^2}}{\sqrt{(\pi\,\mathrm{Lx})^2 - \beta^2}} \tag{6.4}$$

6.2.2. Characterising the averaging effect

In an image sampled using Cartesian trajectory, motion artefacts are caused by three types of motion, namely, subject motion, coil motion and hybrid motion that contain coil and subject motion. As illustrated above, artefacts resulting from these three types of motions can be reduced by the averaging effect of radial trajectories. However, the mechanisms of artefacts suppression have not

been mathematically analysed, especially for the coil motion induced artefacts. In this work, by characterising motion artefact and deliberately utilising averaging effect, motions artefacts caused by rotation could be mitigated by using a rotating coil with its varying sensitivity.

6.2.2.1. Subject motion

After regridding the radial data to the Cartesian grid, multiple acquisitions are located on the same grid positions that lead to the averaging effect as illustrated in Eq. 6.5:

$$\begin{aligned} b_k &= \frac{1}{s}\left(\sum_{\Psi=\Psi_1}^{\Psi_s} b_{k,\Psi}\right) = \frac{1}{s}\left(\sum_{\Psi=\Psi_1}^{\Psi_s}\sum_{r=1}^{n} e_{k,r}\cdot f_\Psi(\rho_r)\right) \\ &= \sum_{r=1}^{n} e_{k,r}\cdot\frac{1}{s}\left(\sum_{\Psi=\Psi_1}^{\Psi_s} f_\Psi(\rho_r)\right) = \sum_{r=1}^{n} e_{k,r}\cdot\overline{f(\rho_r)} \end{aligned} \tag{6.5}$$

where f_Ψ is the transfer function that describes the subject motion from the initial position. In this scenario, we assume that the image is acquired by using a volume coil with a uniform transmission profile. Therefore, the transmit sensitivity is not considered in the encoding process. Assume that, at a *k*-space grid *k*, acquisitions are repeated *s* times due to the oversampling and the corresponding transfer function varies from $f_{\Psi 1}$ to $f_{\Psi 2}$, the final value of grid b_k becomes the average of a series of samples, which are obtained by encoding the transformed voxels $f_\Psi(\rho_r)$ using the Fourier kernels $e_{k,r} = e^{-2\pi j(k,r)}$, where $k, r \in [1, N^2]$ and the image resolution is $N \times N$. As illustrated in the second row of Eq. 6.5, this is equivalent to first computing the average of the voxels in a series of movements before applying the Fourier kernel to the average. It is clear that the motions are not corrected or removed; instead, through the averaging of a series of voxels with movements, the coherent signals that represent the static voxels or average positions are enhanced, and those incoherent motions are weakened.

6.2.2.2. Motion of coil rotation

The rotating coil transmits and receives the signals while rotating about the subject. The coil sensitivity map varies with the coil angular position, and after regridding the radial data to the Cartesian grid, the *k*-space data on the grid *k* is characterised as:

$$\begin{aligned} b_k &= \frac{1}{s}\left(\sum_{\alpha=\alpha_1}^{\alpha_s} b_{k,\alpha}\right) = \frac{1}{s}\left(\sum_{\alpha=\alpha_1}^{\alpha_s}\sum_{r=1}^{n} e_{k,r}\cdot S_{\alpha,r}\cdot\rho_r\right) \\ &= \sum_{r=1}^{n} e_{k,r}\cdot\frac{1}{s}\left(\sum_{\alpha=\alpha_1}^{\alpha_s} S_{\alpha,r}\right)\cdot\rho_r = \sum_{r=1}^{n} e_{k,r}\cdot\overline{S_k}\cdot\rho_r \end{aligned} \tag{6.6}$$

Compared to Eq. 6.5, the encoding process with coil motion now has an extra weighting of receive sensitivity *S*, which varies with angular position (α from α_1 *to* α_s), for the repeated acquisitions at grid *k*. In transceive mode, the sensitivity *S* is a "composite sensitivity" that need to consider the transmit profile [199]. In the second row of Eq. 6.6, it can be seen that the averaging effect of the multiple acquisitions amounts to the averaging of the sensitivity profiles. Eventually, the averaged sensitivity $\overline{S_k}$ at point *k*, plays an important role in reducing artefacts as illustrated by rewriting Eq. 6.6 in matrix form below.

$$\underbrace{\begin{bmatrix} b_1 \\ b_2 \\ \vdots \\ b_k \\ \vdots \\ b_n \end{bmatrix}}_{k-space\ (N^2\times 1)} = \underbrace{\begin{bmatrix} e_{1,1}S_{\alpha_1,1} & e_{1,2}S_{\alpha_1,2} & \cdots & e_{1,r}S_{\alpha_1,r} & \cdots & e_{1,n}S_{\alpha_1,n} \\ e_{2,1}S_{\alpha_2,1} & e_{2,2}S_{\alpha_2,2} & \cdots & e_{2,r}S_{\alpha_2,r} & \cdots & e_{2,n}S_{\alpha_2,n} \\ \vdots & \vdots & \ddots & \vdots & \vdots & \vdots \\ e_{k,1}S_{\alpha_i,1} & e_{k,2}S_{\alpha_i,2} & \cdots & e_{k,r}S_{\alpha_i,r} & \cdots & e_{k,n}S_{\alpha_i,n} \\ \vdots & \vdots & \cdots & \vdots & \ddots & \vdots \\ e_{n,1}S_{\alpha_n,1} & e_{n,2}S_{\alpha_n,2} & \cdots & e_{n,r}S_{\alpha_n,r} & \cdots & e_{n,n}S_{\alpha_n,n} \end{bmatrix}}_{Encoding\ matrix\ E=F\cdot S\ (N^2\times N^2)} \underbrace{\begin{bmatrix} \rho_1 \\ \rho_2 \\ \vdots \\ \rho_r \\ \vdots \\ \rho_n \end{bmatrix}}_{proton\ density\ N^2\times 1} \tag{6.7}$$

In Eq. 6.7, the *k*-space data b_k is generated by multiplying the voxels with the encoding matrix *E*, which is the element-wise product of the standard Fourier weighting $e_{k,r}$ and sensitivity weighting $S_{\alpha,r}$. For a stationary coil, the sensitivity weightings of each row in the matrix *E* are identical ($\alpha_1 = \alpha_2 = \ldots \alpha_n$). Therefore, the sensitivity weightings in matrix *E* can be extracted and form a diagonal matrix *diag(S).* Thus, an image weighted by sensitivity can be obtained by applying IFFT (F^{-1}) to the *k*-space data as:

$$\begin{bmatrix} m_1 \\ m_1 \\ \vdots \\ m_r \\ \vdots \\ m_n \end{bmatrix} = F^{-1}F \begin{bmatrix} S_1 & 0 & \cdots & 0 & \cdots & 0 \\ 0 & S_1 & \cdots & 0 & \cdots & 0 \\ \vdots & \vdots & \ddots & \vdots & \vdots & \vdots \\ 0 & 0 & \cdots & S_r & \cdots & 0 \\ \vdots & \vdots & \cdots & \vdots & \ddots & \vdots \\ 0 & 0 & \cdots & 0 & \cdots & S_n \end{bmatrix} \begin{bmatrix} \rho_1 \\ \rho_2 \\ \vdots \\ \rho_r \\ \vdots \\ \rho_n \end{bmatrix} = \begin{bmatrix} S_1\rho_1 \\ S_2\rho_2 \\ \vdots \\ S_r\rho_r \\ \vdots \\ S_n\rho_n \end{bmatrix} \tag{6.8}$$

where the element in decoding matrix F^{-1} is $e_{k,r}^{-1} = e^{2\pi j(k,r)}$

However, if the data are sampled using a rotating coil in Cartesian trajectory, the sensitivity weightings vary from row to row in matrix *E*, therefore separating *S* from matrix *E* becomes infeasible. Compared to Eq. 6.8 for a stationary coil, the elements of encoding matrix in Eq. 6.9 includes not only sensitivity weightings, but also Fourier kernel $e_{i,r}$. Consequently, applying F^{-1} to

the encoding matrix E will yield a more complex hybrid sensitivity matrix S_h, in which each element is calculated as a summation of the product of the sensitivity weightings, Fourier kernel and inverse Fourier kernel of different angular positions α_i ($\alpha_1 \sim \alpha_n$) at the corresponding voxels r. Each voxel of the reconstructed image is the superposition of all voxels with a variety of sensitivity values, leading to fold-over artefacts.

$$\underset{\substack{\textit{image}\\(N^2\times 1)}}{\begin{bmatrix} m_1 \\ m_2 \\ \vdots \\ m_r \\ \vdots \\ m_n \end{bmatrix}} = F^{-1} \underbrace{\begin{bmatrix} e_{1,1}S_{\alpha_1,1} & e_{1,2}S_{\alpha_1,2} & \cdots & e_{1,r}S_{\alpha_1,\mathrm{r}} & \cdots & e_{1,n}S_{\alpha_1,n} \\ e_{2,1}S_{\alpha_2,1} & e_{2,2}S_{\alpha_2,2} & \cdots & e_{2,r}S_{\alpha_2,\mathrm{r}} & \cdots & e_{2,n}S_{\alpha_2,n} \\ \vdots & \vdots & \ddots & \vdots & \vdots & \vdots \\ e_{k,1}S_{\alpha_i,1} & e_{k,2}S_{\alpha_i,2} & \cdots & e_{k,r}S_{\alpha_i,\mathrm{r}} & \cdots & e_{k,n}S_{\alpha_i,n} \\ \vdots & \vdots & \cdots & \vdots & \ddots & \vdots \\ e_{n,1}S_{\alpha_n,1} & e_{n,2}S_{\alpha_n,2} & \cdots & e_{n,r}S_{\alpha_n,\mathrm{r}} & \cdots & e_{n,n}S_{\alpha_n,n} \end{bmatrix}}_{\substack{\textit{Encoding matrix } E=F\cdot S\\(N^2\times N^2)}} \underset{\substack{\textit{proton density}\\N^2\times 1}}{\begin{bmatrix} \rho_1 \\ \rho_2 \\ \vdots \\ \rho_r \\ \vdots \\ \rho_n \end{bmatrix}}$$

$$= \underbrace{\begin{bmatrix} \sum_{i=1}^{n} e_{1,i}^{-1}e_{\mathrm{i},1}S_{\alpha_i,1} & \sum_{i=1}^{n} e_{1,i}^{-1}e_{\mathrm{i},2}S_{\alpha_i,2} & \cdots & \sum_{i=1}^{n} e_{1,i}^{-1}e_{\mathrm{i},\mathrm{r}}S_{\alpha_i,\mathrm{r}} & \cdots & \sum_{i=1}^{n} e_{1,i}^{-1}e_{\mathrm{i},\mathrm{n}}S_{\alpha_i,\mathrm{n}} \\ \sum_{i=1}^{n} e_{2,i}^{-1}e_{\mathrm{i},1}S_{\alpha_i,1} & \sum_{i=1}^{n} e_{2,i}^{-1}e_{\mathrm{i},2}S_{\alpha_i,2} & \cdots & \sum_{i=1}^{n} e_{2,i}^{-1}e_{\mathrm{i},\mathrm{r}}S_{\alpha_i,\mathrm{r}} & \cdots & \sum_{i=1}^{n} e_{2,i}^{-1}e_{\mathrm{i},\mathrm{n}}S_{\alpha_i,\mathrm{n}} \\ \vdots & \vdots & \ddots & \vdots & \vdots & \vdots \\ \sum_{i=1}^{n} e_{\mathrm{r},i}^{-1}e_{\mathrm{i},1}S_{\alpha_i,1} & \sum_{i=1}^{n} e_{\mathrm{r},i}^{-1}e_{\mathrm{i},2}S_{\alpha_i,2} & \cdots & \sum_{i=1}^{n} e_{r,i}^{-1}e_{\mathrm{i},r}S_{\alpha_i,r} & \cdots & \sum_{i=1}^{n} e_{\mathrm{r},i}^{-1}e_{\mathrm{i},\mathrm{n}}S_{\alpha_i,\mathrm{n}} \\ \vdots & \vdots & \cdots & \vdots & \ddots & \vdots \\ \sum_{i=1}^{n} e_{\mathrm{n},i}^{-1}e_{\mathrm{i},1}S_{\alpha_i,1} & \sum_{i=1}^{n} e_{\mathrm{n},i}^{-1}e_{\mathrm{i},2}S_{\alpha_i,2} & \cdots & \sum_{i=1}^{n} e_{\mathrm{n},i}^{-1}e_{\mathrm{i},\mathrm{r}}S_{\alpha_i,\mathrm{r}} & \cdots & \sum_{i=1}^{n} e_{n,i}^{-1}e_{\mathrm{i},n}S_{\alpha_i,n} \end{bmatrix}}_{\textit{hybrid sensitivity matrix } S_h} \begin{bmatrix} \rho_1 \\ \rho_2 \\ \vdots \\ \rho_r \\ \vdots \\ \rho_n \end{bmatrix} \tag{6.9}$$

However, according to Eq. 6.6, if the equivalent sensitivity $\overline{S_k}$ can be modulated into a uniform one, sensitivity encodings can be extracted out of the summation operation in the Eq. 6.9, and motion artifacts can be suppressed. Given that the non-oversampled outer k-space region has a much lower energy, the hybrid sensitivity matrix S_h could be approximated to a diagonal matrix by adjusting the rotation speed and the repetition time (TR).

The combination of the sampling position α and the times of the repeated acquisitions (oversampling rate) is critical to the uniformity of the equivalent sensitivity $\overline{S_k}$. The sampling positions are dependent on the angular increment θ, which is described as the angular position difference ($\alpha_2 - \alpha_1$) of the coil when two adjacent spokes are sampled. The best uniformity of the equivalent sensitivity should be achieved with the appropriate angular increment as $\theta \approx 360^\circ / \textit{oversampling rate}$. In addition, the uniform sensitivity transfers the single-element

rotating coil into a static volume coil without local intensity biases, which are commonly seen in a stationary surface coil.

The equivalent sensitivity maps with different oversampling rates are shown in Figure 6-3. When the oversampling rate is increased to three, both the magnitude and the phase of the sensitivity uniformity can be dramatically improved, compared with the first and second columns. The uniformity of the sensitivity is further improved with six and eight oversamplings. To maximise the uniformity of the equivalent sensitivity $\overline{S_k}$, the rotation speed and repetition time (TR) should be adjusted accordingly to acquire suitable angular positions that are uniformly distributed around the subject. The angular increment θ is determined by the rotation speed and repetition time (TR) as:

$$\theta = \mathrm{mod}(360^\circ, speed(rpm)/60s/1000ms \cdot 360^\circ \cdot TR) \tag{6.10}$$

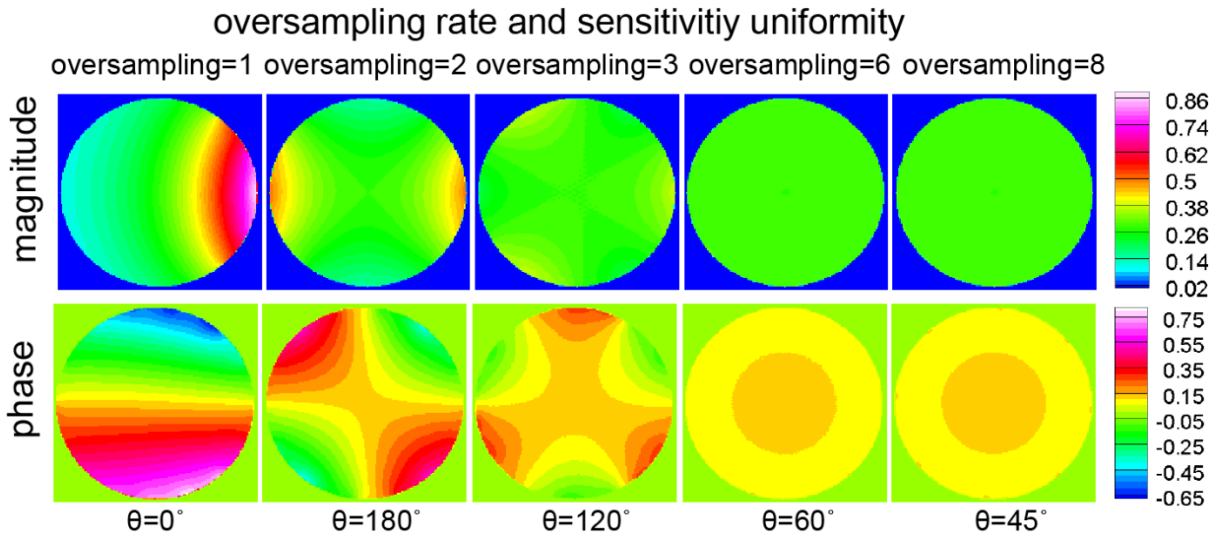

Figure 6-3. The magnitude and phase plots of the averaged sensitivity (equivalent sensitivity $\overline{S_k}$) with various oversamplings.

6.2.3. Prototyping

6.2.3.1. Simulation

The numerical model was constructed first to investigate the averaging effect for a mouse brain and a Shepp-Logan phantom. These two images were chosen because they have very different *k*-space features. The mouse brain has a large amount of detailed tissue information and an ambiguous interface in the image domain, which correlates to a larger low-frequency *k*-space central region and less high-frequency information. In another words, the central *k*-space is dominant. The Shepp-

Logan phantom however, has distinct interfaces; therefore both high and low frequency information are of importance.

The simulation of the RF coil was performed on the electromagnetic simulation platform FEKO (EMSS, SA). The numerical coil model had the exact geometry as the coil used in the experiments (to be discussed in the following section). Matlab (Massachusetts, USA) was used to calculate the circularly polarised magnetic field and simulate the data collection process in Cartesian and radial trajectories with a rotating coil. The elliptical magnetic field can be decomposed into circularly polarised components which are normally referred to as the transmit profile and receive profile [53]:

$$B_1^+ = \frac{\left(B_x + iB_y\right)}{2} \tag{6.11a}$$

$$B_1^- = \frac{(B_x - iB_y)^*}{2} \tag{6.11b}$$

where B_1^+, B_1^-, B_x and B_y denote the position dependent complex magnetic field quantities; B_x and B_y are the vector components calculated in FEKO, i is the imaginary unit, and * asterisk indicates the complex conjugation. In this application at 9.4 T, since the size of the phantom is much smaller than the RF wavelength and there is only one coil element, the B_1^+ and B_1^- are less affected by the interference and other elements. The B_x and B_y are numerically rotated by the Matlab function "*imrotate*" to generate the corresponding *k*-space data.

"Half-length" radial trajectory is used in the simulation and the sampling density along the *k*-space centre is plotted in Figure 6-4. For a 256×256 image, the spoke number is $256 \cdot \pi \approx 804$. The *k*-space centre is sampled 804 times and the points in the extended central region are oversampled at least 20 times. The smallest oversampling rate (>1) is three, which corresponds to a 120˚angular increment to produce a uniform sensitivity. Another very small angle, 3˚, that needs much more oversampling to generate a uniform sensitivity was chosen as for comparison purpose.

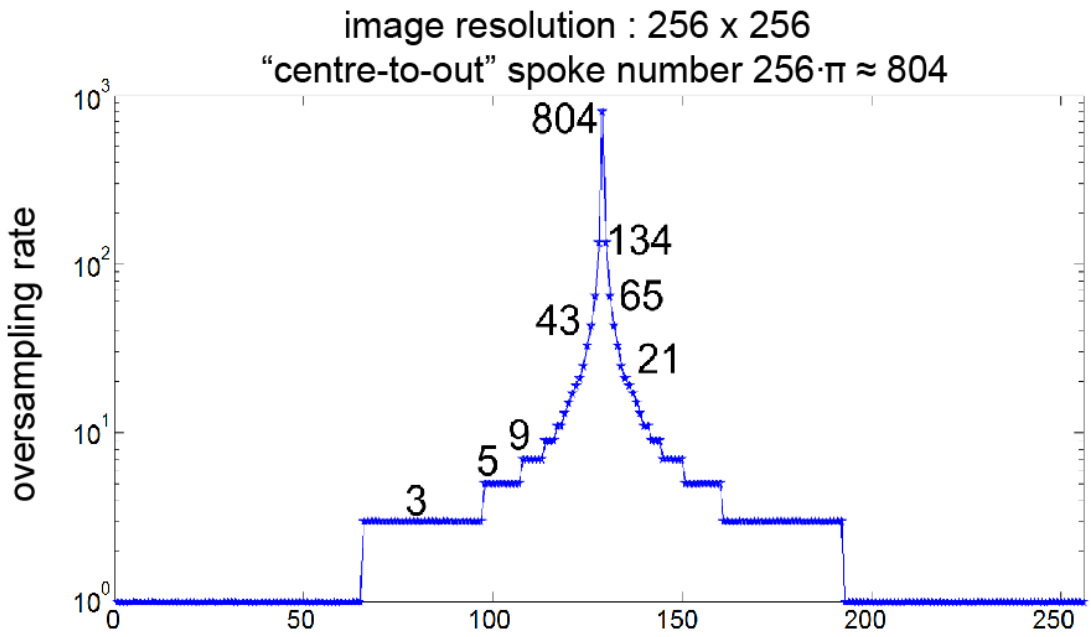

Figure 6-4. The sampling density along the central PE line. ($PE_{central}$ = N/2)

6.2.3.2. Experiment setup

The experiments were performed on a Bruker 9.4 Bruker Biospin MRI preclinical scanner (Ettlingen, Germany) with a single channel RRFC in transceive mode. The rotating coil was driven pneumatically with compressed air. The rotating coil and the disassembled rotating structure are shown in Figure 6-5. (B) and (D) are the wires to connect the optical sensor and gating signal to a USB data logger. By using the data stored in the USB data logger, the rotation speed was calculated and the speed variation was found to be less than 5% throughout the experiment. The RF element (E) with an open angle of 60 °was attached to a rotatable coil former. All the holes of the pneumatic actuator (G) have the same angle of inclination, by which the coil will rotate in one direction with incoming compressed air. A LEGO phantom, a homogeneous phantom and a tomato were used for imaging at different rotation speeds. The “half-length” ultra-short TE (UTE) sequence [200-203] (TE/TR = 0.3481ms/30ms) and the fast low angle shot (FLASH) sequence (TE/TR = 4ms/30ms) were used with radial and Cartesian trajectories, respectively. Data collected using both trajectories were reconstructed by the algorithms available with the scanner software (Paravision 6.0).

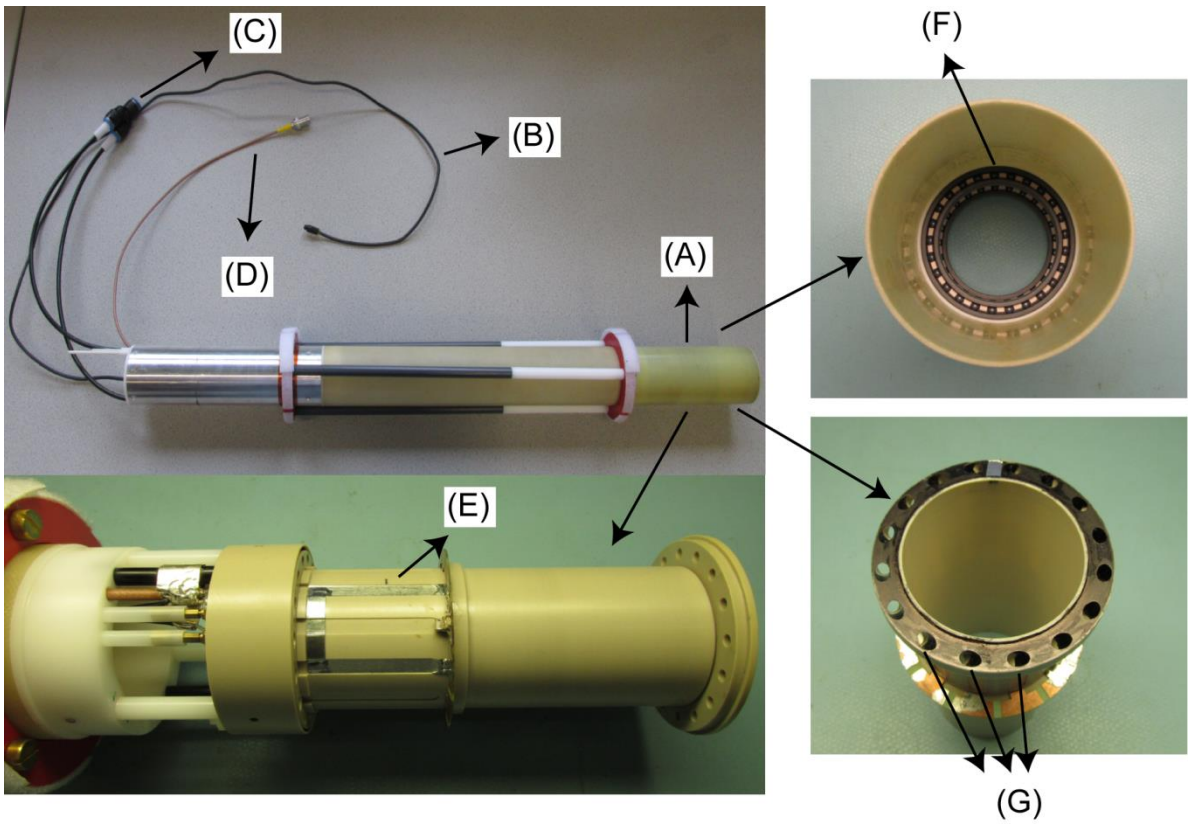

Figure 6-5. The mechanical structure of the rotating coil. (A) is rotating system and includes the pneumatic driving component attached a RF coil. (B) and (D) are the optical sensor connection wire and gating signal connection wire, respectively. (C) is the port connects the compressed air to the actuation system. (E) is the rotating coil that is attached to a rotatable former. (F) is the ceramic bearing of the rotating system. And (G) is the pneumatic actuator which is connected to the rotating coil former. All holes have the same angle of inclination, thus when the compressed air enters, the structure rotates in one direction.

6.3.Results

6.3.1. Simulation results

The images reconstructed from the simulated data in Cartesian and radial trajectories of RRFC are shown in Figure 6-6. Images from (a) to (h) were reconstructed from the simulated Cartesian sampling, and images from (i) to (p) were reconstructed from the simulated radial sampling. The angular increments were chosen as 3 °and 120 °to demonstrate its impact on the reconstruction for both Cartesian sampling and radial sampling.

A comparison of the images reconstructed from radial trajectory sampling against those from Cartesian trajectory revealed two clear differences. First, the motion artefacts of the reconstructed images are more successfully suppressed using radial trajectory than Cartesian trajectory, with both

3 ºand 120 ºangular increments. Second, for the radial sampling, the angular increment is critical for the quality of the image reconstruction. It is clear that by satisfying Eq. 6.10, uniform sensitivity can produce the best image reconstruction as shown in Figure 6-6 (j) with less than 5% error for the mouse brain image. Even when the error was amplified two times (Figure 6-6(l)), only few minor streak artefacts are visible. In contrast, with an angular increment as small as 3 º, the reconstructed images have more artefacts (see Figure 6-6 (i)), especially at the interface. This resulted from the non-uniform equivalent sensitivity in the outer *k*-space region, which primarily contains the high frequency information that related to the interface. With a Shepp-Logan phantom that contains more high-frequency information, the artefacts resulting from this inefficient averaging effect (3 º) were more obvious as shown in Figure 6-6 (m). However, these visible streak artefacts can be better suppressed with a 120 ºangular increment as shown in Figure 6-6 (n).

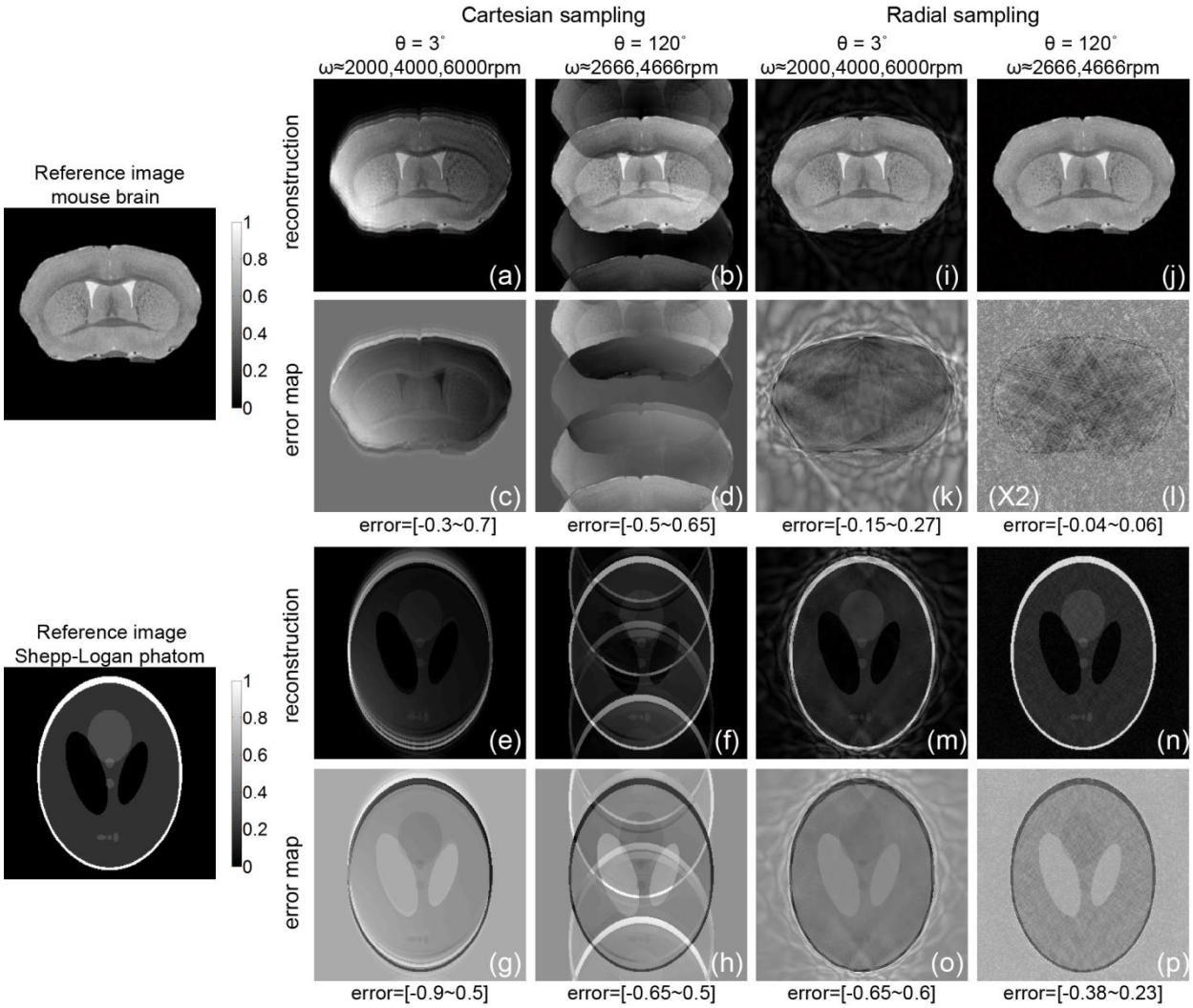

Figure 6-6. The simulated image reconstruction and error maps of a mouse brain and a standard Shepp-Logan phantom with radial sampling. The angular increments and corresponding rotation speeds are listed at the top of each column. The error range for each is listed at the bottom of the

error maps. (a)~(h), images reconstructed from the simulated Cartesian sampling. (i)~(p), images reconstructed from the simulated radial sampling.

6.3.2. Experiment results

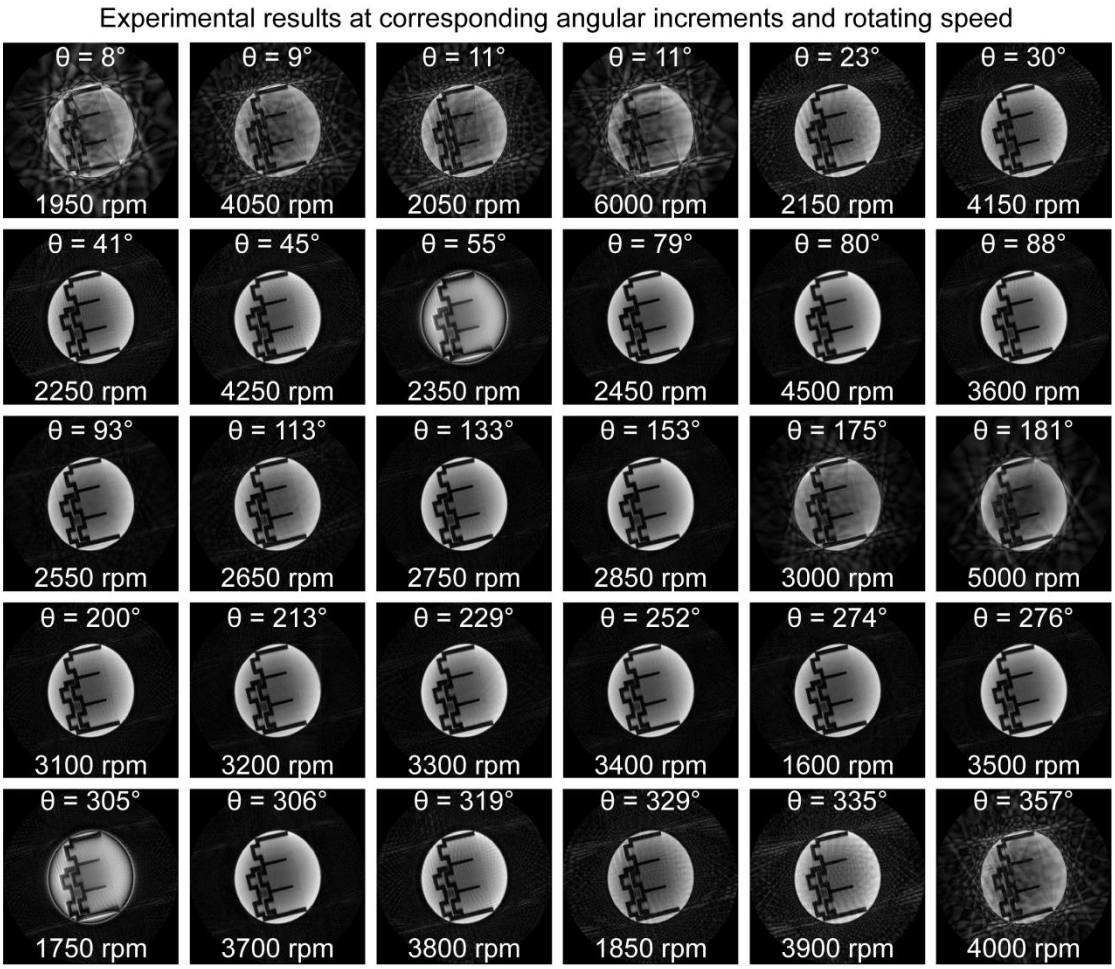

Figure 6-7 Experiment results of the reconstructed LEGO images at different angular increments θ (averaged θ from actual measured data) and rotation speeds.

A LEGO phantom was used to acquire images at different rotation speeds in the experiment. The results are listed in ascending order of the angular increment θ to reveal the relationship between the θ and the image quality. At the top and the bottom of each image in Figure 6-7, the average value of the measured angular increment θ and the pre-set rotation speed are listed respectively. There is a clear trend that the quality of the image varies with the θ. We can easily detect several types of artefacts that contaminate the images, including the streak artefacts, image distortions and dark rims. According to image quality, we classified the images in Figure 6-7 into 4 grades and plotted the corresponding θ in Figure 6-8. The image quality tends to improve with θ from 0˚ in both directions, except the 180˚ region. A 180˚ angular increment θ is inefficient to provide a uniform sensitivity as shown in Figure 6-3.

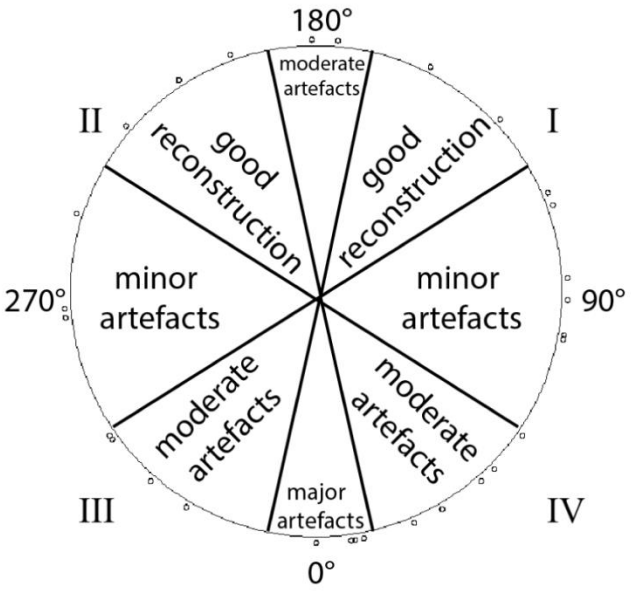

Figure 6-8. The image quality was classified into four grades with the corresponding angular increment. The small circles are the angular increments used in the experiment. Major artefacts: image distortion, intensity bias, serious streak artefacts or bright rim. Moderate artefacts: clear streak artefacts inside the FOV, but details were not seriously distorted. Minor artefacts: very light streak artefacts, details were well reconstructed. Good: images without detectable artefacts.

In order to better quantify the image quality and reveal its relationship to rotation speed (angular position), the artefact power [169] of each reconstructed image at the corresponding rotation speed was calculated and plotted in Figure 6-9. We can easily detect several rotation speeds that correspond to very high artefact powers, marked as red and green arrows in Figure 6-9. At rotation speeds of 1750 rpm and 2350 rpm, the primary artefacts are the dark rims, while the details are well reconstructed. It is noticeable that the image quality is particularly worsened at rotation speeds of about 2000 rpm, 4000 rpm and 6000 rpm. At those speeds, the rotating coil travelled approximately one revolution (360˚), two revolution (720˚) and three revolutions (1080˚) within a TR of 30 ms. The variation in rotation speed generated corresponding angular increments as 3˚, 8˚ and 11˚. This correlates well with the theory and simulation results that with a small angular increment, the averaging effect was less effective and then the appearance of artefacts are more serious, especially at the interfaces.

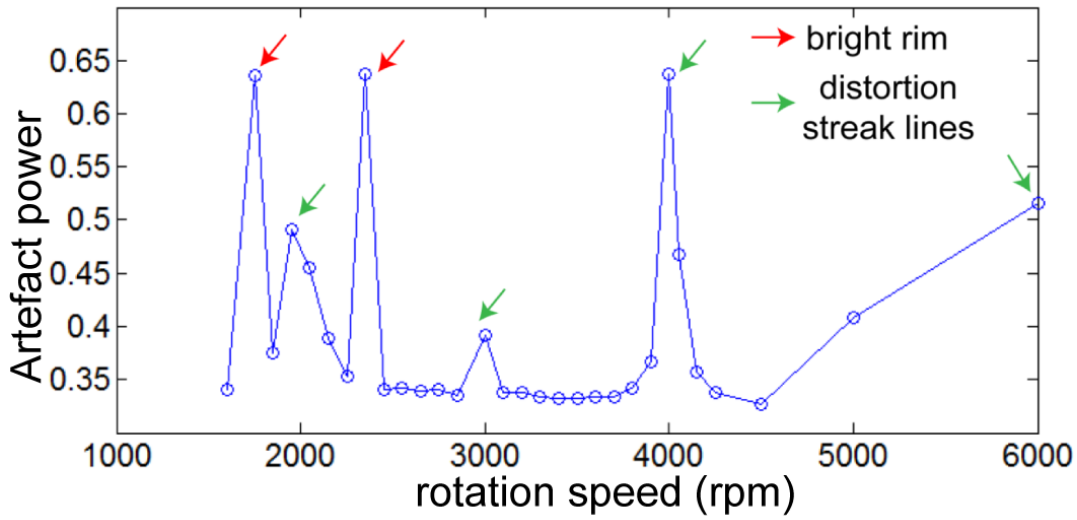

Figure 6-9. The artefact power of the reconstructed image at corresponding rotation speed.

The worst and the best reconstructions are chosen to be compared and analysed, as shown in Figs. 6-10 (a) and (b). It is clear that the image in Figure 6-10 (a) not only has a large number of streak artefacts and distorted details, but also biased intensity. The latter artefact implies unequal-distanced sampling in angular direction shown in Figure 6-10 (c), which is calculated using an optical sensor. With an average increment angle of -3˚, a 360˚ sampling should be achieved by 120 spokes; and for with a full *k*-space sampling of 804 spokes, the same sampling angular positions (regions) should be revisited at least 6 times. However, in Figure 6-10 (c), we only see two complete lines from 0˚ to 360˚, which suggests some angular regions are visited more than others. In addition, red arrows indicate the angular regions that are sampled more often. A good image reconstruction without intensity bias requires equidistant sampling in angular direction. This is demonstrated in Figure 6-10 (f) as a straight line in the ascending order of sampling positions.

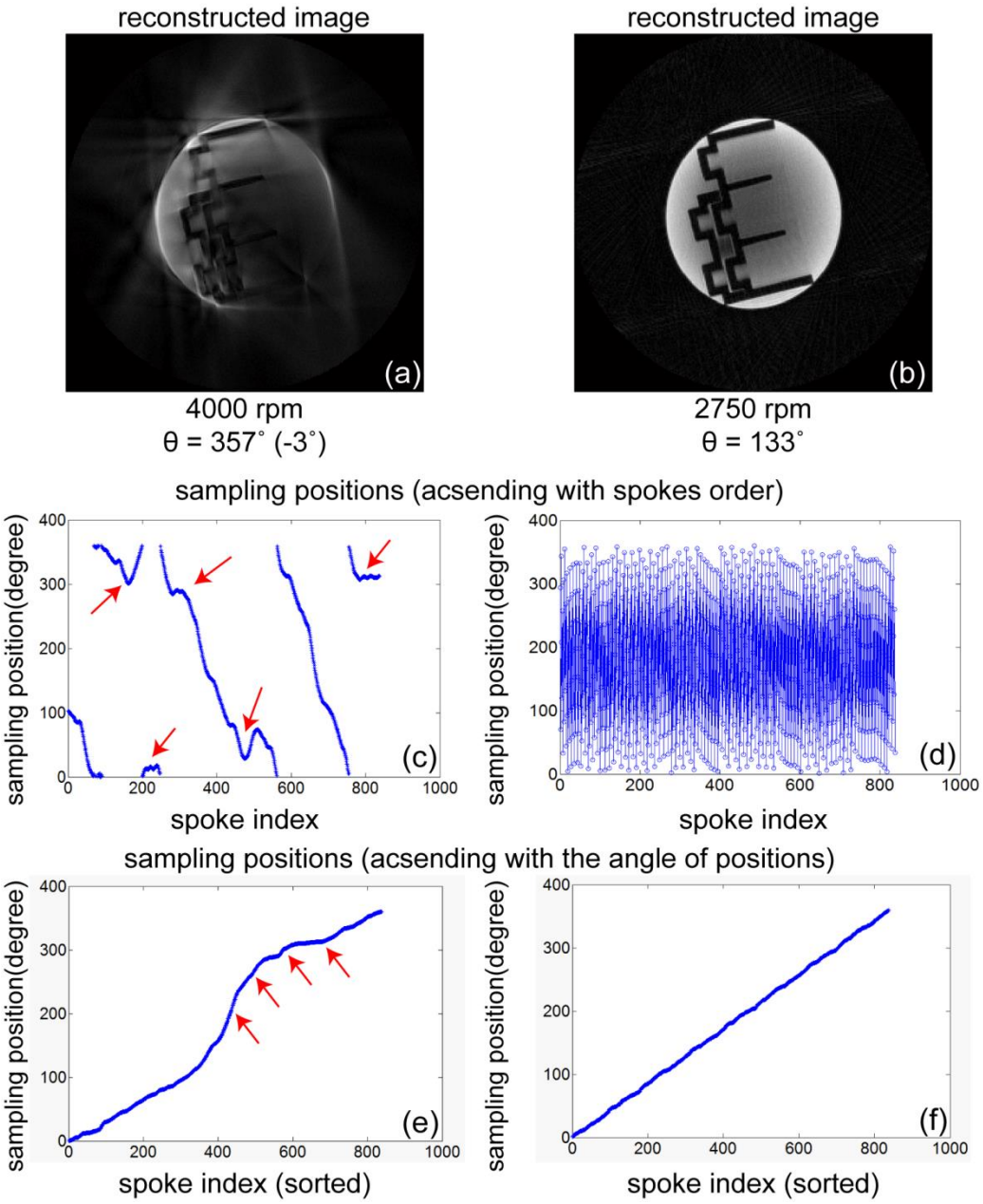

Figure 6-10. Comparison of worst (a) and best (b) scenarios of reconstructed images and sampling angular positions of corresponding spokes. (c) and (d) are the sampling positions at corresponding spokes order (ascending spoke order). (e) and (f) are the sorted sampling positions regardless of spoke order (ascending with sampling positions).

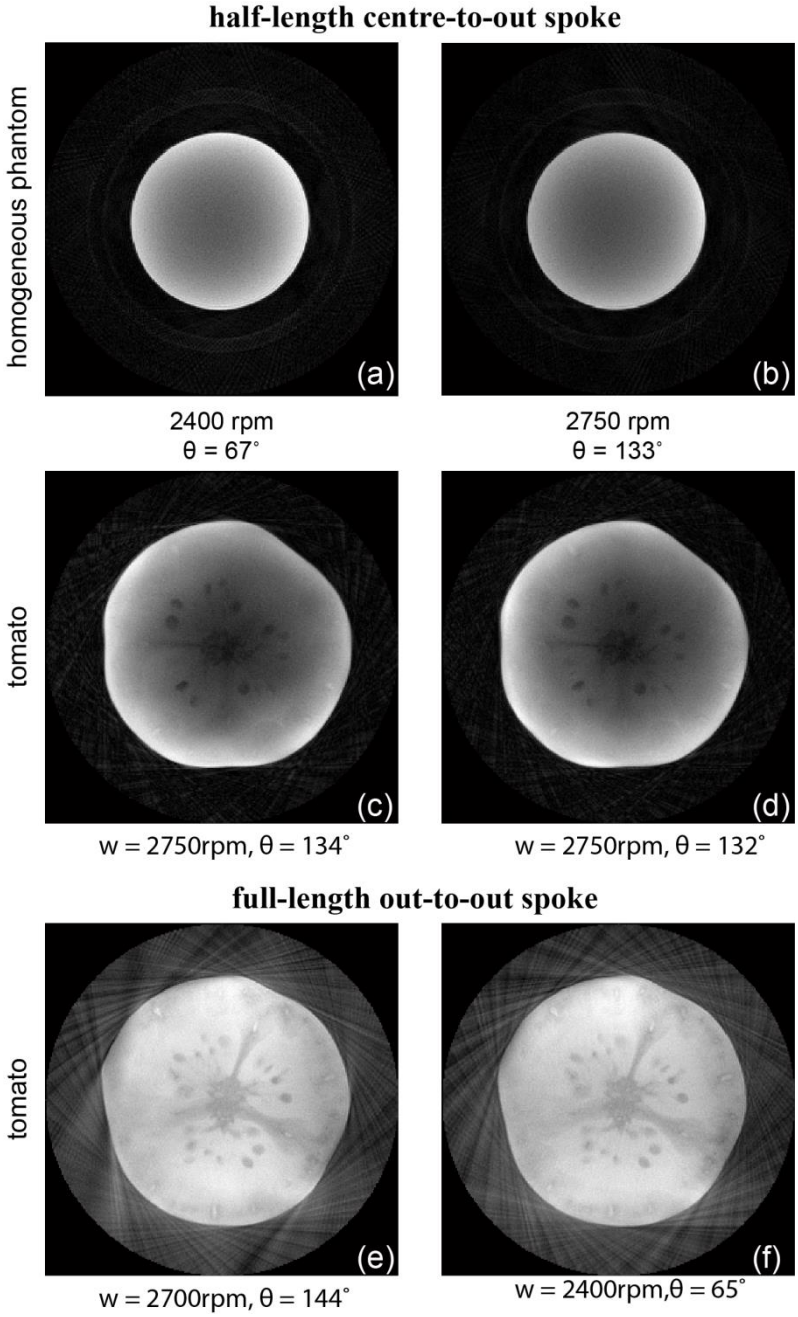

Figure 6-11. (a) and (b) are phantom images reconstructed from "half-length" radially sampled data. (c) and (d) are tomato images reconstructed from "half-length" radially sampled data. (e) and (f) are tomato images reconstructed from "full-length" radially sampled data.

To test the reproducibility of the reconstruction quality, a homogeneous phantom and a tomato were also used for imaging at the speeds that produced good images for the LEGO phantom. As shown in Figure 6-11(a) ~ (d), the reconstructed images were free of artefacts at those speeds. However, similar to the reconstructed LEGO images, both the homogeneous images and the tomato images exhibited reduced signal intensity in the centre. Such a signal loss was attributed to the implementation of the "half-length" trajectory with the UTE sequence. The UTE sequence is specially designed to sample data at the gradient "ramp-up" phase. Therefore, the data sampled at

the beginning are easily contaminated by the gradient distortions [204-206]. It was found that *k*-space data in a small region including and surrounding the *k*-space centre was not sampled. Consequently, the energy at the central of the *k*-space was slightly reduced. Using "full-length" radial trajectory can effectively avoid such distortion as shown in Figure 6-11 (e) and (f).

6.4. Discussions

6.4.1. Coil structure

The coil sensitivity is primarily determined by the coil structure given a certain subject. In the rotating scheme, a small coil naturally has a narrow sensitivity beam that needs more repeated oversamplings to generate a uniform equivalent sensitivity. The RRFC prototype has only one coil element with a 60˚ open angle, which needs approximately needs three oversamplings with a 120˚ angular increment to generate uniform sensitivity and facilitate on-line regridding reconstruction. To achieve a range of optimal angular increments, the rotation speeds are constrained to a certain region. Increasing the coil size and therefore coverage, or having a number of simultaneous RF elements will alleviate such constraint and allow more flexible choices of rotation speeds.

6.4.2. Reconstruction

In this chapter, by matching the rotation speed and sequence parameters, images were rapidly reconstructed with system built-in regridding algorithm. However, the drawback of this rapid imaging scheme is the incomplete *k*-space sampling. The radial trajectory only sample data in a circular region that excludes the four corners of the square *k*-space; therefore, some high-frequency information are missing. This will not cause apparent artefacts for a subject rich in details, like a brain demonstrated in Figure 6-6(j); however, artefacts can exhibit while imaging a subject with a large portion of high-frequency information, such as angiography or Shepp-Logan phantom in Figure 6-6 (m) and (n). It is hoped that the pseudo-radial trajectory which covers whole *k*-space or other rapid radial-wise reconstruction could be employed to improve image reconstruction quality in the future.

6.5. Conclusions

In this chapter, a single-element transceive rotating coil was constructed and tested on a 9.4T preclinical MRI scanner. The feasibility of using the radial trajectory for rapid and practical imaging scheme without sensitivity mapping was investigated. The averaging effect was firstly mathematically characterised, and then used for artefact suppression. With both simulations and experiments, it is proved that with a good match-up of TR and rotation speed, the uniform resultant sensitivity allows a rapid, artefact-free reconstruction on the host computer. Additionally, it is

demonstrated that the rotating coil can provide a uniform excitation without intensity bias, allowing rotation to be successfully used in transceive mode. This extends the possible application of the method to multi-nuclear (X-nuclei) imaging. Planned future work includes the optimisation of the RF elements and exploring the undersampling potential of radial acquisition for real-time imaging.

Chapter 7. Conclusion

7.1. Contributions and implications

Using mathematical derivation and evidence from clinical images, the benefits of ultra-high field MRI were demonstrated in Chapter 2. However, the inhomogeneous B_1 field, the elevated heating hazard and the long scan duration are practical issues that need to be addressed before the benefits that ultra-high fields offer can be realised. In order to overcome these issues and realise the potential of ultra-high field MRI, many studies have been carried out to develop various methods. As reviewed in Chapter 3, each method has advantages and limitations, but until now, there has been no universally accepted solution to these ultra-high field issues.

As the most effective methods to solve transmit and receive related issues, parallel transmission and parallel imaging require the use of phased array coils (PACs) and theoretically, a large number of coils improve the efficiency of those methods. However, placing more coils in a confined surface requires the use of smaller coils that are closer to each other. This may undermine coil efficiency by stronger coupling and shallower B_1 penetration. As an alternative method, the single element rotating RF coil (RRFC) was developed for image reconstruction and scan duration reduction. The single rotating coil element is naturally big and decoupled, leading to much better efficiency and deeper B_1 penetration than PACs. Additionally, the rotating coil is capable of acquiring a large number of transmit and receive sensitivities during rotation; therefore, it could also be employed for B_1 shimming and SAR control. However, with only one coil, the RRFC must increase the rotation velocity to accelerate acquisition, which is a limiting factor in practice, especially used as large volume coil. Since the rotating technique allows more sensitivity profiles to be acquired without increasing the number of coils, fewer coils are needed for a coil array. Therefore, coil efficiency issues are avoided and the performance of parallel transmission/imaging could be improved. At the same time, with multiple rotating elements, the rotating technique could employ algorithms based on parallel imaging to accelerate acquisition without increasing rotation velocity.

In this thesis, for the first time, the coil array concept was combined with the rotating technique to synergize strengths from each method and to address their shortcomings. The development process for this rotating technique and corresponding algorithms for fast imaging and B_1 inhomogeneity mitigation was presented in Chapter 4 and Chapter 5. In order to extend the rotating technique to a broader range of applications that requires prompt image output, in Chapter 6, a new imaging scheme employing radial trajectory and a fast on-line reconstruction algorithm was developed.

In this thesis, the rotating techniques were developed with the aim of designing better solutions for ultra-high field issues. The contributions of this research, its implications and limitations will be examined in the following sections. Future research directions are also discussed in terms of improving performance and extending the applications of rotating technique.

7.1.1. Contributions

7.1.1.1. Highly accelerated acquisition and B_1 inhomogeneity mitigation with a Rotating RF coil array (RRFCA) at 7 T (Chapter 4)

A novel 4-element rotating RF coil array (RRFCA) was manufactured and employed for scan time reduction and image reconstruction with mitigated inhomogeneous intensity. Incorporating advantages of the rotating technique and array structure, coils in the RRFCA were bigger and well decoupled, which provided better efficiency and deeper B_1 penetration to facilitate B_1 inhomogeneity mitigation and imaging acceleration. More importantly, each coil was capable of acquiring a large number of transmit and receive sensitivity profiles thus facilitating scan time reduction and B_1 inhomogeneity mitigation. By employing numerical models, the geometry of the RRFCA was optimised to minimise coupling and to maximise B_1 field penetration. Dedicated algorithms for image reconstruction and acquisition acceleration were developed and validated using a homogenous phantom.

The results indicated that, with the assistance of rotation and larger coils, the RRFCA was able to reconstruct images without inhomogeneous artefacts at high reduction factors using the proposed methods. In addition, our proposed algorithms were also capable of reconstructing images faithfully with higher global and more uniform signal-to-noise ratio (SNR) distribution at high reduction factors of scan duration. The rotating coil array has the potential to facilitate rapid, high quality human imaging for ultra-high field MRI.

7.1.1.2. Realising fast in vivo imaging with the rotating coil array via use of a novel sensitivity estimation method (Chapter 5)

After validating the imaging ability of the RRFCA with a homogeneous phantom, the feasibility of using the RRFCA for *in vivo* imaging was investigated. The *in vivo* sensitivity profiles (B_1^-) become distinct at various angular positions at 7 T. Therefore, sensitivity maps at angular positions cannot be obtained with the simple numerical methods used in phantom imaging.

A novel rotation-dependent *in vivo* sensitivity estimation algorithm was developed to facilitate *in vivo* fast imaging with the RRFCA at 7 T. Based on the observation that sensitivity is more related to the global dielectric properties rather than local changes, this method employed registration techniques to find the relationship between sensitivity in a library and acquired profiles.

This relationship was then transferred to an arbitrary angular position to estimate corresponding sensitivity profiles. In order to improve the accuracy, the individual coil sensitivities were optimally combined before feeding into the registration process. The results indicate that the proposed method is capable of accurately estimating both the magnitude and the phase of the sensitivity maps at an arbitrary angular position, which enables us to employ the rotating-SENSE method to perform imaging acceleration and reconstruction. Compared to a stationary coil array with the same number of coils, the RRFCA was able to reconstruct images with better quality at a higher reduction factor. It is hoped that the proposed sensitivity estimation algorithm and the acceleration ability of the RRFCA will be particularly useful for human imaging in ultra-high field MRI.

7.1.1.3. A rapid and practical imaging scheme using rotating technique with radial sampling at 9.4 T (Chapter 6)

The dedicated rotating-SENSE and the *in vivo* rotation-dependent sensitivity estimation is capable of reconstructing images faithfully at high reduction factors; nevertheless, these methods require dedicated sensitivity calibration algorithms; therefore, images cannot be reconstructed on-line with built-in system algorithms. This may limit using the rotating technique for applications that require immediate image output.

In order to improve the practicality of the rotating technique for *in vivo* applications, a rapid and practical imaging scheme was developed for the rotating coil by employing radial trajectory and characterising rotation-related motion artefacts. The numerical and experimental results (see Chapter 6) indicate that, by exploiting the averaging effect of the radial sampling and the optimisation of rotation velocity, images can be faithfully and rapidly reconstructed by built-in system algorithms without measuring B_1^+ and B_1^- maps. The successful experimental validation on a 9.4 T pre-clinical system represents an important step toward applying the rotating technique for *in vivo* imaging.

7.1.2. Implications

In this thesis, a 4-element rotating coil array was built to accelerate acquisition and reconstruct images without B_1 inhomogeneity. This rotating array was used to acquire proton images from a homogeneous phantom and two human subjects. As demonstrated in Chapter 4 and 5, the 4-element RRFCA was able to reconstruct better images with higher and more uniform SNR compared to an 8-element stationary coil array. This will improve the diagnostic accuracy by reducing dark and bright interference. In addition, the RRFCA is capable of reconstructing images in only a quarter of the time compared to a full *k*-space sampling. This dramatically increases the possibility of acquiring high quality images without contamination from motion artefacts. It is also hoped these

methods will benefit neuroimaging such as the *f*MRI, which is considered one of the major reasons for developing ultra-high field MRI. The fast partial acquisition in conjunction with fast gradient sequences could offer higher temporal resolution that has better opportunity to capture brain reactions under one second.

7.2. Limitations

7.2.1. SNR

With four elements, the coils of the RRFCA are large and decoupled, which benefits the image reconstruction and B_1 mitigation. As shown in Figure 5-9, the 4-element RRFCA is able to reconstruct an image to a similar quality as compared to an 8-element stationary coil array. However, since the SNR is proportional to the square root of the number of simultaneous channels [171], the SNR of a 4-channel RRFCA is naturally lower than that of an 8-element coil array. It is hoped the SNR of the rotating array can be improved by optimising the number of coils and the geometry. Besides the number of channels, the SNR is also proportional to the square root of the number of acquisitions. In Chapter 6, it was noted that when the single element rotating coil sampled data in a radial trajectory, the central *k*-space was oversampled. The consequent averaging effect of the central *k*-space region can improve SNR. It is expected that the SNR can be further improved with the optimisation of the radial sequence.

7.2.2. Actuation mode and signal transportation

Currently, two rotating strategies have been designed, namely stepping mode and continuous mode. The RRFCA rotates in the stepping mode, which samples a *k*-space line at each stepping angular position. Currently, the stepping rotation is realised manually to develop acquisition acceleration and B_1 mitigation algorithms. The automatic pneumatic rotation system has been successful constructed and adopted by the RRFC. The continuous rotation prevents the use of conventional RF connections with wires; therefore, a frictionless inductively coupled RF link was used to connect the rotating coil. Although the inductive coupling was well adjusted, signal loss was inevitable. In addition, it may be hard to accommodate more than two coils by this signal transportation method. The compressed air pressure varied during the experiment, and even with a modulator, the rotation speed still varied by about 5%. This could cause inaccurate positioning and undermine the reconstruction quality of the newly developed imaging scheme, which requires a stable rotation velocity to match up the radial sampling. In the future, the automatic rotating system in stepping mode is expected to be manufactured to overcome the shortcomings of the continuous mode.

7.2.3. Image reconstructions

By using radial sampling, the method developed in Chapter 6 can faithfully reconstruct images using system built-in algorithms. However, since radial trajectory only samples data in the circular region of the *k*-space, four corners of the square *k*-space that contain high-frequency information are not sampled. This is not an issue for a subject rich in details, since detailed low-frequency information is mostly located in the central *k*-space region; however, this could cause artefacts for a subject rich in high-frequency information, such as angiography images or a Shepp-Logan phantom. It is hoped that pseudo-radial trajectory that covers the whole *k*-space will be used for improving image quality.

7.3. Future work

Future work will mainly focus on the improvement of existing solutions and extending the applications of the rotating technique. Specifically, the imaging scheme developed in Chapter 6 could achieve better performance with optimised coil geometry and improved reconstruction algorithms. The rotating technique could be used for simultaneous X-nuclei imaging (proton imaging with simultaneous sodium/phosphorus imaging), since multiple coils with different frequencies could be arranged and rotate together without coupling. In addition, algorithms similar to rotating-SENSE could be developed for coils travelling in other motions to accelerate acquisition and mitigate B_1.

7.3.1. Improvement of current solutions

7.3.1.1. Coil geometry optimisation

Coil sensitivity is closely related to coil structure; therefore, the optimised coil geometry assures better image quality. In Chapter 6, the reconstruction quality of the radially sampled data by the RRFC is highly dependent on the oversampled data and the uniformity of their superposed sensitivity profiles. A coil with a larger open angle has greater likelihood to form a more uniform superposed sensitivity, thereby improving the reconstruction quality. However, since the area of the coil former is confined, the number and the size of coils need to be optimised in the future.

7.3.1.2. Improving reconstruction and acceleration algorithms

Currently, with radial sampling, given the optimised rotation speed, the image can be readily and faithfully reconstructed with a built-in system regridding algorithm. However, the image quality could be further improved and the rotation speed could be more flexible by potentially incorporating the previously developed methods, such as sensitivity removing [207] and iterative solutions [129, 192]. By removing sensitivity weightings from *k*-space data before the inverse Fourier transform, it is not necessary to consider the non-uniformity of sensitivity superposition of

oversampled *k*-space data, thus data acquired at any speed can be reconstructed using a direct inverse fast Fourier transform. Alternatively, the iterative solution could be employed to resolve a full *k*-space instead of a circular radial sampling region. However, all of those methods require accurate sensitivity mappings, which could be offered by a more robust and controllable rotating system. In the future, such an automatic rotating system will be built by means of nonmagnetic driving schemes, such as using electro-piezo motors.

It is well known that the radial sampling has great potential in dynamic imaging and fast imaging. Our next step is to investigate its undersampling potential with compressed sensing, which is a recently developed iterative algorithm that allows the use of much less data for faithful reconstruction. Since regridding and inverse regridding algorithms are time-consuming in iterative solutions, pseudo-polar sampling and reconstruction [208] or other radial-wise reconstruction algorithms will also be explored.

7.3.2. Extending rotating techniques for wider applications

7.3.2.1. Simultaneous X-nuclei imaging

In Chapter 6, the rapid imaging scheme using radial sampling with the rotating coil was validated with proton images. In fact, this method is particularly suitable for sodium/phosphorus imaging, since its reconstruction does not rely on sensitivity information, which may be hard to acquire for sodium/phosphorus imaging, due to the much lower concentration of sodium and phosphorus in the human body. This novel coil structure offers other key advantages for simultaneous X-nuclear imaging, such as low coupling and large coil size that provide deeper B_1 penetration and higher SNR. Based on the proposed rotating technique, a simultaneous X-nuclei imaging scheme is being developed with our industry partner, Bruker BioSpin (Germany).

7.3.2.2. Coils traveling in other motions

The rotating-SENSE technique used in Chapter 4 and Chapter 5 is based on SENSE algorithms, which could be employed by coils travelling in other motions, such as horizontal translation that parallels B_0. A "shifting coil array" with a low number of channels could be used for imaging the whole spine with reduced scan duration by using a corresponding "shifting-SENSE" algorithm. Similar to the *in vivo* sensitivity estimation algorithm developed in Chapter 5, the sensitivity for a spine scan could also be estimated by using library data and registration techniques.

7.3.2.3. SAR management

The preliminary results of SAR control with the rotating technique were reported in [182]. The simulation results demonstrated the SAR management of the single element rotating coil was better than that of an 8-element stationary coil array. In the future, this capability will be further explored

with a multi-element rotating coil array. Much better SAR management by such a rotating coil array is expected, since the ability to modulate transmit magnetic fields and electric fields is much improved with multiple coils. In order to accurately control subject-dependent local-SAR, a practical method to estimate SAR distribution is desperately needed.

References

[1] V. I. Madai, F. C. von Samson-Himmelstjerna, M. Bauer, K. L. Stengl, M. A. Mutke, E. Tovar-Martinez, *et al.*, "Ultrahigh-Field MRI in Human Ischemic Stroke – a 7 Tesla Study," *PLoS ONE,* vol. 7, p. e37631, 2012.

[2] G. H. Welsch, V. Juras, P. Szomolanyi, T. C. Mamisch, P. Baer, C. Kronnerwetter, *et al.*, "Magnetic resonance imaging of the knee at 3 and 7 Tesla: a comparison using dedicated multi-channel coils and optimised 2D and 3D protocols," *European radiology,* vol. 22, pp. 1852-1859, 2012.

[3] W. van der Zwaag, S. Francis, K. Head, A. Peters, P. Gowland, P. Morris, *et al.*, "fMRI at 1.5, 3 and 7 T: Characterising BOLD signal changes," *NeuroImage,* vol. 47, pp. 1425-1434, 10/1/ 2009.

[4] R. Brown, P. Storey, C. Geppert, K. McGorty, A. Leite, J. Babb, *et al.*, "Breast MRI at 7 Tesla with a bilateral coil and T1-weighted acquisition with robust fat suppression: image evaluation and comparison with 3 Tesla," *European Radiology,* vol. 23, pp. 2969-2978, 2013/11/01 2013.

[5] V. Juras, Š. Zbýň, C. Pressl, S. E. Domayer, J. G. Hofstaetter, M. E. Mayerhoefer, *et al.*, "Sodium MR imaging of Achilles tendinopathy at 7 T: preliminary results," *Radiology,* vol. 262, pp. 199-205, 2012.

[6] R. Beisteiner, S. Robinson, M. Wurnig, M. Hilbert, K. Merksa, J. Rath, *et al.*, "Clinical fMRI: evidence for a 7T benefit over 3T," *Neuroimage,* vol. 57, pp. 1015-21, Aug 1 2011.

[7] S. Trattnig, Š. Zbýň, B. Schmitt, K. Friedrich, V. Juras, P. Szomolanyi, *et al.*, "Advanced MR methods at ultra-high field (7 Tesla) for clinical musculoskeletal applications," *European Radiology,* vol. 22, pp. 2338-2346, 2012/11/01 2012.

[8] L. B. Pierre-Marie Robitalle, *Ultra High Field Magnetic Resonance Imaging*. New York, USA: Springer Science + Business Media, 2006.

[9] J. M. Theysohn, S. Maderwald, O. Kraff, C. Moenninghoff, M. E. Ladd, and S. C. Ladd, "Subjective acceptance of 7 Tesla MRI for human imaging," *Magma,* vol. 21, pp. 63-72, Mar 2008.

[10] M. A. Griswold, P. M. Jakob, R. M. Heidemann, M. Nittka, V. Jellus, J. Wang, *et al.*, "Generalized autocalibrating partially parallel acquisitions (GRAPPA)," *Magnetic Resonance in Medicine,* vol. 47, pp. 1202-1210, 2002.

[11] K. P. Pruessmann, M. Weiger, M. B. Scheidegger, and P. Boesiger, "SENSE: Sensitivity encoding for fast MRI," *Magnetic Resonance in Medicine,* vol. 42, pp. 952-962, 1999.

[12] K. P. Pruessmann, M. Weiger, P. Bornert, and P. Boesiger, "Advances in sensitivity encoding with arbitrary k-space trajectories," *Magnetic Resonance in Medicine,* vol. 46, pp. 638-51, 2001.

[13] D. K. Sodickson and W. J. Manning, "Simultaneous acquisition of spatial harmonics (SMASH): Fast imaging with radiofrequency coil arrays," *Magnetic Resonance in Medicine,* vol. 38, pp. 591-603, 1997.

[14] X. Zhang, S. Zhu, and B. He, "Imaging Electric Properties of Biological Tissues by RF Field Mapping in MRI," *IEEE transactions on medical imaging,* vol. 29, pp. 474-481, 2010.

[15] J. Jin, F. Liu, E. Weber, and S. Crozier, "Improving SAR estimations in MRI using subject-specific models," *Physics in Medicine and Biology,* vol. 57, pp. 8153-71, Dec 21 2012.

[16] CM Collins , Z Wang, and M. Smith, "A conservative method for ensuring safety within transmit arrays," in *In: Proceedings of the 15th Annual Meeting of ISMRM,* Berlin, Germany, 2007.

[17] K. Setsompop, V. Alagappan, B. Gagoski, T. Witzel, J. Polimeni, A. Potthast, *et al.*, "Slice-selective RF pulses for in vivo B 1+ inhomogeneity mitigation at 7 tesla using parallel RF excitation with a 16-element coil," *Magnetic Resonance in Medicine,* vol. 60, pp. 1422-1432, 2008.

[18] S. Oh, A. G. Webb, T. Neuberger, B. Park, and C. M. Collins, "Experimental and Numerical Assessment of MRI-Induced Temperature Change and SAR Distributions in Phantoms and In Vivo," *Magnetic resonance in medicine : official journal of the Society of Magnetic Resonance in Medicine / Society of Magnetic Resonance in Medicine,* vol. 63, pp. 218-223, 2010.

[19] D. Qian, A.-M. M. El-Sharkawy, P. A. Bottomley, and W. A. Edelstein, "An RF dosimeter for independent SAR measurement in MRI scanners," *Medical Physics,* vol. 40, p. 122303, 11/15 2013.

[20] J. P. Stralka and P. A. Bottomley, "A prototype RF dosimeter for independent measurement of the average specific absorption rate (SAR) during MRI," *Journal of Magnetic Resonance Imaging,* vol. 26, pp. 1296-1302, 2007.

[21] T. S. Ibrahim, R. Lee, B. A. Baertlein, A. M. Abduljalil, H. Zhu, and P. M. L. Robitaille, "Effect of RF coil excitation on field inhomogeneity at ultra high fields: A field optimized TEM resonator," *Magnetic Resonance Imaging,* vol. 19, pp. 1339-1347, Dec 2001.

[22] P. de Heer, W. M. Brink, B. J. Kooij, and A. G. Webb, "Increasing signal homogeneity and image quality in abdominal imaging at 3 T with very high permittivity materials," *Magnetic Resonance in Medicine,* vol. 68, pp. 1317-1324, 2012.

[23] U. Katscher, P. Bornert, C. Leussler, and J. S. van den Brink, "Transmit SENSE," *Magnetic Resonance in Medicine,* vol. 49, pp. 144-50, 2003.

[24] Y. Zhu, "Parallel excitation with an array of transmit coils," *Magnetic Resonance in Medicine,* vol. 51, pp. 775-784, 2004.

[25] X. Zhang, P.-F. V. de Moortele, S. Schmitter, and B. He, "Complex B1 mapping and electrical properties imaging of the human brain using a 16-channel transceiver coil at 7T," *Magnetic Resonance in Medicine,* vol. 69, pp. 1285-1296, 2013.

[26] W. M. Brink and A. G. Webb, "High permittivity pads reduce specific absorption rate, improve B1 homogeneity, and increase contrast-to-noise ratio for functional cardiac MRI at 3 T," *Magnetic Resonance in Medicine,* vol. 71, pp. 1632-1640, 2014.

[27] U. Katscher, T. Voigt, C. Findeklee, P. Vernickel, K. Nehrke, and O. Dossel, "Determination of electric conductivity and local SAR via B1 mapping," *IEEE Trans Med Imaging,* vol. 28, pp. 1365-74, Sep 2009.

[28] A. L. H. M. W. van Lier, D. O. Brunner, K. P. Pruessmann, D. W. J. Klomp, P. R. Luijten, J. J. W. Lagendijk, *et al.*, "B 1+ Phase mapping at 7 T and its application for in vivo electrical conductivity mapping," *Magnetic Resonance in Medicine,* vol. 67, pp. 552-561, 2012.

[29] A. M. El-Sharkawy, D. Qian, P. A. Bottomley, and W. A. Edelstein, "A multichannel, real-time MRI RF power monitor for independent SAR determination," *Medical Physics,* vol. 39, pp. 2334-41, 2012.

[30] T. Voigt, U. Katscher, and O. Doessel, "Quantitative conductivity and permittivity imaging of the human brain using electric properties tomography," *Magnetic Resonance in Medicine,* vol. 66, pp. 456-466, 2011.

[31] R. Abraham and T. S. Ibrahim, "Proposed radiofrequency phased-array excitation scheme for homogenous and localized 7-Tesla whole-body imaging based on full-wave numerical simulations," *Magnetic Resonance in Medicine,* vol. 57, pp. 235-42, 2007.

[32] J. T. Vaughan, G. Adriany, C. J. Snyder, J. Tian, T. Thiel, L. Bolinger, *et al.*, "Efficient high-frequency body coil for high-field MRI," *Magnetic Resonance in Medicine,* vol. 52, pp. 851-859, 2004.

[33] T. Vaughan, L. DelaBarre, C. Snyder, J. Tian, C. Akgun, D. Shrivastava, *et al.*, "9.4T human MRI: Preliminary results," *Magnetic Resonance in Medicine,* vol. 56, pp. 1274-1282, 2006.

[34] M. de Greef, O. Ipek, A. J. E. Raaijmakers, J. Crezee, and C. A. T. van den Berg, "Specific absorption rate intersubject variability in 7T parallel transmit MRI of the head," *Magnetic Resonance in Medicine,* vol. 69, pp. 1476-1485, 2013.

[35] W. M. Teeuwisse, W. M. Brink, K. N. Haines, and A. G. Webb, "Simulations of high permittivity materials for 7 T neuroimaging and evaluation of a new barium titanate-based dielectric," *Magnetic Resonance in Medicine,* vol. 67, pp. 912-8, 2012.
[36] W. Mao, M. B. Smith, and C. M. Collins, "Exploring the limits of RF shimming for high-field MRI of the human head," *Magnetic Resonance in Medicine,* vol. 56, pp. 918-922, 2006.
[37] W. M. Brink and A. G. Webb, "High permittivity pads reduce specific absorption rate, improve B1 homogeneity, and increase contrast-to-noise ratio for functional cardiac MRI at 3 T," *Magnetic Resonance in Medicine,* vol. 71, pp. 1632-40, Apr 2014.
[38] G. C. Wiggins, C. Triantafyllou, A. Potthast, A. Reykowski, M. Nittka, and L. L. Wald, "32-channel 3 Tesla receive-only phased-array head coil with soccer-ball element geometry," *Magnetic Resonance in Medicine,* vol. 56, pp. 216-223, 2006.
[39] G. C. Wiggins, J. R. Polimeni, A. Potthast, M. Schmitt, V. Alagappan, and L. L. Wald, "96-Channel receive-only head coil for 3 Tesla: Design optimization and evaluation," *Magnetic Resonance in Medicine,* vol. 62, pp. 754-762, 2009.
[40] A. Trakic, H. Wang, E. Weber, B. K. Li, M. Poole, F. Liu, *et al.*, "Image reconstructions with the rotating RF coil," *Journal of Magnetic Resonance,* vol. 201, pp. 186-198, 2009.
[41] A. Trakic, B. K. Li, E. Weber, H. Wang, S. Wilson, and S. Crozier, "A rapidly rotating RF coil for MRI," *Concepts in Magnetic Resonance Part B: Magnetic Resonance Engineering,* vol. 35B, pp. 59-66, 2009.
[42] P. Rinck. (2014). *Magnetic Resonance in Medicine. The Basic Textbook of the European Magnetic Resonance Forum. (8th edition ed.).*
[43] D. J. Griffiths, *Introduction to Quantum Mechanics*: Pearson, 2013.
[44] E. Merzbacher, *Quantum Mechanics*: Wiley, 1998.
[45] E. A. M. Donald W. McRobbie, Martin J. Graves, Martin R. Prince, *MRI from Picture to Proton*: Cambridge University Press, 28 Sep 2006.
[46] A. Abragam, *The principles of nuclear magnetism*: Clarendon Press, 1983.
[47] R. W. Brown;, Y.-C. N. Cheng;, E. M. Haacke;, M. R. Thompson;, and R. Venkatesan, *Magnetic Resonance Imaging: Physical Properties and Sequence Design*: Wiley-Liss 1999.
[48] E. Mark, M. R. T. Haacke, and R. W. Brown, "Magnetic resonance imaging: physical principles and sequence design," *New York: Wisely-Liss,* 1999.
[49] J. A. S. Jerrold T. Bushberg, Edwin M. Leidholdt, John M. Boone, *The Essential Physics of Medical Imaging*: LWW; Third, North American Edition edition, 28 Dec 2011.
[50] T. Geva, "Magnetic resonance imaging: historical perspective," *Journal of Cardiovascular Magnetic Resonance,* vol. 8, pp. 573-80, 2006.
[51] F. Bloch, "Nuclear Induction," *Physical Review,* vol. 70, pp. 460-474, 10/01/ 1946.
[52] E. M. Purcell, H. C. Torrey, and R. V. Pound, "Resonance Absorption by Nuclear Magnetic Moments in a Solid," *Physical Review,* vol. 69, pp. 37-38, 01/01/ 1946.
[53] D. I. Hoult, "The principle of reciprocity in signal strength calculations - A mathematical guide," *Concepts in Magnetic Resonance,* vol. 12, pp. 173-187, 2000.
[54] D. K. Cheng, *Field and Wave Electromagnetics*, 2nd ed. Massachusetts: Addison–Wesley Pub. Co, 1989.
[55] D. I. Hoult and R. E. Richards, "The signal-to-noise ratio of the nuclear magnetic resonance experiment," *Journal of Magnetic Resonance (1969),* vol. 24, pp. 71-85, 10// 1976.
[56] H. Nyquist, "Thermal Agitation of Electric Charge in Conductors," *Physical Review,* vol. 32, pp. 110-113, 07/01/ 1928.
[57] W. A. Edelstein, G. H. Glover, C. J. Hardy, and R. W. Redington, "The intrinsic signal-to-noise ratio in NMR imaging," *Magnetic Resonance in Medicine,* vol. 3, pp. 604-18, Aug 1986.
[58] C. M. Collins and M. B. Smith, "Calculations of B(1) distribution, SNR, and SAR for a surface coil adjacent to an anatomically-accurate human body model," *Magn Reson Med,* vol. 45, pp. 692-9, Apr 2001.

[59] S. A. Huettel, A. W. Song, and G. McCarthy, *Functional magnetic resonance imaging* vol. 1: Sinauer Associates Sunderland, MA, 2004.
[60] S. Ogawa, T. Lee, A. Kay, and D. Tank, "Brain magnetic resonance imaging with contrast dependent on blood oxygenation," *Proceedings of the National Academy of Sciences,* vol. 87, pp. 9868-9872, 1990.
[61] M. Barth and B. A. Poser, "Advances in High-Field BOLD fMRI," *Materials,* vol. 4, pp. 1941-1955, 2011.
[62] G. Krüger and G. H. Glover, "Physiological noise in oxygenation-sensitive magnetic resonance imaging," *Magnetic Resonance in Medicine,* vol. 46, pp. 631-637, 2001.
[63] S. Ogawa, R. S. Menon, D. W. Tank, S. G. Kim, H. Merkle, J. M. Ellermann, *et al.*, "Functional brain mapping by blood oxygenation level-dependent contrast magnetic resonance imaging. A comparison of signal characteristics with a biophysical model," *Biophysical Journal,* vol. 64, pp. 803-812, 1993.
[64] J. S. Gati, R. S. Menon, K. Ugurbil, and B. K. Rutt, "Experimental determination of the BOLD field strength dependence in vessels and tissue," *Magnetic Resonance in Medicine,* vol. 38, pp. 296-302, Aug 1997.
[65] E. Yacoub, T. Q. Duong, P. F. Van De Moortele, M. Lindquist, G. Adriany, S. G. Kim, *et al.*, "Spin-echo fMRI in humans using high spatial resolutions and high magnetic fields," *Magnetic Resonance in Medicine,* vol. 49, pp. 655-64, Apr 2003.
[66] J. Wang, L. He, H. Zheng, and Z.-L. Lu, "Optimizing the Magnetization-Prepared Rapid Gradient-Echo (MP-RAGE) Sequence," *PLoS ONE,* vol. 9, p. e96899, 2014.
[67] S. P. Brown R, McGorty K, "Toward improved T1-weighted breast imaging at 7T: preliminary results and comparison with 3T," in *ISMRM*, Melbourne, Australia, 2012.
[68] M. K. Brown R, Moy L, DeGregorio S, Sodickson DK, and W. GC, "Sub-millimeter breast imaging and relaxivity characterization at 7T," in *ISMRM*, Montreal, Canada, 2011.
[69] S. C. Fu, K. M. Chan, and C. G. Rolf, "Increased deposition of sulfated glycosaminoglycans in human patellar tendinopathy," *Clin J Sport Med,* vol. 17, pp. 129-34, Mar 2007.
[70] J. Shin, J. Lee, M.-O. Kim, N. Choi, J. K. Seo, and D.-H. Kim, "Quantitative Conductivity Estimation Error due to Statistical Noise in Complex B1+ Map," *Journal of the Korean Society of Magnetic Resonance in Medicine,* vol. 18, pp. 303-313, 2014.
[71] E. M. Merkle and B. M. Dale, "Abdominal MRI at 3.0 T: the basics revisited," *American Journal of Roentgenology,* vol. 186, pp. 1524-32, Jun 2006.
[72] M. A. Bernstein, J. Huston, 3rd, and H. A. Ward, "Imaging artifacts at 3.0T," *Journal of Magnetic Resonance Imaging,* vol. 24, pp. 735-46, Oct 2006.
[73] O. Dietrich;, M. F. Reiser;, and S. O. Schoenberg, "Artifacts in 3-Tesla MRI: Physical background and reduction strategies," *European Journal of Radiology,* vol. 65(1), pp. 29-35, 2008.
[74] M. Alecci, C. M. Collins, M. B. Smith, and P. Jezzard, "Radio frequency magnetic field mapping of a 3 Tesla birdcage coil: experimental and theoretical dependence on sample properties," *Magnetic Resonance in Medicine,* vol. 46, pp. 379-85, Aug 2001.
[75] C. Gabriel, "Compilation of the dielectric properties of body tissues at RF and microwave frequencies," Air Force Material Command Brooks Air Force Base, Texas, Occupational and Environmental Health Directorate , Radiofrequency Radiation Division, 2503 D Drive, Brooks Air Force Base, TX 78235-5102June 1996.
[76] J. Wang, Q. X. Yang, X. Zhang, C. M. Collins, M. B. Smith, X.-H. Zhu, *et al.*, "Polarization of the RF field in a human head at high field: A study with a quadrature surface coil at 7.0 T," *Magnetic Resonance in Medicine,* vol. 48, pp. 362-369, 2002.
[77] C. M. Collins, Q. X. Yang, J. H. Wang, X. Zhang, H. Liu, S. Michaeli, *et al.*, "Different excitation and reception distributions with a single-loop transmit-receive surface coil near a head-sized spherical phantom at 300 MHz," *Magnetic Resonance in Medicine,* vol. 47, pp. 1026-1028, 2002.

[78] C. M. Collins and M. B. Smith, "Signal-to-noise ratio and absorbed power as functions of main magnetic field strength, and definition of "90 degrees " RF pulse for the head in the birdcage coil," *Magnetic Resonance in Medicine,* vol. 45, pp. 684-91, Apr 2001.
[79] J. T. Vaughan, M. Garwood, C. M. Collins, W. Liu, L. DelaBarre, G. Adriany, *et al.*, "7T vs. 4T: RF power, homogeneity, and signal-to-noise comparison in head images," *Magnetic Resonance in Medicine,* vol. 46, pp. 24-30, Jul 2001.
[80] C. M. Collins and M. B. Smith, "Calculations of B1 distribution, SNR, and SAR for a surface coil adjacent to an anatomically-accurate human body model," *Magnetic Resonance in Medicine,* vol. 45, pp. 692-699, 2001.
[81] P. A. Bottomley, R. W. Redington, W. A. Edelstein, and J. F. Schenck, "Estimating radiofrequency power deposition in body NMR imaging," *Magnetic Resonance in Medicine,* vol. 2, pp. 336-49, Aug 1985.
[82] L. A. Zaremba, "FDA Guidelines for Magnetic Resonance Equipment Safety ", F. D. A. Center for Devices and Radiological Health, Ed., ed.
[83] "International standard, medical equipment – Part 2–33: Particular requirements for the safety of magnetic resonance equipment," vol. 60601, I. E. Commission, Ed., ed. Geneva, 2002.
[84] K. Yee, "Numerical solution of initial boundary value problems involving maxwell's equations in isotropic media," *Antennas and Propagation, IEEE Transactions on,* vol. 14, pp. 302-307, 1966.
[85] S. Wolf, D. Diehl, M. Gebhardt, J. Mallow, and O. Speck, "SAR simulations for high-field MRI: how much detail, effort, and accuracy is needed?," *Magnetic Resonance in Medicine,* vol. 69, pp. 1157-68, Apr 2013.
[86] A. Christ, W. Kainz, E. G. Hahn, K. Honegger, M. Zefferer, E. Neufeld, *et al.*, "The Virtual Family—development of surface-based anatomical models of two adults and two children for dosimetric simulations," *Physics in Medicine and Biology,* vol. 55, p. N23, 2010.
[87] R. Damadian, M. Goldsmith, and L. Minkoff, "NMR in cancer: XVI. FONAR image of the live human body," *Physiological Chemistry and Physics,* vol. 9, pp. 97-100, 108, 1977.
[88] *Adolescent Brain Development and the Effects of Drug Abuse: MRI Information*. Available: https://www.psych.umn.edu/faculty/luciana/mri_information.htm
[89] *MRI Artifacts*. Available: http://www.mr-tip.com/serv1.php?type=art&sub=Motion%20Artifact
[90] *Sequences and MRI Artifacts*. Available: http://www.mridoc.com/physics/sequences/
[91] S. Wang, J. Murphy-Boesch, H. Merkle, A. P. Koretsky, and J. H. Duyn, "B1 homogenization in MRI by multilayer coupled coils," *IEEE Trans Med Imaging,* vol. 28, pp. 551-4, Apr 2009.
[92] Q. X. Yang, W. Mao, J. Wang, M. B. Smith, H. Lei, X. Zhang, *et al.*, "Manipulation of image intensity distribution at 7.0 T: Passive RF shimming and focusing with dielectric materials," *Journal of Magnetic Resonance Imaging,* vol. 24, pp. 197-202, 2006.
[93] K. M. Franklin, B. M. Dale, and E. M. Merkle, "Improvement in B1-inhomogeneity artifacts in the abdomen at 3T MR imaging using a radiofrequency cushion," *Journal of Magnetic Resonance Imaging,* vol. 27, pp. 1443-1447, 2008.
[94] M. Sreenivas, M. Lowry, P. Gibbs, M. Pickles, and L. W. Turnbull, "A simple solution for reducing artefacts due to conductive and dielectric effects in clinical magnetic resonance imaging at 3T," *European Journal of Radiology,* vol. 62, pp. 143-146, 2007.
[95] Y. Takayama, H. Nonaka, M. Nakajima, T. Obata, and H. Ikehira, "Reduction of a high-field dielectric artifact with homemade gel," *Magnetic Resonance in Medical Sciences,* vol. 7, pp. 37-41, 2008.
[96] M. Kataoka, H. Isoda, Y. Maetani, Y. Nakamoto, T. Koyama, S. Umeoka, *et al.*, "MR imaging of the female pelvis at 3 Tesla: evaluation of image homogeneity using different dielectric pads," *Journal of Magnetic Resonance Imaging,* vol. 26, pp. 1572-7, Dec 2007.

[97] C. H. Cunningham, J. M. Pauly, and K. S. Nayak, "Saturated double-angle method for rapid B1+ mapping," *Magnetic Resonance in Medicine,* vol. 55, pp. 1326-33, Jun 2006.
[98] V. L. Yarnykh, "Actual flip-angle imaging in the pulsed steady state: a method for rapid three-dimensional mapping of the transmitted radiofrequency field," *Magnetic Resonance in Medicine,* vol. 57, pp. 192-200, Jan 2007.
[99] L. I. Sacolick, F. Wiesinger, I. Hancu, and M. W. Vogel, "B1 mapping by Bloch-Siegert shift," *Magnetic Resonance in Medicine,* vol. 63, pp. 1315-22, May 2010.
[100] C. M. Collins, Z. Wang, W. Mao, J. Fang, W. Liu, and M. B. Smith, "Array-optimized composite pulse for excellent whole-brain homogeneity in high-field MRI," *Magnetic Resonance in Medicine,* vol. 57, pp. 470-474, 2007.
[101] U. Katscher and P. Bornert, "Parallel RF transmission in MRI," *NMR in Biomedicine,* vol. 19, pp. 393-400, May 2006.
[102] U. Katscher, T. Voigt, C. Findeklee, P. Vernickel, K. Nehrke, and O. Dossel, "Determination of Electric Conductivity and Local SAR Via B1 Mapping," *Medical Imaging, IEEE Transactions on,* vol. 28, pp. 1365-1374, 2009.
[103] P. C. Lauterbur, "Image Formation by Induced Local Interactions: Examples Employing Nuclear Magnetic Resonance," *Nature,* vol. 242, pp. 190-191, 03/16/print 1973.
[104] P. Mansfield, "Multi-planar image formation using NMR spin echoes," *Journal of Physics C: Solid State Physics,* vol. 10, p. L55, 1977.
[105] J. Listerud, S. Einstein, E. Outwater, and H. Y. Kressel, "First principles of fast spin echo," *Magn Reson Q,* vol. 8, pp. 199-244, Dec 1992.
[106] P. van der Meulen, J. P. Groen, and J. J. Cuppen, "Very fast MR imaging by field echoes and small angle excitation," *Magnetic Resonance Imaging,* vol. 3, pp. 297-9, 1985.
[107] P. P. So, M. A. Stuchly, and J. A. Nyenhuis, "Peripheral nerve stimulation by gradient switching fields in magnetic resonance imaging," *IEEE Transactions on Biomedical Engineering* vol. 51, pp. 1907-14, Nov 2004.
[108] C. L. G. Ham, J. M. L. Engels, G. T. van de Wiel, and A. Machielsen, "Peripheral nerve stimulation during MRI: Effects of high gradient amplitudes and switching rates," *Journal of Magnetic Resonance Imaging,* vol. 7, pp. 933-937, 1997.
[109] D. J. Schaefer, J. D. Bourland, and J. A. Nyenhuis, "Review of patient safety in time-varying gradient fields," *Journal of Magnetic Resonance Imaging,* vol. 12, pp. 20-9, Jul 2000.
[110] F. Liu, L. Xia, and S. Crozier, "Influence of magnetically-induced E-fields on cardiac electric activity during MRI: A modeling study," *Magnetic Resonance in Medicine,* vol. 50, pp. 1180-8, Dec 2003.
[111] M. Lustig, D. Donoho, and J. M. Pauly, "Sparse MRI: The application of compressed sensing for rapid MR imaging," *Magnetic Resonance in Medicine,* vol. 58, pp. 1182-95, Dec 2007.
[112] M. Lustig, D. L. Donoho, J. M. Santos, and J. M. Pauly, "Compressed Sensing MRI," *Signal Processing Magazine, IEEE,* vol. 25, pp. 72-82, 2008.
[113] D. Liang, B. Liu, J. Wang, and L. Ying, "Accelerating SENSE using compressed sensing," *Magnetic Resonance in Medicine,* vol. 62, pp. 1574-84, Dec 2009.
[114] J. Miao, W. Guo, S. Narayan, and D. L. Wilson, "A simple application of compressed sensing to further accelerate partially parallel imaging," *Magnetic Resonance Imaging,* vol. 31, pp. 75-85, Jan 2013.
[115] F. Wiesinger, N. De Zanche, and K. Pruessman, "Approaching ultimate SNR with finite coil arrays," in *In: Proceedings of the 13th Annual Meeting of ISMRM,* Miami Beach,FL, USA, 2005.
[116] M. Schmitt, A. Potthast, D. E. Sosnovik, J. R. Polimeni, G. C. Wiggins, C. Triantafyllou, *et al.*, "A 128-channel receive-only cardiac coil for highly accelerated cardiac MRI at 3 Tesla," *Magnetic Resonance in Medicine,* vol. 59, pp. 1431-1439, 2008.

[117] C. J. Hardy, R. O. Giaquinto, J. E. Piel, K. W. Rohling, L. Marinelli, D. J. Blezek, *et al.*, "128-Channel Body MRI With a Flexible High-Density Receiver-Coil Array," *Journal of Magnetic Resonance Imaging,* vol. 28, pp. 1219-1225, Nov 2008.
[118] C. J. Hardy, R. D. Darrow, M. Saranathan, R. O. Giaquinto, Y. Zhu, C. L. Dumoulin, *et al.*, "Large field-of-view real-time MRI with a 32-channel system," *Magnetic Resonance in Medicine,* vol. 52, pp. 878-884, 2004.
[119] J. A. de Zwart, P. J. Ledden, P. Kellman, P. van Gelderen, and J. H. Duyn, "Design of a SENSE-optimized high-sensitivity MRI receive coil for brain imaging," *Magnetic Resonance in Medicine,* vol. 47, pp. 1218-27, Jun 2002.
[120] J. A. de Zwart, P. J. Ledden, P. van Gelderen, J. Bodurka, R. Chu, and J. H. Duyn, "Signal-to-noise ratio and parallel imaging performance of a 16-channel receive-only brain coil array at 3.0 Tesla," *Magnetic Resonance in Medicine,* vol. 51, pp. 22-6, Jan 2004.
[121] W. Liu, C. M. Collins, and M. B. Smith, "Calculations of Distribution, Specific Energy Absorption Rate, and Intrinsic Signal-to-Noise Ratio for a Body-Size Birdcage Coil Loaded with Different Human Subjects at 64 and 128 MHz," *Applied Magnetic Resonance,* vol. 29, pp. 5-18, Mar 2005.
[122] J. W. Hand, Y. Li, E. L. Thomas, M. A. Rutherford, and J. V. Hajnal, "Prediction of specific absorption rate in mother and fetus associated with MRI examinations during pregnancy," *Magnetic Resonance in Medicine,* vol. 55, pp. 883-93, Apr 2006.
[123] Z. Wang, J. C. Lin, W. Mao, W. Liu, M. B. Smith, and C. M. Collins, "SAR and temperature: simulations and comparison to regulatory limits for MRI," *Journal of Magnetic Resonance Imaging,* vol. 26, pp. 437-41, Aug 2007.
[124] C. A. Van den Berg, B. van den Bergen, J. B. Van de Kamer, B. W. Raaymakers, H. Kroeze, L. W. Bartels, *et al.*, "Simultaneous B1 + homogenization and specific absorption rate hotspot suppression using a magnetic resonance phased array transmit coil," *Magnetic Resonance in Medicine,* vol. 57, pp. 577-86, Mar 2007.
[125] M. A. Cloos, M. Luong, G. Ferrand, A. Amadon, D. Le Bihan, and N. Boulant, "Local SAR reduction in parallel excitation based on channel-dependent Tikhonov parameters," *Journal of Magnetic Resonance Imaging,* vol. 32, pp. 1209-16, Nov 2010.
[126] G. Eichfelder and M. Gebhardt, "Local specific absorption rate control for parallel transmission by virtual observation points," *Magnetic Resonance in Medicine,* vol. 66, pp. 1468-1476, 2011.
[127] H. Homann, I. Graesslin, K. Nehrke, C. Findeklee, O. Dossel, and P. Bornert, "Specific absorption rate reduction in parallel transmission by k-space adaptive radiofrequency pulse design," *Magnetic Resonance in Medicine,* vol. 65, pp. 350-7, Feb 2011.
[128] M. Blaimer, F. Breuer, M. Mueller, R. M. Heidemann, M. A. Griswold, and P. M. Jakob, "SMASH, SENSE, PILS, GRAPPA: how to choose the optimal method," *Topics in Magnetic Resonance Imaging,* vol. 15, pp. 223-36, Aug 2004.
[129] L. Feng, R. Grimm, K. T. Block, H. Chandarana, S. Kim, J. Xu, *et al.*, "Golden-angle radial sparse parallel MRI: Combination of compressed sensing, parallel imaging, and golden-angle radial sampling for fast and flexible dynamic volumetric MRI," *Magnetic Resonance in Medicine,* vol. 72, pp. 707-717, 2014.
[130] C. M. Collins, W. Liu, W. Schreiber, Q. X. Yang, and M. B. Smith, "Central brightening due to constructive interference with, without, and despite dielectric resonance," *Journal of Magnetic Resonance Imaging,* vol. 21, pp. 192-6, Feb 2005.
[131] Li M, Jin J, Trakic A, Liu F, Weber E, Li Y, *et al.*, "High Acceleration with Rotating Radiofrequency Coil Array (RRFCA) in Parallel Magnetic Resonance Imaging (MRI)," presented at the 34th Annual International Conference of the IEEE Engineering in Medicine and Biology Society (EMBC'12), San Diego, 2012.
[132] T. S. Miller, Tompkins County (N.Y.) Dept. of Planning, and U.S. Department of the Interior, "Unconsolidated aquifers in Tompkins County, New York," ed: U.S. Geological Survey, Branch of Information Services, 2000.

[133] P. Ullmann, S. Junge, M. Wick, F. Seifert, W. Ruhm, and J. Hennig, "Experimental analysis of parallel excitation using dedicated coil setups and simultaneous RF transmission on multiple channels," *Magn Reson Med*, vol. 54, pp. 994-1001, Oct 2005.
[134] Q. X. Yang, J. Wang, X. Zhang, C. M. Collins, M. B. Smith, H. Liu, *et al.*, "Analysis of wave behavior in lossy dielectric samples at high field," *Magnetic Resonance in Medicine*, vol. 47, pp. 982-989, 2002.
[135] D. I. Hoult and D. Phil, "Sensitivity and power deposition in a high-field imaging experiment," *Journal of Magnetic Resonance Imaging*, vol. 12, pp. 46-67, Jul 2000.
[136] J. Jin, F. Liu, Z. Zuo, R. Xue, M. Li, Y. Li, *et al.*, "Inverse field-based approach for simultaneous B(1) mapping at high fields - a phantom based study," *Journal of Magnetic Resonance*, vol. 217, pp. 27-35, Apr 2012.
[137] E. Weber;, A. Trakic;, M. L. ;, J. Jin;, F. Liu;, and S. Crozier, "Rotating Radiofrequency Coil (RRFC) Probe for 11.7T Small-animal MRI," presented at the 5th Asia-Pacfic NMR Symposium in conjuction with ANZMAG 2013, Brisabne, 2013.
[138] " Center for devices and radiologic health. Guidance for the submission of premarket notifications for magnetic resonance diagnostic devices," F. a. D. Administration, Ed., ed. Rockville, 1988.
[139] "International Electrotechnical Commission 2002 International standard, medical equipmen," ed. Geneva, 2002, pp. part2-33.
[140] Jin J, Liu F, Trakic A, Weber E, and Crozier S, "Application of Rotating RF Coil Array in B1 Shimming with Strict Local SAR Constraints,," presented at the 21th ISMRM, Salt Lake City,USA, 2013.
[141] S. Crozier, I. M. Brereton, F. O. Zelaya, W. U. Roffmann, and D. M. Doddrell, "Sample-Induced RF Perturbations in High-Field, High-Resolution NMR Spectroscopy," *Journal of Magnetic Resonance*, vol. 126, pp. 39-47, May 1997.
[142] P. S. Tofts, "Standing wave in uniform water phantoms," *Journal of Magnetic Resonance*, vol. 104(B), pp. 143-147, 1994.
[143] F. Liu and S. Crozier, "Electromagnetic fields inside a lossy, multilayered spherical head phantom excited by MRI coils: models and methods," *Physics in Medicine and Biology*, vol. 49, pp. 1835-51, May 21 2004.
[144] F. Liu, B. L. Beck, B. Xu, J. R. Fitzsimmons, S. J. Blackband, and S. Crozier, "Numerical modeling of 11.1T MRI of a human head using a MoM/FDTD method," *Concepts in Magnetic Resonance Part B: Magnetic Resonance Engineering*, vol. 24B, pp. 28-38, 2005.
[145] G. McLaughlin, T. Ji, and D. Napolitano, "Material probing method for medical application, involves receiving echoes generated by interactions between ultrasound beam and material, and converting received echoes to generate echolocation data," United States Patent US2004147841-A1;, 2004.
[146] T. S. Ibrahim, R. Lee, A. M. Abduljalil, B. A. Baertlein, and P. M. Robitaille, "Dielectric resonances and B(1) field inhomogeneity in UHFMRI: computational analysis and experimental findings," *Magnetic Resonance Imaging*, vol. 19, pp. 219-26, Feb 2001.
[147] A. Kangarlu, B. A. Baertlein, R. Lee, T. Ibrahim, L. Yang, A. M. Abduljalil, *et al.*, "Dielectric resonance phenomena in ultra high field MRI," *Journal of Computer Assisted Tomography*, vol. 23, pp. 821-31, Nov-Dec 1999.
[148] P. F. Van de Moortele, C. Akgun, G. Adriany, S. Moeller, J. Ritter, C. M. Collins, *et al.*, "B(1) destructive interferences and spatial phase patterns at 7 T with a head transceiver array coil," *Magnetic Resonance in Medicine*, vol. 54, pp. 1503-18, Dec 2005.
[149] D. L. Hill, P. G. Batchelor, M. Holden, and D. J. Hawkes, "Medical image registration," *Physics in Medicine and Biology*, vol. 46, pp. R1-45, Mar 2001.
[150] M. Holden, "A Review of Geometric Transformations for Nonrigid Body Registration," *Medical Imaging, IEEE Transactions on*, vol. 27, pp. 111-128, 2008.

[151] D. Rueckert, L. I. Sonoda, C. Hayes, D. L. Hill, M. O. Leach, and D. J. Hawkes, "Nonrigid registration using free-form deformations: application to breast MR images," *IEEE Transactions on Medical Imaging,* vol. 18, pp. 712-21, Aug 1999.
[152] S. J. Malik, D. J. Larkman, and J. V. Hajnal, "Optimal linear combinations of array elements for B1 mapping," *Magn Reson Med,* vol. 62, pp. 902-9, Oct 2009.
[153] L. Ying and J. Sheng, "Joint image reconstruction and sensitivity estimation in SENSE (JSENSE)," *Magnetic Resonance in Medicine,* vol. 57, pp. 1196-202, Jun 2007.
[154] C. A. McKenzie, E. N. Yeh, M. A. Ohliger, M. D. Price, and D. K. Sodickson, "Self-calibrating parallel imaging with automatic coil sensitivity extraction," *Magnetic Resonance in Medicine,* vol. 47, pp. 529-38, Mar 2002.
[155] F. Huang, Y. Chen, W. Yin, W. Lin, X. Ye, W. Guo, *et al.*, "A rapid and robust numerical algorithm for sensitivity encoding with sparsity constraints: self-feeding sparse SENSE," *Magnetic Resonance in Medicine,* vol. 64, pp. 1078-88, Oct 2010.
[156] J. Jin, F. Liu, E. Weber, Y. Li, and S. Crozier, "An electromagnetic reverse method of coil sensitivity mapping for parallel MRI – Theoretical framework," *Journal of Magnetic Resonance,* vol. 207, pp. 59-68, 2010.
[157] M. D. P. Dennis C. Ghiglia, *Two-Dimensional Phase Unwrapping: Theory, Algorithms, and Software*: John Wiley and Sons, Inc., 1998.
[158] J. Jin, F. Liu, E. Weber, Y. Li, and S. Crozier, "An electromagnetic reverse method of coil sensitivity mapping for parallel MRI - Theoretical framework," *Journal of Magnetic Resonance,* vol. 207, pp. 59-68, 2010.
[159] P. F. Van de Moortele, C. Akgun, G. Adriany, S. Moeller, J. Ritter, C. M. Collins, *et al.*, "B(1) destructive interferences and spatial phase patterns at 7 T with a head transceiver array coil," *Magn Reson Med,* vol. 54, pp. 1503-18, Dec 2005.
[160] J. B. Maintz and M. A. Viergever, "A survey of medical image registration," *Medical Image Analysis,* vol. 2, pp. 1-36, Mar 1998.
[161] R. Wan and M. Li, "An overview of medical image registration," in *Computational Intelligence and Multimedia Applications, 2003. ICCIMA 2003. Proceedings. Fifth International Conference on*, 2003, pp. 385-390.
[162] J. Jin, F. Liu, and S. Crozier, "Image registration guided, sparsity constrained reconstructions for dynamic MRI," *Magnetic Resonance Imaging*.
[163] F. Maes, A. Collignon, D. Vandermeulen, G. Marchal, and P. Suetens, "Multimodality image registration by maximization of mutual information," *Medical Imaging, IEEE Transactions on,* vol. 16, pp. 187-198, 1997.
[164] J. P. W. Pluim, J. B. A. Maintz, and M. A. Viergever, "Mutual-information-based registration of medical images: a survey," *Medical Imaging, IEEE Transactions on,* vol. 22, pp. 986-1004, 2003.
[165] T. M. B. J. Weese, C. Lorenz, and C. Fassnacht, "An approach to 2D/3D registration of a vertebra in 2D X-ray fluoroscopy," *CVRMed/MRCAS*, pp. 119-128, 1997.
[166] D. Rueckert, P. Aljabar, R. A. Heckemann, J. V. Hajnal, and A. Hammers, "Diffeomorphic registration using B-splines," *Med Image Comput Comput Assist Interv,* vol. 9, pp. 702-9, 2006.
[167] L. Seungyong, G. Wolberg, and S. Sung-Yong, "Scattered data interpolation with multilevel B-splines," *Visualization and Computer Graphics, IEEE Transactions on,* vol. 3, pp. 228-244, 1997.
[168] M. Li, Z. Zuo, J. Jin, R. Xue, A. Trakic, E. Weber, *et al.*, "Highly accelerated acquisition and homogeneous image reconstruction with rotating RF coil array at 7T-A phantom based study," *Journal of Magnetic Resonance,* vol. 240, pp. 102-12, Mar 2014.
[169] C. A. McKenzie, E. N. Yeh, and D. K. Sodickson, "Improved spatial harmonic selection for SMASH image reconstructions," *Magnetic Resonance in Medicine,* vol. 46, pp. 831-836, 2001.

[170] M. D. Harpen, "Sample noise with circular surface coils," *Med Phys*, vol. 14, pp. 616-8, Jul-Aug 1987.
[171] P. B. Roemer, W. A. Edelstein, C. E. Hayes, S. P. Souza, and O. M. Mueller, "The NMR phased array," *Magnetic Resonance in Medicine*, vol. 16, pp. 192-225, Nov 1990.
[172] R. F. Harrington, *Field Computation by Moment Methods*. New York: John Wiley and Sons, 1996.
[173] H. Ochi, E. Yamamoto, K. Sawaya, and S. Adachi, "Analysis of a Magnetic-Resonance-Imaging Antenna Inside an RF Shiled," *Electronics and Communications in Japan Part I-Communications*, vol. 77, pp. 37-45, Jan 1994.
[174] S. Wright and M. Lee, "Full-wave moment of method analysis of RF coils on lossy media.," in *In: Proceeding of the 6th Annual Meeting of 10th ISMRM,*, San Francisco, USA, 1991.
[175] M. Li, J. Jin, A. Trakic, F. Liu, E. Weber, Y. Li, *et al.*, "High Acceleration with Rotating Radiofrequency Coil Array (RRFCA) in Parallel Magnetic Resonance Imaging (MRI)," presented at the 34th Annual International Conference of the IEEE Engineering in Medicine and Biology Society (EMBC'12), San Diego, 2012.
[176] B. K. Li, F. Liu, E. Weber, and S. Crozier, "Hybrid numerical techniques for the modelling of radiofrequency coils in MRI," *NMR Biomed*, vol. 22, pp. 937-51, Nov 2009.
[177] J. M. Jin and J. Chen, "On the SAR and field inhomogeneity of birdcage coils loaded with the human head," *Magnetic Resonance in Medicine*, vol. 38, pp. 953-963, Dec 1997.
[178] K. Ugurbil, M. Garwood, J. Ellermann, K. Hendrich, R. Hinke, X. P. Hu, *et al.*, "Imaging at High Magnetic-Fields - Initial Experience at 4T," *Magnetic Resonance Quarterly*, vol. 9, pp. 259-277, Dec 1993.
[179] T. S. Ibrahim, "A numerical analysis of radio-frequency power requirements in magnetic resonance imaging experiment," *Ieee Transactions on Microwave Theory and Techniques*, vol. 52, pp. 1999-2003, Aug 2004.
[180] F. Liu and S. Crozier, "An FDTD model for calculation of gradient-induced eddy currents in MRI system," *IEEE Transactions on Applied Superconductivity*, vol. vol.14, no.3, pp. 1983-1989, // 2004.
[181] F. Liu, S. Crozier, H. Zhao, and B. Lawrence, "Finite-difference time-domain-based studies of MRI pulsed field gradient-induced eddy currents inside the human body," *Concepts in Magnetic Resonance*, vol. 15, pp. 26-36, 2002.
[182] A. Trakic, J. Jin, M. Y. Li, D. McClymont, E. Weber, F. Liu, *et al.*, "A comparative numerical study of rotating and stationary RF coils in terms of flip angle and specific absorption rate for 7 T MRI," *Journal of Magnetic Resonance*, vol. 236, pp. 70-82, Nov 2013.
[183] J. Chi, F. Liu, E. Weber, Y. Li, and C. Stuart, "GPU-accelerated FDTD modeling of radio-frequency field-tissue interactions in high-field MRI," *Biomedical Engineering, IEEE Transactions on*, vol. 58, pp. 1789-1796, 2011.
[184] W. A. Edelstein, G. H. Glover, C. J. Hardy, and R. W. Redington, "The intrinsic signal-to-noise ratio in NMR imaging," *Magn Reson Med*, vol. 3, pp. 604-18, Aug 1986.
[185] D. Liang, H. T. Hui, and T. S. Yeo, "Increasing the Signal-to-Noise Ratio by Using Vertically Stacked Phased Array Coils for Low-Field Magnetic Resonance Imaging," *Information Technology in Biomedicine, IEEE Transactions on*, vol. 16, pp. 1150-1156, 2012.
[186] M. Li, J. Jin, A. Trakic, F. Liu, E. Weber, Y. Li, *et al.*, "High Acceleration with Rotating Radiofrequency Coil Array (RRFCA) in Parallel Magnetic Resonance Imaging (MRI)," presented at the 34th Annual International Conference of the IEEE Engineering in Medicine and Biology Society (EMBC'12), San Diego, 2012.
[187] M. Li, J. Jin, F. Liu, A. Trakic, E. Weber, and S. Crozier, "Highly accelerated parallel MRI using rotating radiofrequency coil array at 7T," in *International Society for Magnetic Resonance in Medicine, 21th scientific meeting and exhibition,*, Salt Lake City, USA, 2013.

[188] M. Li, J. Jin, F. Liu, A. Trakic, E. Weber, and S. Crozier, "Efficient Hybrid Parallel Imaging Reconstruction with Rotating Radiofrequency Coil Array," in *in International Society for Magnetic Resonance in Medicine, 21th scientific meeting and exhibition*, Salt Lake City, USA, 2013.
[189] A. Haase, J. Frahm, D. Matthaei, W. Hanicke, and K. D. Merboldt, "FLASH imaging. Rapid NMR imaging using low flip-angle pulses," *Journal of Magnetic Resonance (1969)*, vol. 67, pp. 258-266, 4// 1986.
[190] M. Li, J. Jin, Z. Zuo, F. Liu, A. Trakic, E. Weber, *et al.*, "In vivo Sensitivity Estimation and Imaging Acceleration with a Rotating RF Coil Arrays at 7 Tesla," *Journal of Magnetic Resonance*.
[191] S. Winkelmann, T. Schaeffter, T. Koehler, H. Eggers, and O. Doessel, "An optimal radial profile order based on the Golden Ratio for time-resolved MRI," *IEEE Transactions on Medical Imaging*, vol. 26, pp. 68-76, Jan 2007.
[192] K. T. Block, M. Uecker, and J. Frahm, "Undersampled radial MRI with multiple coils. Iterative image reconstruction using a total variation constraint," *Magnetic Resonance in Medicine*, vol. 57, pp. 1086-1098, 2007.
[193] V. Rasche, R. W. D. Boer, D. Holz, and R. Proksa, "Continuous radial data acquisition for dynamic MRI," *Magnetic Resonance in Medicine*, vol. 34, pp. 754-761, 1995.
[194] M. A. Bernstein, K. F. King, and X. J. Zhou, in *Handbook of MRI Pulse Sequences*, M. A. B. F. K. J. Zhou, Ed., ed Burlington: Academic Press, 2004, pp. xvii-xxii.
[195] S. Zhang, K. T. Block, and J. Frahm, "Magnetic resonance imaging in real time: Advances using radial FLASH," *Journal of Magnetic Resonance Imaging*, vol. 31, pp. 101-109, 2010.
[196] J. D. O'Sullivan, "A Fast Sinc Function Gridding Algorithm for Fourier Inversion in Computer Tomography," *Medical Imaging, IEEE Transactions on*, vol. 4, pp. 200-207, 1985.
[197] J. I. Jackson, C. H. Meyer, D. G. Nishimura, and A. Macovski, "Selection of a convolution function for Fourier inversion using gridding [computerised tomography application]," *IEEE Transactions on Medical Imaging*, vol. 10, pp. 473-8, 1991.
[198] P. J. Beatty, D. G. Nishimura, and J. M. Pauly, "Rapid gridding reconstruction with a minimal oversampling ratio," *IEEE Transactions on Medical Imaging*, vol. 24, pp. 799-808, Jun 2005.
[199] M. Li, Z. Zuo, J. Jin, R. Xue, A. Trakic, E. Weber, *et al.*, "Highly accelerated acquisition and homogeneous image reconstruction with rotating RF coil array at 7T-A phantom based study," *J Magn Reson*, vol. 240, pp. 102-12, Mar 2014.
[200] M. D. Robson and G. M. Bydder, "Clinical ultrashort echo time imaging of bone and other connective tissues," *NMR in Biomedicine*, vol. 19, pp. 765-780, 2006.
[201] D. J. Tyler, M. D. Robson, R. M. Henkelman, I. R. Young, and G. M. Bydder, "Magnetic resonance imaging with ultrashort TE (UTE) PULSE sequences: Technical considerations," *Journal of Magnetic Resonance Imaging*, vol. 25, pp. 279-289, 2007.
[202] M. Benjamin and G. M. Bydder, "Magnetic resonance imaging of entheses using ultrashort TE (UTE) pulse sequences," *Journal of Magnetic Resonance Imaging*, vol. 25, pp. 381-389, 2007.
[203] W. C. Bae, J. R. Dwek, R. Znamirowski, S. M. Statum, J. C. Hermida, D. D. D'Lima, *et al.*, "Ultrashort echo time MR imaging of osteochondral junction of the knee at 3 T: identification of anatomic structures contributing to signal intensity," *Radiology*, vol. 254, pp. 837-45, Mar 2010.
[204] E. K. Brodsky, A. A. Samsonov, and W. F. Block, "Characterizing and correcting gradient errors in non-cartesian imaging: Are gradient errors linear time-invariant (LTI)?," *Magnetic Resonance in Medicine*, vol. 62, pp. 1466-1476, 2009.
[205] J. H. Duyn, Y. Yang, J. A. Frank, and J. W. van der Veen, "Simple Correction Method fork-Space Trajectory Deviations in MRI," *Journal of Magnetic Resonance*, vol. 132, pp. 150-153, 1998.

[206] M. Takizawa, H. Hanada, K. Oka, T. Takahashi, E. Yamamoto, and M. Fujii, "A robust ultrashort TE (UTE) imaging method with corrected k-space trajectory by using parametric multiple function model of gradient waveform," *IEEE Transactions on Medical Imaging,* vol. 32, pp. 306-16, Feb 2013.

[207] M. Li, J. Jin, F. Liu, A. Trakic, and S. Crozier, "Efficient hybrid imaging reconstruction of sensitivity encoding parallel imaging performed on rotating radiofrequency coil array," in *International Society for Magnetic Resonance in Medicine, 21st Annual Meeting and Exhibition*, 2013.

[208] A. Averbuch, R. R. Coifman, D. L. Donoho, M. Elad, and M. Israeli, "Fast and accurate polar Fourier transform," *Applied and Computational Harmonic Analysis,* vol. 21, pp. 145-167, 2006.